Title	Microstructure Control and Characterization of Porous Ceramic Materials Prepared by Powder Processing Methods
Author(s)	Xi, Xiuan
Citation	大阪大学, 2015, 博士論文
Version Type	VoR
URL	https://doi.org/10.18910/52120
rights	
Note	

Doctoral Dissertation

Microstructure Control and Characterization of Porous Ceramic Materials Prepared by Powder Processing Methods

Xiuan Xi

January, 2015

Division of Materials and Manufacturing Science,

Graduate School of Engineering,

Osaka University

Contents

Chapter 1

General Introduction

1.1 Introduction

Energy security, economic growth and environment protection are the national energy policy drivers of any country of the world. As world populations grow, global demand for energy services is expected to increase by as much as an order of magnitude by 2050 [1]. To meet this energy demand, billions metric tons carbon equivalent of greenhouse gas (GHG) emission will be released in the atmosphere. Approximately, 80% is due to carbon emissions from the combustion of energy fuels. It is also now well established that global warming is taking place due to effluent gas emission, mainly CO_2 [2]. During the past century, global surface temperatures have increased at a rate near 0.6 °C/century. This trend has dramatically increased during the past 25 years [3]. Moreover, problems with energy supply and use are related not only to global warming but also to such environmental concerns as air pollution, acid precipitation, ozone depletion, forest destruction, and emission of radioactive substances [4-7].

Therefore, energy and the environment pose major scientific and technological challenges for the 21st century. New technologies for increasing the efficiency of harvesting and utilizing energy resources will become increasingly important. In response to these critical need, some potential solutions have evolved, including energy conservation through improved energy efficiency, reduction in the consumption of fossil fuels, and an increase in the supply of environmental-friendly energy [8-10]. In this regards, porous ceramics play an important part in addressing the needs for technology development in aforementioned field, e.g., thermal insulation materials [11-16] and solid oxide fuel cells [17-21]. In particular, there are needs for economic and environmentally benign methods which can produce these materials efficiently.

1.2 Features of porous ceramic materials

Materials containing tailored porosity exhibit special properties and features that usually cannot be achieved by their conventional dense counterparts. For this reason, porous materials find nowadays many applications as end products and in several technological processes. Especially, among these various applications, an increasing number of applications that require porous ceramic materials have appeared in the last decades, since they can operate over a wide range of conditions, whereas polymers and metallic materials are often unsuitable.

The advantages of using porous ceramics include usually the high melting point, tailored electronic properties, high corrosion, and wear resistance in combination with the features gained by the replacement of solid material by voids in the component. Such features include low thermal mass, low thermal conductivity, controlled permeability, high surface area, low density, high specific strength, and low dielectric constant [22]. These features will lead to developing various kinds of advanced materials such as filters, catalyst carriers, membranes, thermal insulation materials and solid oxide fuel cells. Actually, each specific application can be tailored by controlling the composition and microstructure of the porous ceramics. Changes in open and closed porosity, pore morphology and pore size distribution can have a major effect on the material’s properties. All of these microstructural features are in turn highly influenced by the processing method used for the production of the porous ceramics.

In this paper, the thermal insulation materials and solid oxide fuel cells were selected, and their corresponding production methods were also developed.

1.3 Porous ceramics for thermal insulation materials

The rapidly growing world energy use has already raised concerns over supply difficulties, exhaustion of energy resources and heavy environmental impacts. The International Energy Agency has gathered frightening data on energy consumption trends. During the time of 1984-2004, primary energy has grown by 49% and CO_2 emissions by 43%, with an average annual increase of 2% and 1.8% respectively. Current predictions show that this growing trend will continue [23]. As a less cost energy strategy, conservation through improved energy efficiency is necessary in the energy future. Especially, thermal insulation is important part, and thermal insulation materials are just key ones for achieving better thermal management. In this section, its energy conservation at “buildings” as an example is explained.

1.3.1 Thermal insulation for buildings

As well known, the building sector plays an important role as it accounts for significant percentages of national energy consumption: 23% for Spain [23], 25% for Japan [24], 28% for China [25], 37% for EU [23], 39% for the UK [23], 42% for Brazil [26], over 47% for Botswana [27], 47% for Switzerland [28], etc. Among the various parts of energy consumption in the buildings, space air-conditioning can have a big share of energy used to operate buildings. Generally, space heating and cooling account for 50–70% of its energy use [29]. This percentage could be higher in other parts of the world with more harsh climatic conditions and less energy efficient buildings. Both governments and scientific communities across the world have identified the potential and need for energy efficiency in the buildings, and initiated significant efforts in this direction.

Building energy efficiency can be improved by implementing either active or passive energy efficient strategies. Improvements to heating, ventilation and air conditioning (HVAC) systems, etc. can be categorized as active strategies, whereas, improvements to building envelope elements can be classified under passive strategies. Recent years, a renewed interest has raised in environmental-friendly passive building energy efficiency strategies. They are being envisioned as a viable solution to the problems of energy crisis and environmental pollution [30].

A building envelope is what separates the indoor and outdoor environments of a building. It is the key factor that determines the quality and controls the indoor conditions irrespective of transient outdoor conditions. Various components such as walls, fenestration, roof, foundation, external shading devices etc. make up this important part of any building. Walls are a predominant fraction of a building envelope and are expected to provide thermal and acoustic comfort within a building, without compromising the aesthetics of the building. The thermal resistance (R-value) of the wall is crucial as it influences the building energy consumption heavily, especially, in high rise buildings where the ratio of wall to total envelope area is high. The placement of insulation material within the building component is a major contributor and obvious practical and logical first step towards achieving energy efficiency in the envelope-load dominated buildings [31-36].

1.3.2 Thermal insulation process

Thermal insulation is a material or combination of materials, that, when properly applied, retard the rate of heat flow by conduction, convection, and radiation. It retards heat flow into or out of a building due to its high thermal resistance [37]. Fig.1.1shows the conduction heat transfer process from hot (T_1) to cold (T_2) surfaces. The heat flux across the insulation material layer “Q” (W/m^{-2}) is related to the temperature difference between two sides of the layer “$T_2 – T_1$” (K), the thickness of the layer “L” (m) and the thermal conductivity of the material layer “k” (W/(m•K)). This relationship is expressed by [38]:

$$Q = \frac{-k(T_2 - T_1)}{L} \tag{1}$$

The thermal conductivity “k” is a parameter to estimate the heat transfer capability of a material, which is strongly dependent of the material density (or fraction of pores). The theoretical model proposed by Aivazov and Domashnev [39], well correlates the thermal conductivity of porous materials with the porosity according to Equation 2:

$$k = k_0 \cdot \frac{1-P}{1+nP^2} \tag{2}$$

where k_0 is the thermal conductivity of dense materials whose porosity is zero; P is the volume fraction of pores, and n is a constant. According to the formula, the thermal conductivity decreases with the increase of the porosity. It is the air entrapped within the insulation, which provides the thermal resistance. Creating small cells (closed cell structure) within thermal insulation across which the temperature difference is not large also reduces radiation effects. It causes radiation ‘paths’ to be broken into small distances where the long-wave infrared radiation is absorbed and/or scattered by the insulation material.

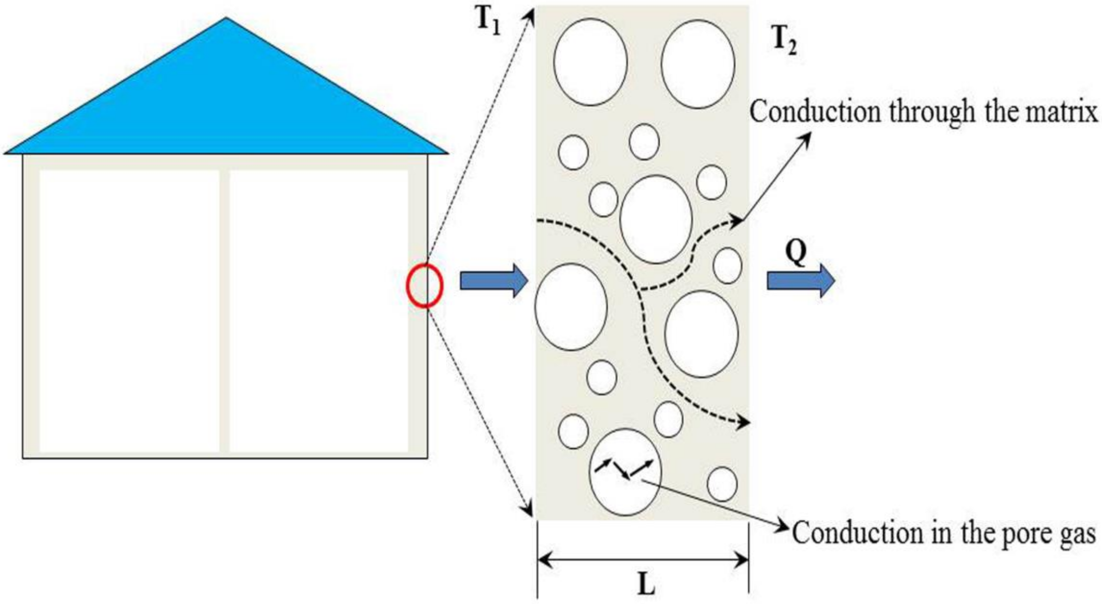

Fig. 1.1 Conduction heat transfer process from hot (T_1) to cold (T_2) surfaces.

1.3.3 Selection of the thermal insulation materials

The thermal conductivity and thermal inertia are practically the most important factors that affect the selection. On the other hand, flammability, cost, environmental and health impacts are also important factors in selecting an appropriate insulation [40, 41]. Among the various thermal insulation materials [42, 43], porous ceramic materials represent a highly valuable solution for thermal insulation, since they generally possess a higher mechanical, chemical, and thermal stability. For instance, in a fire case, the polymeric foams may result in a rather serious calamity with toxic gas generation, but the ceramic material is fire-resistant without any toxic gas generation. In addition, the benefits of porous ceramics used for thermal insulation also include their long life and ceramic fibre free et al [44, 45].

1.3.4 Economic and environmentally benign method of porous ceramics for insulation

As buildings carry a high consumption of materials and energy, the costs associated with porous ceramics for building insulation have still presented a major impediment to their large-scale adoption by the building industry, which are not only affected by the starting materials but also by the foaming agents [46, 47]. Therefore, it is necessary to identify and select a method that is much simpler and economically cheaper and that can be easily scaled-up for production of porous ceramics efficiently.

There are many production methods of porous building materials. In these methods, a fabrication route of porous ceramics from polishing porcelain stoneware tile residues (PPR) is one approach to achieve building insulation efficiently, as this should allow for much easier fabrication by foaming or bloating during firing [48,49]. The concept of this method is explained as follows: PPR as the main raw material and feldspar, ball clay and quartz etc. as minor raw materials, they were planetary-milled with distilled water. Then the raw material powders were prepared via drying and sieving, and the porcelain green bodies were formed by dry-pressing the raw material powders. Finally, the green bodies were fired in an electric furnace in air atmosphere. The properties of the resultant porous ceramics were shown in Table 1.1. These properties confirmed the viability of this method to achieve high-quality porous ceramics suitable for building insulation [30]. However, this method is still difficult to achieve control of the microstructure and properties of the porous ceramics, because the foaming behaviors of PPR and its influential factors during firing still remain unclear.

Table 1.1 Properties of the porous ceramics prepared from PPR [50, 51].

Bulk density (g/cm^3) / Porosity (%)	Compressive strength (MPa)	Thermal conductivity (W/m· K)
0.45 / 82	3.0	0.19
0.81 / 67	14.3	0.30
1.20 / 51	55.9	0.61

1.4 Porous materials for solid oxide fuel cells

1.4.1 Introduction of solid oxide fuel cells

The exhaustion of the major fossil energy sources on earth in near future and the serious environment pollution from the fuel combustion processes are also the most important problems of modern society. The generation of energy by clean, efficient and environmental-friendly means is now one of the major challenges for engineers and scientists. Solid oxide fuel cells (SOFCs) are electrochemical devices that convert the energy of a chemical reaction directly into electrical energy. Owing to the utilization of solid electrolyte and high operation temperatures, it offers many advantages over conventional power-generating systems in terms of efficiency, reliability, modularity, fuel flexibility, and environmental friendliness [52-54]. Therefore, SOFCs are considered as one of the most promising power generation technologies in the 21st century, and a tremendous of research activities on SOFCs from both academic and industrial fields on the purpose of trying to develop them into practical devices has been envisioned.

In its simplest form, a single cell of SOFC is typically composed of a porous cermet anode and a porous oxide cathode, with a dense electrolyte sandwiching them. The operating principle of such a cell is schematically illustrated in Fig. 1.2 [55]. Mostly, electrolytes are oxygen ion (O^{2-}) conductors. The operating principle of a SOFC involves the oxidation of hydrogen (H_2) at the anode (on using H_2 as fuel), reduction of molecular oxygen (O_2) at the cathode and the diffusion of the produced O^{2-} through an electrolyte into the anode where it reacts with H_2 ions (H^+) to produce water. At the same time, electrons flow from the anode to the cathode through an external circuit to

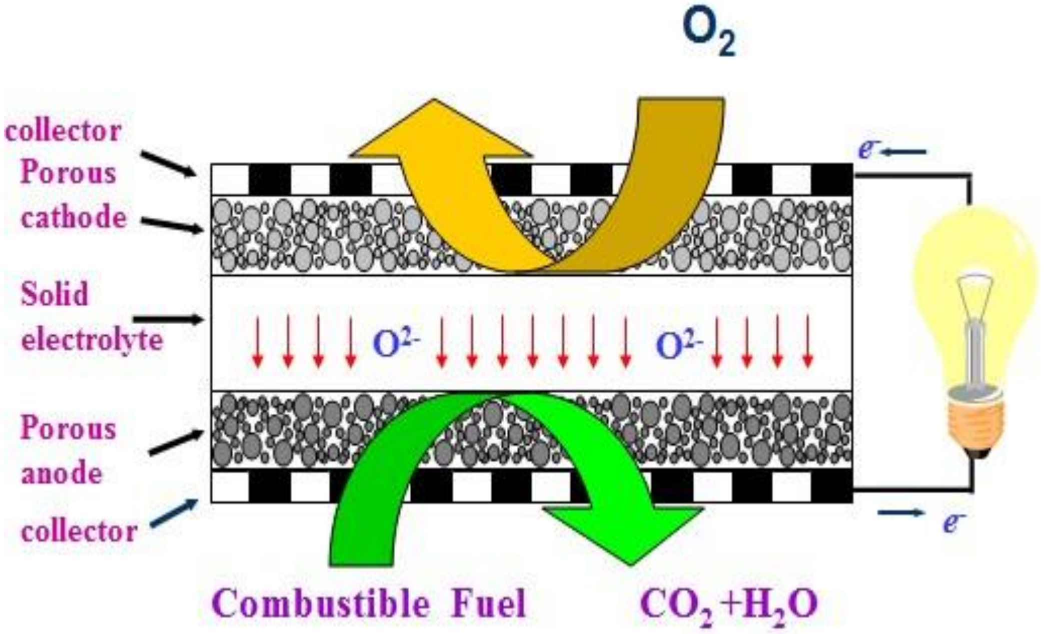

Fig. 1.2 Schematic drawing of power generation principle for SOFC.

generate power. In this way, the conversion from chemical energy into electrical energy is realized. Power generation would continue as long as fuel and oxidants are supplied. Reactions occurring at anode, cathode and overall reaction on using H_2 as fuel, are summarized in Eqs. (3) – (5).

Anode reaction: $2H_2 \rightarrow 4H^+ + 4e^-$ (3)

Cathode reaction: $O_2 + 4e^- \rightarrow 2O^{2-}$ (4)

Overall cell reaction: $2H_2 + O_2 \rightarrow 2H_2O$ (5)

When CO and hydrocarbons (such as methane) are used as fuels, following overall reactions occurs:

$CO + O^{2-} = CO_2 + 2e^-$ (6)

$CH_4 + 4O^{2-} = CO_2 + 2H_2O + 8e^-$ (7)

1.4.2 Research direction and challenge for SOFCs

State-of-the-art SOFCs are composed of YSZ electrolyte and typically operated at 1000◦C [56]. Such a high temperature is beneficial for improving the electrode reaction kinetics and reducing the electrolyte ohmic drop. Unfortunately, it also sets strict requirements on the cell materials. Both the sintering and the phase reaction between the cell components are obviously accelerated with increasing operation temperature. Operation at the intermediate range of 500-800◦C offers the choice of low cost metallic materials, such as stainless steels for SOFCs interconnection and construction materials, which would make both the stack and balance-of-plant cheaper. On the other hand, the drop in operation temperature also alleviates the solid-phase reaction between the cell components, effectively reducing the maintenance cost and prolonging the lifetime of the fuel cell system [57]. However, at the intermediate temperature range, the electrode performance of SOFCs is deteriorated with decreasing operating temperature. Therefore, fabrication of the highly active electrode is the key factors for the development of intermediate temperature solid oxide fuel cells (IT-SOFCs).

1.4.3 State –of –the–art anode materials for SOFCs: Ni/YSZ

The high catalytic activity and mechanical/chemical stability of Ni–YSZ (yttria-stabilized zirconia) cermets, as well as their compatibility with most electrolytes and interconnect materials, has made them the most extensively studied anode material in the field of SOFCs [58-62]. In such applications, the electrochemical reaction inside the anode is considered to occur around the triple-phase boundary (TPB), which is the contacting point that is formed among fuel gas, Ni and YSZ as shown in Fig. 1.3 [63]. The Ni therefore provides not only an excellent catalyst for the electrochemical oxidation of hydrogen, but also the predominant electron pathway through the anode. At the same time, the YSZ creates the necessary framework for the dispersion of Ni particles, and inhibits growth of the Ni powder during both consolidation and operation. It also offers a significant ionic contribution to the overall conductivity, thereby effectively broadening the TPBs.

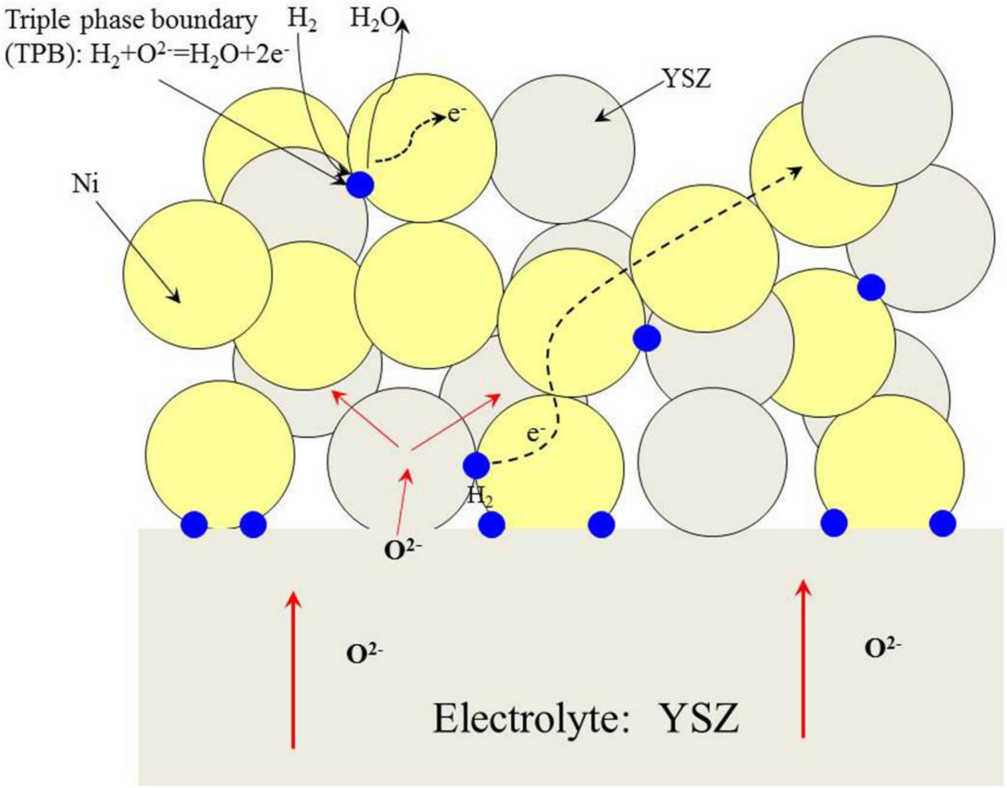

Fig. 1.3 Schematic illustrations of Ni–YSZ anode structure.

1.4.4 Development of high-performance Ni/YSZ anode for IT-SOFCs

For efficient functioning of Ni/YSZ anode, an optimum amount of porosity, its appropriate distribution and connectivity are very essential, as they facilitates easy transportation of fuel gas towards the reaction site and the reaction product diffusing out of the anode [64]. In addition to the vol% of porosity, factors such as nature of the pores (closed pores or open pores), size of the pores, pores size distribution, pore tortuosity, etc., also play a dominant role in impacting the polarization characteristics of Ni/YSZ anode. Because the electrochemical reaction occurs around the triple-phase boundary (TPB), which is the contacting point that is formed among fuel gas, Ni and YSZ. TPBs which are not connected to gas chains through open pores are electrochemically inactive. In addition, when reduced vol% of pores is present or size of the existing pores is small, diffusion becomes increasingly difficult, especially with increase in the operating current density. It results in a concentration polarization and reduced efficiency. Closed pores are not only ineffective in supplying the gas, but also detrimental, as they might occupy the regions which otherwise would have been occupied by electrochemically active TPBs (EATPBs).

To develop the highly active Ni/YSZ anode for IT-SOFC, it is required to contain as much EATPBs as possible to provide abundant electrochemical reaction site. Various electrode models have revealed that the EATPBs density is predominantly determined by microstructural characteristics such as the particle size, and the relative distribution of its individual components. A finer microstructure with uniformly distributed Ni, YSZ phases and pores in the anode will be beneficial to maximizing the EATPBs density [65, 66]. In this regards, NiO/YSZ composite particles are better tools for making good pore structure which makes larger TPBs. Especially, the preparation method adopted for this composite particles should yield a homogeneous mixture of NiO and YSZ with appropriate composition, as the pores of the resultant Ni–YSZ anode are predominantly formed by the reduction of NiO.

1.5 Objective of this study

1.5.1 Objective

As mentioned in the preceding section, the fabrication of porous ceramics from PPR is one of the promising methods for thermal insulation materials to be used for buildings. However, this method is still difficult to achieve control of the microstructure and properties of the porous ceramics, because the foaming mechanism of PPR and its influential factors during firing still remain unclear. With this in mind, a fundamental research on the foaming mechanism of the PPR and its influential factors during firing should be carried out. In this way, it is hoped to clarify the dominant factors linking the foaming behavior of PPR, with a view to the development of control technologies for high thermal insulation performance building ceramics.

On the other hand, the porous structure also plays an important part in the electrochemical reaction of electrode for SOFCs. To develop a highly active Ni/YSZ anode for IT-SOFCs, a finer microstructure with uniformly distributed Ni, YSZ phases and pores is essential to provide abundant triple-phase boundaries (TPBs) for electrochemical reaction. In this regards, homogeneous NiO/YSZ nanocomposite particles are better tools for making good pore structure which makes larger TPBs, because the pore structure of the resultant Ni–YSZ anode are predominantly formed by the reduction of NiO. Therefore, another aim of this work is to synthesize homogeneous NiO-YSZ nanocomposite particles for high-performance IT-SOFCs.

1.5.2 Scope of thesis

This thesis comprises 6 chapters. In chapter 1, the background of this study and its objectives were clarified.

In chapter 2, porcelain green bodies were prepared using porcelain stoneware tile powder as the major raw material, with magnesium oxychloride cement (MOC) and silicon carbide (SiC) as additives. These were fired at 1000~1200℃. Effect of the MOC and its mixture with SiC on the microstructure and properties of porcelain ceramics was quantitatively investigated. It was discussed the foaming origin of the PPR and the dominant factors linking its foaming behavior.

In chapter 3, porcelain green bodies were prepared using porcelain stoneware tile powder as the major raw material, and silicon carbide (SiC) and CaO as additives. These were fired at 1000–1200 °C. The effects of SiC particle size and CaO content on the microstructure and foaming properties of porcelain ceramics were investigated in detail. It was discussed the relationship among foaming behavior, phase composition and SiC particle size during firing of a porcelain tile matrix, with a view to further clarifying the dominant factors linking foaming behavior of the PPR and the development of improved processing method.

In chapter 4, a novel synthetic method to NiO-YSZ nanocomposite particles for

SOFC anode was proposed. The properties of the as-synthesized composite particles were evaluated, and their formation mechanism was also discussed. Then, the Ni/YSZ anode was fabricated by screen-printing the paste made by the NiO-YSZ nanocomposite particles, sintering at 1350℃and subsequent reduction. Finally, the microstructure and electrochemical performance of the resultant anode were evaluated

In chapter 5, Ni content of NiO–YSZ nanocomposite particles was changed by the novel co-precipitation method. Ni-YSZ anodes were fabricated by sintering screen-printed nanocomposites at 1350 ℃ for 2 h and then selectively reducing them. The effects of NiO-YSZ nanocomposite particles composition on the microstructures and electrochemical performance of the resultant Ni-YSZ anodes were discussed in detail.

In chapter 6, the results obtained throughout this study were summarized.

References

[1] N. S. Lewis, D. G. Nocera, Proceedings of the National Academy of Sciences of the United States of America 103 (2006) 15729–1573.

[2] P. M. Cox, R. A. Betts, C. D. Jones, S. A. Spall, I. J. Totterdell, Nature 408 (2000) 184–187.

[3] A. B. Stambouli, E. Traversa, Renewable and Sustainable Energy Reviews 6 (2002) 433–455.

[4] A. M. Omer, Renewable & Sustainable Energy Reviews 12 (2008) 2265–2300.

[5] I. Dincer, M. A. Rosen, International Journal of Energy Research 22 (1998) 1305–1321.

[6] L. Lombard, J. Ortiz, J, C. Pout, Energy and Buildings 40 (2008) 394–398.

[7] C. Y. Keong, Energy Policy 33 (2005) 679–689.

[8] K. M. Zhang, Z. G. Wen, Journal of Environmental Management 88 (2008) 1249–1261.

[9] A. M. Omer, Renewable & Sustainable Energy Reviews 12 (2008) 1562–1587.

[10] A. B. Stambouli, E. Traversa, Renewable & Sustainable Energy Reviews 6 (2002) 295–304.

[11] A. M. Papadopoulos, Energy and Buildings 37 (2005) 77–86.

[12] M. Reim, W. Korner, J. Manara, S. Korder, M. Arduini-Schuster, H. P. Ebert, J. Fricke, Solar Energy 79 (2005) 131–139.

[13] E. Kossecka, J. Kosny, Energy and Buildings 34 (2002) 321–331.

[14] G. S. Wei, Y. S. Liu, X. X. Zhang, F. Yu, X. Z. Du, International Journal of Heat and Mass Transfer 54 (2011) 2355–2366.

[15] G. M. Pajonk, Colloid and Polymer Science 281 (2003) 637–651.

[16] T. W. Clyne, I. O. Golosnoy, J. C. Tan, A. E. Markaki, Philosophical Transactions of the Royal Society A: Mathematical, Physical and Engineering Sciences 364 (2006) 125–146.

[17] A. J. Jacobson, Chemistry of Materials 22 (2010) 660–674.

[18] T. Suzuki, Z. Hasan, Y. Funahashi, T. Yamaguchi, Y. Fujishiro, M. Awano, Science 325 (2009) 852–855.

[19] S. T. Aruna, M. Muthuraman, K. C. Patil, Solid State Ionics 111 (1998) 45–51.

[20] P. J. Panteix, I. Julien, P. Abelard, D. Bernache-Assollant, Ceramics International 34 (2008) 1579–1586.

[21] S. Jou, T. H. Wu, Journal of Physics and Chemistry of Solids 69 (2008) 2804–2812.

[22] A. R. Studart, U. T. Gonzenbach, E. Tervoort, L. J. Gauckler, Journal of the American Ceramic Society 89 (2006) 1771–1789.

[23] L. Perez-Lombard, J. Ortiz, C. Pout, Energy and Buildings 40 (2008) 394–398.

[24] G. Yoon, et al., The World Sustainable Building Conference in Tokyo (2005) 1–102.

[25] J. C. Lam, C. L. Tsang, L. Yang, Energy Conversion and Management 47 (2006) 1942–1953.

[26] S. Delbin, V. Gomes da Silva, The World Sustainable Building Conference in Tokyo (2005) 01–135.

[27] Central Statistics Office, Energy Statistics, Government of Botswana Publication, 2002.

[28] M. Zimmermann, H. J. Althaus, A. Haas, Energy and Buildings 37 (2005) 1147–1157.

[29] The US Department of Energy, DOE/CE-0180, USA, 2002.

[30] S. B. Sadineni, S. Madala, R. F. Boehm, Renewable and Sustainable Energy Reviews 15 (2011) 3617–3631.

[31] A. Bolatturk, Building and Environment 43 (2008) 1055–1064.

[32] J. H. Yu, C. Z. Yang, L. W. Tian, D. Liao, Applied Energy 86 (2009) 2520–2529.

[33] G. A. Florides, S. A. Tassou, S. A. Kalogirou, L. C. Wrobel, Applied Energy 73 (2002) 299–328.

[34] M. S. Mohsen, B. A. Akash, Energy Conversion and Management 42 (2001) 1307–1315.

[35] L. D. D. Harvey, Energy Efficiency 2 (2009) 139–163.

[36] S. A. Al-Sanea, M. F. Zedan, S. N. Al-Hussain, Applied Energy 89 (2012) 430–442.

[37] M. S. Al-Homoud, Building and Environment 40 (2005) 353–366.

[38] M. Moran, H. Shapiro, Fundamentals of Engineering Thermodynamics 1998.

[39] C. Efftinga, S. Güthsb, O. E. Alarcona, Materials Research 10 (2007) 301–307.

[40] N. M. P. Low, Journal of Building Physics 8 (1984) 116–26.

[41] B. K. Kandola, A. R. Horrocks, D. Price, G. V. Coleman, Journal of Macromolecular Science Part C Polymer Review 36 (1996) 721–794.

[42] A. M. Papadopoulos, Energy and Buildings 37 (2005) 77–86.

[43] D. M. S. Al-Homoud, Building and Environment 40 (2005) 353–366.

[44] E. Bernardo, R. Cedro, M. Florean, S. Hreglich, Ceramics International 33 (2007) 963–968.

[45] G. M. Mclellan, E. B. Shand, McGraw-Hill Book Co., New York, 1984.

[46] S. Hasheminia, A. Nemati, B. E. Yekta, P. Alizadeh, Ceramics International 38 (2012) 2005–2010.

[47] E. Bernardo, R. Cedro, M. Florean, S. Hreglich, Ceramics International 33 (2007) 963–968.

[48] A. M. Bernardin, M. J. DaSilva, H. G. Riella, Materials Science and Engineering: A 37 (2006) 222–225.

[49] X. J. Cai, X. A. Xi, A. Z. Shui, T. T. Wu, J. J. Chen, R. T. Jian, X. G. Wu, Bulletin of the Chinese Ceramics Society 30 (2011) 955–959.

[50] X. A. Xi, Foaming Mechanism of Polishing Tile Waste during Sintering and Its Application [D], Guangzhou, South China University of Technology, 2011.

[51] T. Lu, X. A. Xi, A. Z. Shui, X. J. Cai, H. Ma, W. Zheng, R. T. Jian, Bulletin of the Chinese Ceramics Society 30 (2011) 970–973.

[52] A. B. Stambouli, E. Traversa, Renewable & Sustainable Energy Reviews 6 (2002) 433–455.

[53] P. Zapp, Journal of Power Sources 61 (1996) 259–262.

[54] G. Y. Meng, W. Y. Liu, D. K. Peng, Ionics 4 (1998) 451–462.

[55] B. ShriPrakash, S. SenthilKumar, S. T. Aruna, Renewable and Sustainable Energy Reviews 36 (2014) 149–179.

[56] N. Q. Minh, Journal of the American Ceramic Society 76 (1993) 563–588.

[57] Z. P. Shao, W. Zhou, Z. H. Zhu, Progress in Materials Science 57 (2012) 804–874.

[58] F. Stephen, X. Qiao, Journal of the American Ceramic Society 86(2003) 401–406.

[59] M. Marinsek, K. Zupan, J. Macek, Journal of Power Sources 86 (2000) 383–389.

[60] S. D. Kim, H. Moon, S. H. Hyun, J. Moon, J. Kim, H. W. Lee, Journal of Power Sources 163 (2006) 392–397.

[61] T. Fukui, S. Ohara, M. Naito, K. Nogi, Journal of Power Sources 110 (2002) 91–95.

[62] K. R. Han, Y. Jeong, H. Lee, C. S. Kim, Materials Letters 61 (2007) 1242–1245.

[63] M. Mogensen, S. Scare, Solid State Ionics 86 (1996) 1151–I 160.

[64] M. Poon, O. Kesler, Journal of Power Sources 210 (2012) 204–217.

[65] Y. Deseure, L. Bultel, E. Siebert, Electrochimica Acta 10 (2005) 2037–2046.

[66] S.H. Chan, Z.T. Xia, Journal of the Electrochemical Society 4 (2001) 388–394.

Chapter 2

Effect of Magnesium Oxychloride Cement and Silicon Carbide Additives on Microstructure and Foaming Properties of Porcelain Ceramics

Abstract

Porcelain green bodies were prepared using porcelain stoneware tile powder as the major raw material, with magnesium oxychloride cement (MOC) and silicon carbide (SiC) as additives. These were fired at 1000~1200℃. Effect of the additives on the foaming property of porcelain ceramics and its microstructure was quantitatively investigated to clarify the foaming origin of polished porcelain waste during firing. The results showed that a small amount of the mixture of both MOC and SiC added into the porcelain green body caused the body foaming during firing more significantly, compared to the addition of either SiC or MOC. The foaming of porcelain green body with only SiC was more remarkable than that of the porcelain green body with only MOC at the same content and firing conditions. The MOC accelerated the foaming of porcelain green body with SiC during firing. In addition, the foaming mechanism was also discussed.

2.1 Introduction

Porcelain stoneware tile is a building ceramic material with the high mechanical strength, abrasion resistance, excellent chemical resistance and frost resistance. In recent years, the porcelain stoneware tile production has achieved about 4000 million square meters annually in China, and occupied more than a half of the total ceramic tile production [1-3]. In the porcelain stoneware tile production, it is necessary to polish porcelain tile surface with a polishing tool containing silicon carbide abrasive and magnesium oxychloride cement (MOC). During the polishing process, the porcelain material in a thickness range of 0.4~0.8 mm from the tile surface is commonly removed to obtain the surface gloss level of 65~70%, resulting in a large amount of polishing porcelain stoneware tile residue (PPR) [4, 5]. The residue usually contains approximately 1~3 mass% of the silicon carbide abrasive and 2~6 mass% of the MOC originated from the polishing tool. It was reported that the output of PPR has reached about 6 million tons per year in China. The large amount of PPR is generally disposed in landfill without any treatments, which causes serious environment pollution, increased mineral resource consumption and high production cost as well [6-9]. Therefore, it is important to recycle the PPR due to economic and environmental sustainabilities.

A porous ceramic tile represents a high valuable material for thermal and acoustic insulation since it possesses higher physical performance, chemical and thermal stabilities. For instance, in a fire case, the polymeric foams may result in a rather serious calamity with toxic gas generation, but the porous ceramic material is fire-resistant without toxic gas generation. Moreover, the porous ceramic material can facilitate the quick and low-cost construction because it is easy to handle, cut, drill and transport the lightweight material. Therefore, the ceramic manufacturers are seeking to produce the porous ceramic materials [10, 11].

Recent work reported that the porous ceramics could be made from the PPR with the lower production cost, because it could easily make the material foaming or bloating during firing [12-15]. However, this method is still difficult to achieve large-scale production of high quality porous ceramics from PPR, because the foaming mechanism of the PPR during firing has not been understood well. In this regards, it is very important to investigate firstly the foaming origin of the PPR during sintering for clarifying the foaming mechanism.

Approximately 1-3 mass% of the silicon carbide abrasive and 2-6 mass% of the MOC impurities derived from polishing tool exist in the PPR [5, 9, 13, 15], it seems that these impurities are the foaming origins during sintering. However, the silica protective layer generally forms on the silicon carbide particle surface due to the oxidation of silicon carbide in air atmosphere, which baffles the further oxidation. Besides, the MOC easily decomposes into MgO and HCl at 600-800℃, and the decomposition temperature is too low comparing with the general densification temperature of porcelain ceramics (about 1150-1200℃). Furthermore, since there has been little work on the investigation of effects of silicon carbide or MOC on the microstructure and properties of porcelain ceramics, the problems of PPR foaming origin during sintering are not understood yet.

The objectives of this paper are to investigate the effects of MOC, SiC and their mixture on the microstructure and properties of porcelain ceramics, and to clarify the foaming origin of polished porcelain waste during firing.

2.2 Experimental procedure

2.2.1 Sample preparation

A porcelain stoneware tile powder (Newpearl Ceramics Co. Ltd., Guangdong, China) as a main raw material was obtained by shattering and planetary-milling of porcelain tile for 45 minutes. The particle size range of the powder was from 0.1 to 45μm, and the median diameter was 6.2 μm. A PPR powder was obtained by polishing porcelain stoneware tile surface. The particle size range of the waste powder was from 0.1 to 25μm, and the median diameter was 3.6 μm. Table 1 shows their chemical compositions.

Silicon carbide powder (Haixu abrasive Co. Ltd., Zhengzhou, China) was used as an additive. The purity was more than 99.8 mass%, and the nominal particle size was 38 μm. MOC was prepared from MgO (AR, Hangzhou Wanjing New Material Co., Ltd, China), $MgCl_2 \cdot 6H_2O$ (AR, Tianjin Changlu Hangu Saltworks Co. Ltd., China) and distilled water in their molar ratio 4.6 : 1 : 17. The MOC was cured at room temperature for 1 day, and then unmoulded, cured again in air atmosphere for 14 days. MOC as an additive was obtained by shattering and planetary-milling of the MOC for 45 minutes, whose chemical composition was composed of a majority of $5Mg(OH)_2 \cdot MgCl_2 \cdot 8H_2O$ (referred to as 5-phase) and a few of the $3Mg(OH)_2 \cdot MgCl_2 \cdot 8H_2O$ (referred to as 3-phase). The particle size range of the MOC was from 0.1 to 36μm, and the median diameter was 4.3μm. The SiC powder was a typical abrasive used in porcelain tile polishing process, and the MOC also was a typical binder used in the polishing process. The slurries of the porcelain tile powder and MOC, SiC, MOC+SiC were prepared with distilled water and 0.5 mass% of polyethylene glycol (PEG-400 binder, Guangzhou

Taiqi Chemical Technology Co., Ltd, China) in the water : mixture mass ratio of 0.8 : 1, respectively. The slurries were prepared by a planetary mill for 30 minutes. The raw material powders were prepared via drying, granulating and sieving (in a sieve with 30 mesh, i.e., 550μm). The porcelain green bodies with 35mm in diameter and 5mm in thickness were formed by dry-pressing the raw powder materials at 15MPa. Then the green bodies were fired in an electric furnace in air atmosphere at 1000~1200℃ for 20 minutes at a heating rate of 5℃/min.

2.2.2 Sample characterizations

The bulk density and apparent porosity of the fired samples were measured according to the ASTM C373-88. The total porosity of the sample, ε_T (%) was determined by the following equation:

$$\varepsilon_T = (1 - \frac{d_b}{d_r}) \times 100 \tag{2.1}$$

where d_b and d_r are the bulk and true densities of the fired sample, respectively. In which d_r was previously measured according to ASTM C329-88.

The samples were characterized by scanning electron microscope (SEM, Philips L30FEG, The Netherlands), laser particle size analyzer (BT-9300S, Dandong Bettersize Instruments Ltd., China), and TG-DSC (STA 449, NETZSCH, Germany), respectively. The image analysis software (Image-Pro Plus6.0, Media Cybernetics, USA) was used to determine the pore size of the fired body.

Table 2.1 Chemical compositions of the porcelain stoneware tile powder and the PPR powder (mass%).

	IL[a]	SiO_2	Al_2O_3	Fe_2O_3	TiO_2	CaO	MgO	K_2O	Na_2O
Porcelain tile powder	0.6	69.01	22.29	0.44	0.17	0.54	0.48	1.35	4.93
Polishing porcelain tile residue (PPR)	3.14	67.27	19.21	0.37	0.15	0.62	2.94	1.19	5.17

[a] IL = ignition loss

2.3 Results and discussion

2.3.1 Foaming property of polishing porcelain tile residue during firing

Fig. 2.1 shows the effect of firing temperature on the bulk densities of the samples prepared with PPR powder and porcelain tile powder in 1000~1200℃. Clearly, the bulk density for the PPR initially increased and reached the maximum value at 1060℃, and then abruptly decreased with increasing the firing temperature. The bulk density was almost constant with an average value of 0.4g/cm^3 (total porosity about 84%) in 1120~1200℃. Also, the bulk density for the porcelain tile powder increased with elevating the firing temperature, and the bulk density obtained was 2.4g/cm^3 at 1200℃, which was the general density of densified porcelain tile. Compared to the general density (2.4g/cm^3), the bulk density of the sample prepared with the PPR powder at 1200℃ was decreased down to 17%.

Fig. 2.2 shows the SEM micrographs of the samples prepared with the PPR powder at firing temperature of 1060℃(a), 1080℃(b), 1120℃(c) and 1160℃(d), respectively. Some pore structures were formed in the sample fired at 1080℃. The higher the firing temperature, the larger the closed pores could be. The average pore size increased from 15μm in the sample fired at 1080℃ to about 1000 μm in the sample fired at 1160℃. These results were consistent with the change of bulk density with the firing temperature as shown in Fig. 2.1.

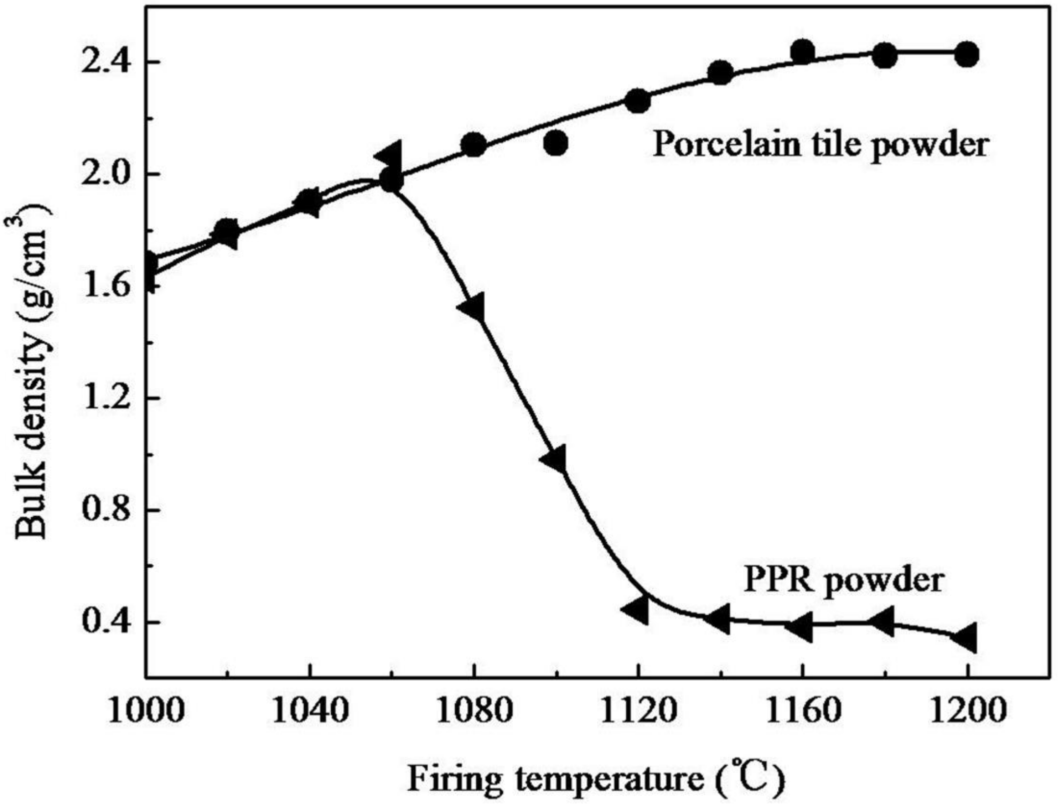

Fig. 2.1 Effect of firing temperature on the bulk densities of the samples prepared with PPR powder and porcelain tile powder, respectively.

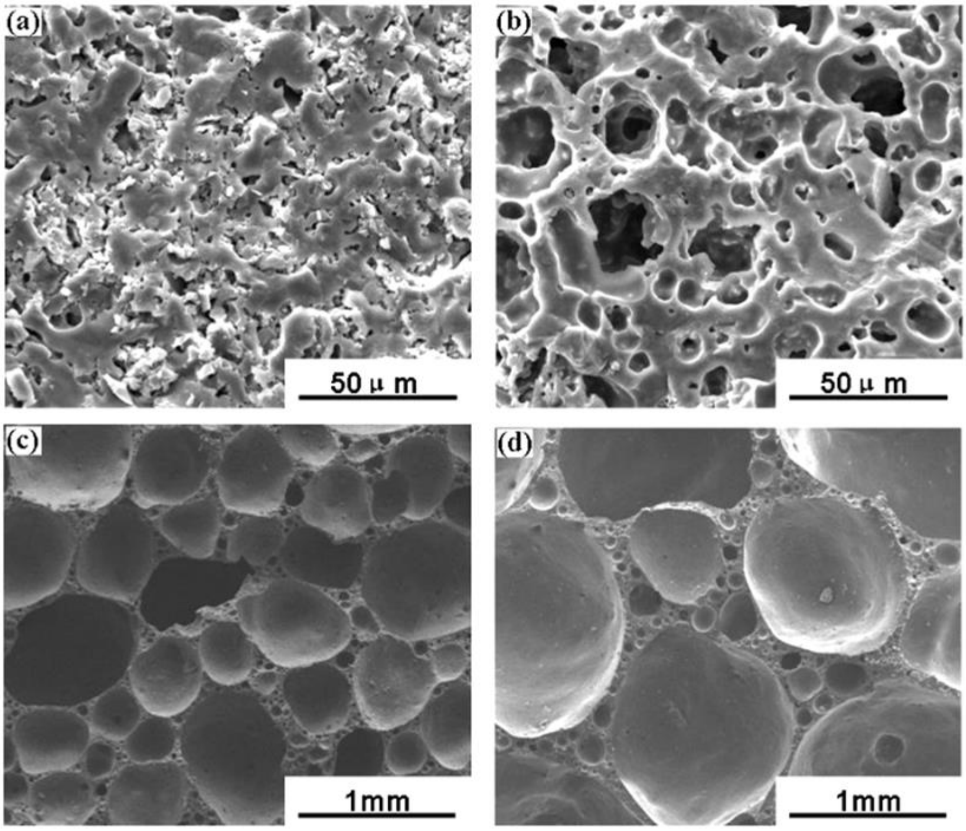

Fig. 2.2 SEM micrographs of the samples prepared with the PPR powder at firing temperature: (a)1060℃ , (b)1080℃ , (c)1120℃ and (d) 1160℃.

2.3.2 Effect of SiC on foaming property of porcelain ceramics during firing

Fig. 2.3 shows the effect of firing temperature on the bulk density of fired porcelain bodies with various SiC contents. The bulk density of the fired porcelain body without SiC gradually increased with elevating the firing temperature. However, the bulk densities of the fired porcelain bodies with 1 mass% and 2 mass% SiC initially increased and reached the maximum value at about 1120℃, and then abruptly decreased with elevating the firing temperature. Their variation was similar to that of the sample prepared with the PPR powder, as shown in Fig. 2.1. At 1200℃, the bulk density reached 1.4g/cm^3 for the sample with 1 mass% SiC and about 1.1g/cm^3 for the sample with 2 mass% SiC. Compared to the general density of densified porcelain tile (2.4g/cm^3), the decreasing rate of the bulk density was 42% for the sample with 1mass% SiC and 54% for the sample with 2 mass% SiC, respectively.

Fig. 2.4 shows the SEM micrographs of the fired porcelain bodies with 2 mass% SiC at the firing temperature of 1050℃(a), 1100℃(b), 1150℃(c) and 1200℃(d), respectively. Clearly, the higher the firing temperature, the greater the densification, the closed pores can be more and larger. When the samples fired at 1050℃ and 1100℃ were in a loose state, there were not the closed pores in these samples. However, when the samples fired at 1150℃ and 1200℃, they became a dense state, and large closed pores were observed in these samples.

Clearly, the foaming property of fired porcelain body was significantly affected by SiC additive. However, the transition temperature of bulk density for the fired porcelain body with only SiC additive was higher than that of the sample prepared with the PPR powder. Besides, the bulk density of the fired porcelain body with SiC additive was much higher than that of the sample prepared with the PPR powder at the same firing temperature. These results indicate that SiC addition has an effect on the foaming during firing, and another impurity (i.e., MOC in the PPR) should also affect the foaming during firing.

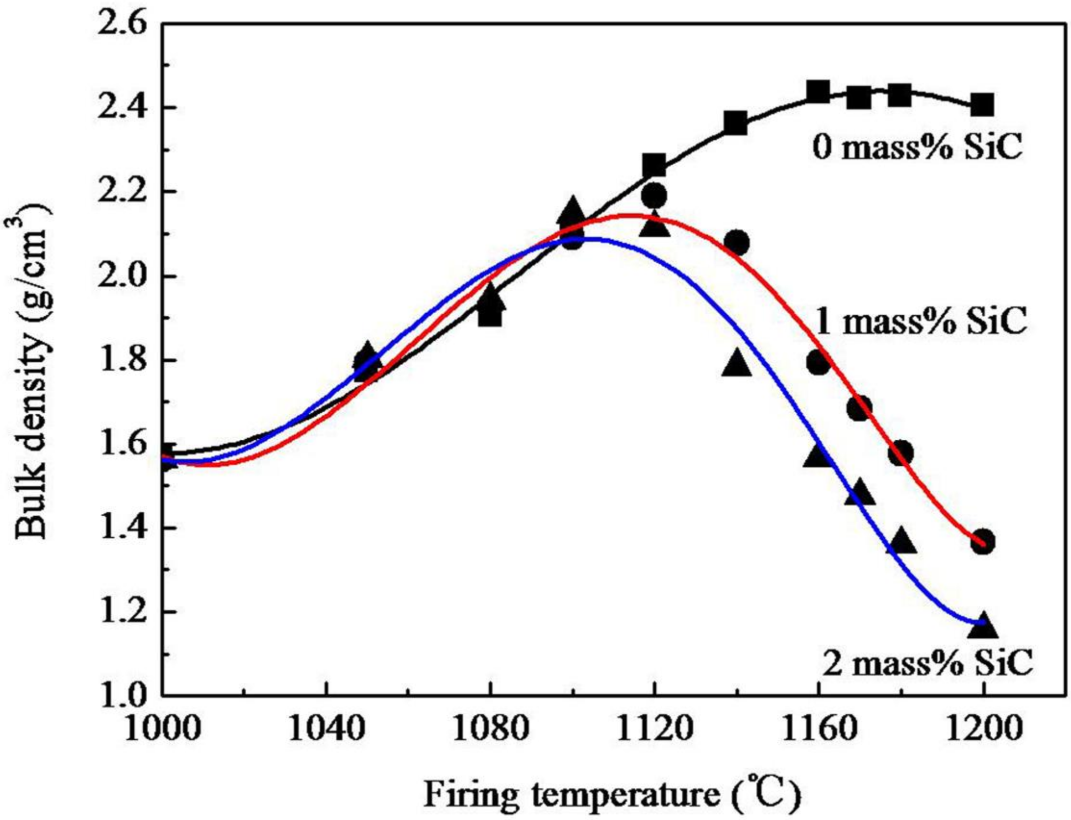

Fig. 2.3 Effect of firing temperature on the bulk density of fired porcelain bodies with various SiC contents.

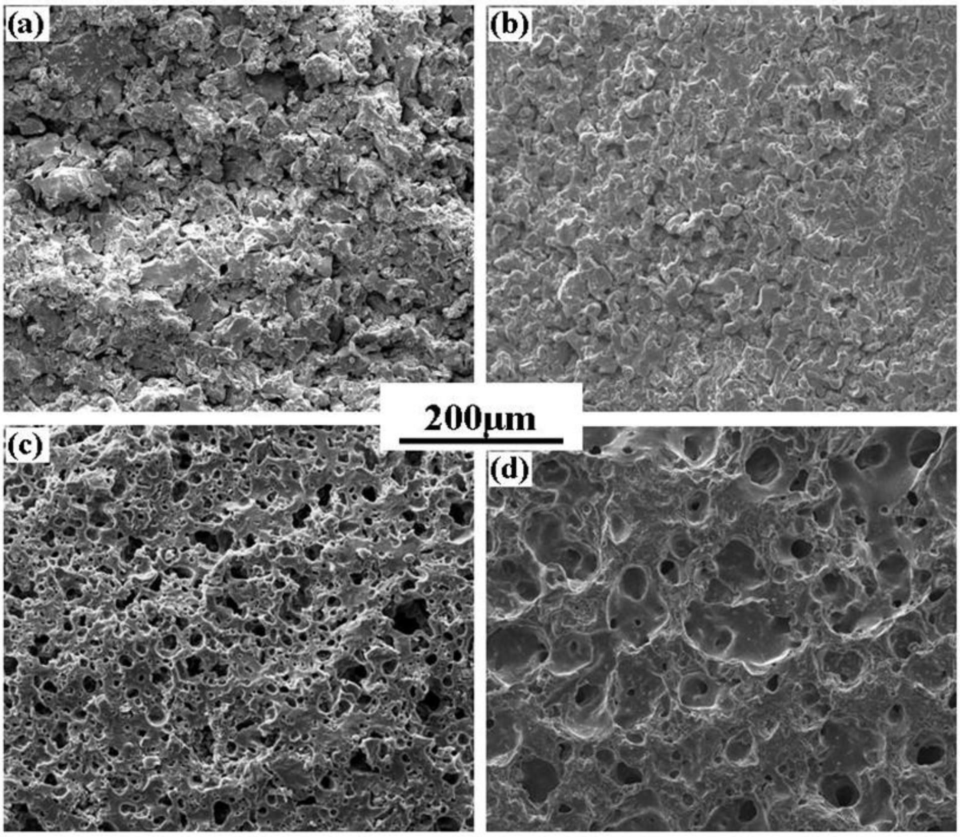

Fig. 2.4 SEM micrographs of the fired porcelain bodies with 2 mass% SiC: (a) 1050℃, (b) 1100℃, (c) 1150℃ and (d) 1200℃.

2.3.3 Effect of magnesium oxychloride cement (MOC) and its mixtures with SiC on foaming property of porcelain ceramics

Fig. 2.5 shows the effect of MOC content on the bulk densities of fired porcelain bodies without and with 1 mass% SiC at 1200℃. In the absence of SiC, the bulk density of the fired porcelain body slightly decreased with increasing the MOC content and kept a constant value of 2.0 g/cm^3 in the MOC range of 4~8 mass%. The decreasing rate of the bulk density was only 17%. The bulk density of the fired porcelain body with 1 mass% SiC sharply decreased with increasing the MOC content and kept a constant value of 0.6 g/cm^3 in the MOC range of 6~8 mass%, and the decreasing rate reached 75%, which was close to the decreasing rate of the sample prepared with the polished porcelain waste powder (83%). It is indicated that the mixture of SiC and MOC causes more significant foaming in the porcelain green body during firing rather than the case of only SiC or MOC. The foaming of fired porcelain body with only SiC during firing (Fig.2.3) is more remarkable than that of fired porcelain body with only MOC in the same additive content and firing conditions (Fig.2.5).

Fig. 2.6 shows the TG-DSC curve of the MOC powder. The mass loss of the MOC powder was approximately 40 mass% at > 500℃ due to the MOC decomposition to H_2O, HCl and MgO at 150~600℃ [16-19].

Since the decomposition temperature of MOC is much lower than the densification starting temperature of porcelain green body (about 1050℃) [26, 27], the gas generated by the thermal decomposition at the decomposition temperature (150~600℃) in the fired body has been almost discharged before the densification of the body, and the MOC has a slight effect on the foaming during firing (>1050℃). However, MgO is the residual product by the decomposition of MOC, and it should accelerate the foaming by the SiC oxidation corrosion during firing.

Fig. 2.7 shows the effect of firing temperature on the bulk densities of porcelain green bodies with 1 mass% SiC and various MgO contents in 1000~1200℃. Clearly, the transition temperature of the bulk density for the fired porcelain body without MgO (with only 1 mass% SiC) was 1120℃, but it reduced to 1080℃ for the fired porcelain body with 1 mass% SiC and 4 mass% MgO, and in this condition, the decreasing rate of the bulk density also reached 79% at 1200℃. These are close to the results of the sample prepared with the PPR powder as shown in Fig. 2.1.

Fig. 2.8 shows the bulk density of fired porcelain body with different SiC content as a function of the concentration of MgO at 1200℃. Obviously, bulk density of the samples with 1 mass% and 3 mass% SiC decreased significantly with increasing the concentration of MgO in the 0~5 mass% interval. However, this decrease in the bulk density becomes insignificant once the amount of MgO addition reaches a range of 5–8 mass%, and their bulk density were constant with an average value of 0.5 and 0.3 g/cm^3, respectively. Compared to the general density of densified porcelain tile (2.4g/cm^3), the decreasing rate of the bulk density was 79% for the sample with 1 mass% SiC and 87.5% for the sample with 3 mass% SiC, respectively, which is very closed to that of PPR powder.

Fig. 2.9 shows the SEM micrographs of the fired porcelain bodies with 1 mass% SiC and 0 mass.% (a), 2 mass% (b), 4 mass% (c) and 6 mass% (d) of MgO at 1200℃. With increasing the MgO content, the pore size increased, the pore number density increased and the pore shape appeared spherical. The average pore size was 69μm, 253μm, 673μm and 710μm in (a) ~ (d) of Fig. 2.9, respectively.

2.3.4 Foaming mechanism of the polishing porcelain tile residue during firing

The foaming behavior is likely related to the oxidation and corrosion reaction of SiC in a porcelain tile matrix. Generally, the silica protective layer forms on the SiC particle surface due to the oxidation in air atmosphere, which are responsible for the oxidation resistance of SiC, because the oxygen diffusion rate through the silica protective layer is rather slow (10^{-14}~10^{-15} cm^2/s in vitreous silica) [20-22]. However, in porcelain stoneware tile, a minor crystalline phase formed by mullite and quartz crystals becomes immersed in a vitreous phase that is formed by a siliceous glass containing alkaline and earth alkaline oxides, mainly K_2O, Na_2O, and MgO [1, 8]. These oxides have a significant corrosive effect on the SiO_2 protective layer normally formed on the surface of SiC particles, causing the broken of the protective layer and the rapidly oxygen diffusion through the protective layer. This leads to a substantial increase in the chemical reaction of SiC with oxygen to generate a large amount of CO_2 and CO gas. Given that a large amount of liquid phase is generated in a fired porcelain body above 1100 °C, it becomes increasingly difficult for this gas to discharge outward [23]. With more gas remaining in the liquid, closed pores are generated, which explains the observed reduction in bulk density.

Any subsequent increase in temperature reduces the effective viscosity, which can deform the porcelain body and thereby increase the occluded pore gas pressure (P_g) above the capillary pressure (P_c). If this occurs, then the porcelain body expands, thus explaining the observed significant reduction in bulk density with increasing firing temperature. The firing process for this type of material is expressed by [24, 25]:

$$-\frac{d\varepsilon}{\varepsilon dt} = \frac{3}{4\eta_s}(P_c - P_g) \tag{2.2}$$

where ε is porosity, t is temperature, η_s is viscosity, P_g is occluded pore gas pressure and P_c is capillary pressure, which is given by $P_c = -2\gamma/r$, where γ is surface tension and r is pore radius. Therefore, as the bulk density decreases, the pore size increases with increasing the firing temperature, as shown in Fig. 2.3 and Fig. 2.4.

On the other hand, the foaming properties of porcelain ceramics are also affected by the presence of MOC during firing, due to its decomposition into MgO at high temperature. MgO behaves as a network modifier in silicate network, which can disrupt the continuity of the silicate structure due to the breakage of Si-O bonds with the formation of non-bridging oxygen and decrease the degree of polymerization (DOP) of the silicates, resulting in the formation of the silicate liquid at a lower temperature [26] and the SiC oxidation corrosion at a lower temperature to generate a large amount of CO_2 and CO gas. As a result, it is supposed that the foaming of the porcelain green body occurred at lower temperature during firing. Also, the decrease in degree of polymerization (DOP) of the silicates is associated with its physical and chemical changes such as the decreased viscosity. Because the activation energy for the viscous flow of the silicate melts is strongly dependent on the DOP [27-29]. Thus, it is considered that the expansion resistance of the stoma formed in the silicate liquid becomes smaller, resulting in the significant increase of the pore size with increasing the MgO content (see Fig. 2.9). Furthermore, since silicate liquid also dissolves appreciable quantities of molecular oxygen, oxygen can thus migrate through the liquid silicate. The decrease of liquid viscosity may accelerate the oxygen migration in the liquid silicate [30], which can facilitate the SiC oxidation corrosion to generate more gas.

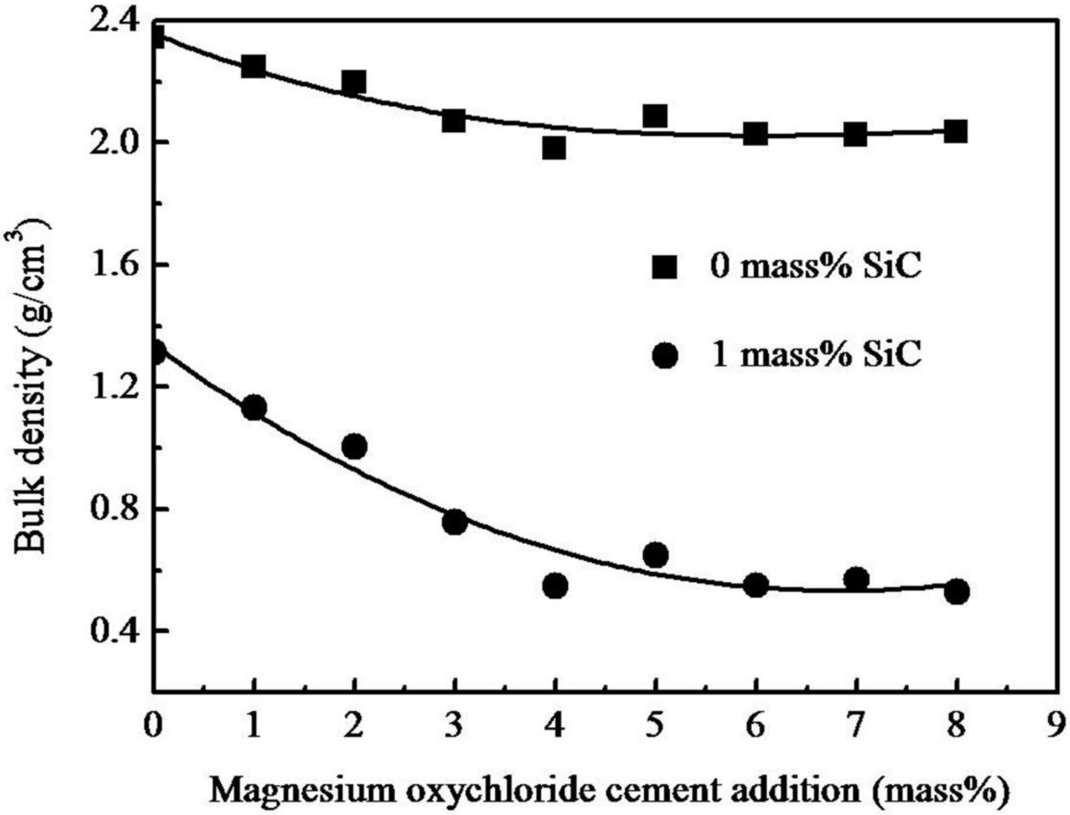

Fig. 2.5 Effect of MOC content on the bulk density of fired porcelain bodies without and with 1 mass % SiC at 1200℃.

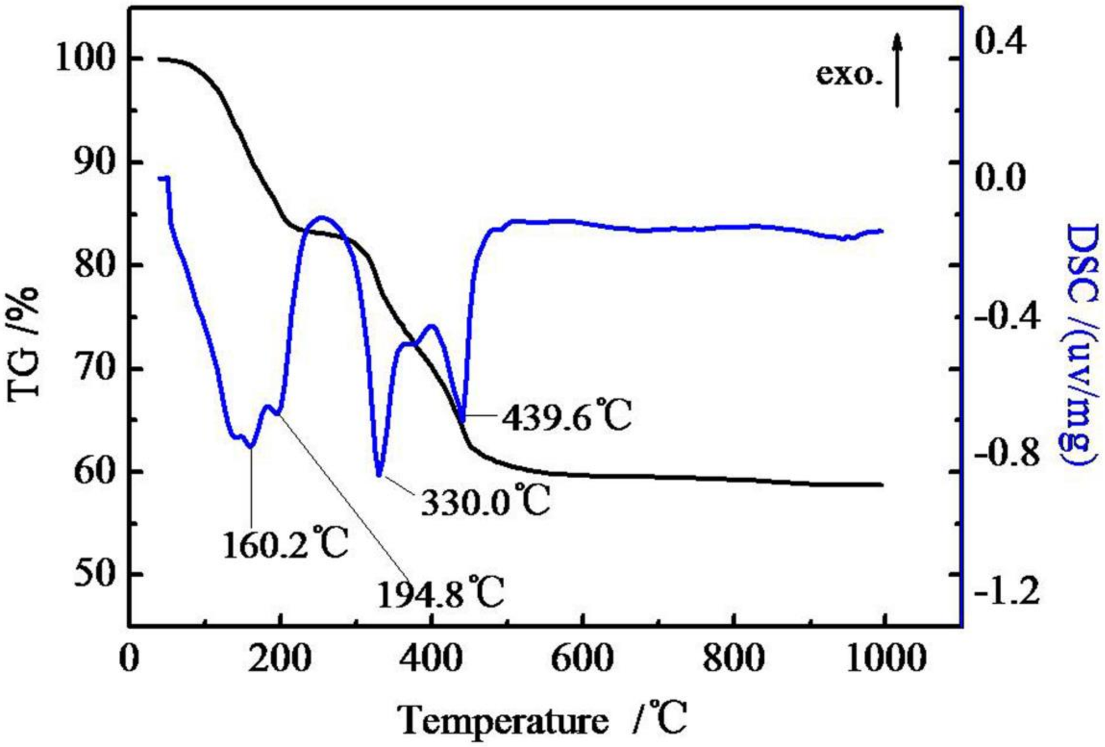

Fig. 2.6 TG-DSC curve of the MOC powder.

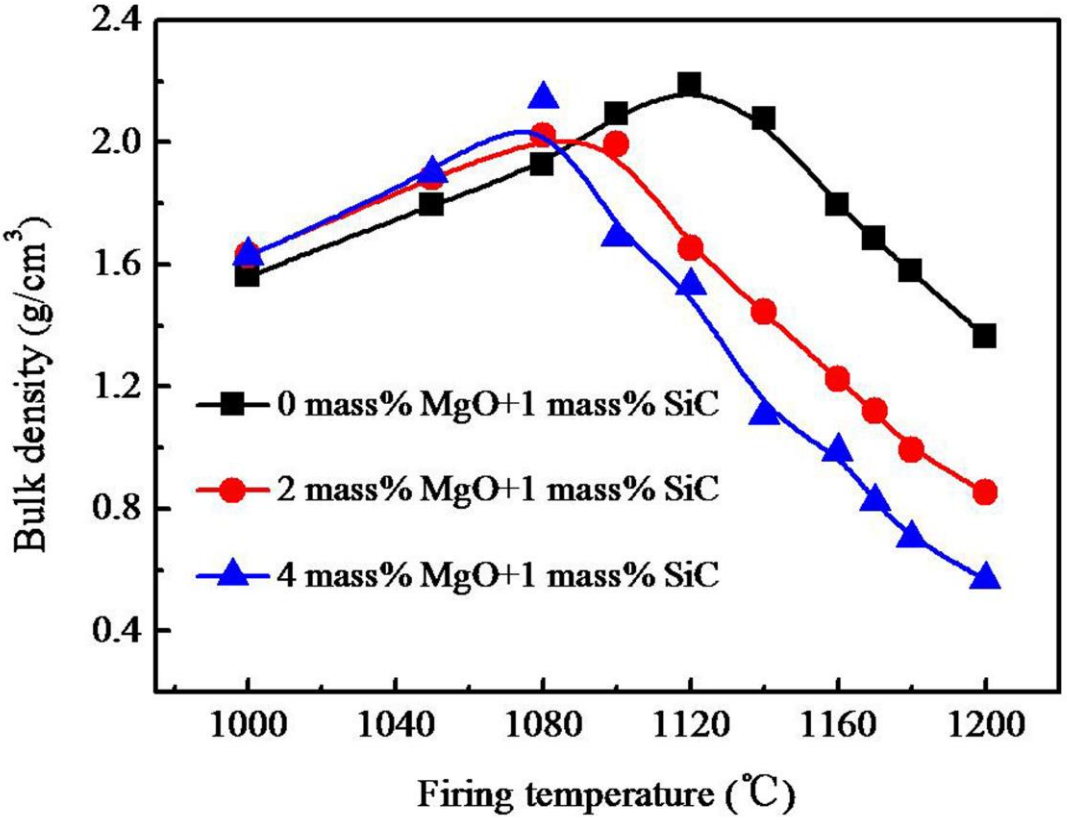

Fig. 2.7 Effect of firing temperature on the bulk densities of porcelain bodies with 1 mass% SiC and various MgO contents.

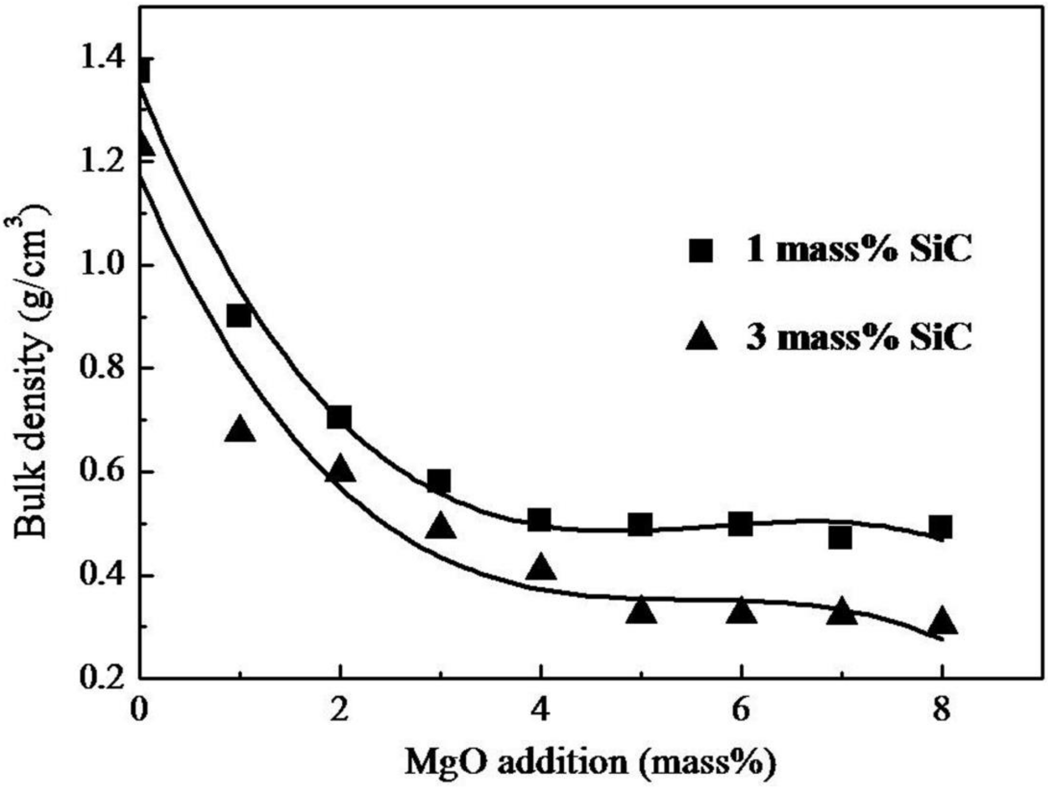

Fig. 2.8 Bulk density of fired porcelain body with different SiC content as a function of the MgO addition in the 0~8 mass% range at 1200℃.

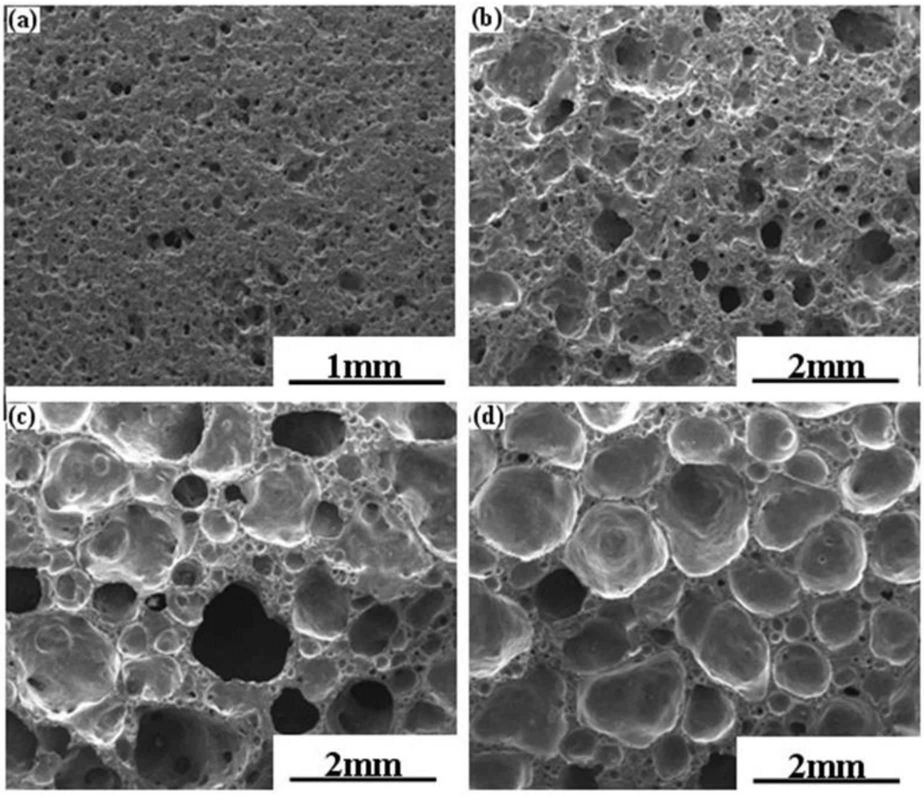

Fig. 2.9 SEM micrographs of the fired porcelain bodies with 1 mass% SiC: (a) 0 mass% , (b) 2 mass% , (c) 4 mass% , and (d) 6 mass% of MgO at 1200℃.

2.4 Conclusions

Porcelain green bodies with various MOC and silicon carbide (SiC) contents were fired at 1000~1200℃. The effects of MOC and SiC on the bulk density and microstructure were quantitatively investigated to clarify the foaming origin of PPR during firing.

A small amount of a mixture of both SiC and MOC caused the foaming of the fired porcelain body more significantly during firing rather than only SiC or MOC. The foaming of the fired porcelain body with only SiC during firing was more remarkable than that of the fired porcelain body with only MOC in the same content under the firing conditions. The MOC accelerated the foaming of fired porcelain body with SiC during firing. The foaming mechanism was explained as follow: a) SiC acts as a foaming agent due to its oxidation reaction to CO and CO2 gas generation at high temperature under alkaline molten salt conditions, and b) MOC serves as an alkaline molten salt due to its decomposition into MgO at high temperature and reduces the expansion resistance of the bubble formed in silicate liquid, resulting in a significant foaming of the porcelain green body during firing.

References

[1] M. M. Jorge, M. R. Jesus, R. Maximina, Journal of the European Ceramic Society 30 (2010) 3063–3069.

[2] E. Sanchez, J. Garcia-Ten, V. Sanz, A. Moreno, Ceramics International 36 (2010) 831–845.

[3] L. A. Diaz, R. Torrecillas, Journal of the European Ceramic Society 27 (2007) 2341–2345.

[4] H. J. Alves, M. R. Freitas, F. G. Melchiades, A. O. Boschi, Journal of the European Ceramic Society 31 (2011) 665–671.

[5] R. D. Gennaro, S. F. Graziano, P. Cappelletti, A. Colella, Environmental Science & Technology 43 (2009) 7123–7129.

[6] R. D. Gennaro, A. Langella, M. D. Amore, Applied Clay Science 41 (2008) 61–72.

[7] E. Rambaldi, L. Esposito, A. Tucci, G. Timellini, Journal of the European Ceramic Society 27 (2007) 3509–3515.

[8] E. Sanchez, M. J. Ibanez, J. Garcia-Ten, M. F. Quereda, Journal of the European Ceramic Society 26 (2006) 2533–2540.

[9] A. M. Bernardin, M. J. DaSilva, H. G. Riella, Materials Science and Engineering: A 37 (2006) 222–225.

[10] E. Bernardo, R. Cedro, M. Florean, S. Hreglich, Ceramics International 33 (2007) 963–968.

[11] G. M. Mclellan, E. B. Shand. Glass Engineering Handbook, McGraw-Hill Book Co. New York (1984) Chapter 19.

[12] E. Bernardo, L. Esposito, E. Rambaldi, A. Tucci, Journal of the European Ceramic Society 29 (2009) 2921–2927.

[13] A. Mueller, S. N. Sokolova, V. I. Vereshagin, Construction and Building Materials 22 (2008) 703–712.

[14] E. Bernardo, R. Cedro, M. Florean, S. Hreglich, Ceramics International 33 (2007) 963–968.

[15] E. Bernardo, Journal of the European Ceramic Society 27 (2007) 2415–2422.

[16] V. M. Sglavo, F. D. Genua, A. Conci, R. Ceccato, Journal of Materials Science 46 (2011) 6726–6733.

[17] S. P. Xia, P. F. Xing, S. Y. Gao, Thermochimica Acta 183 (1991) 349–363.

[18] W. D. Xiao, P. X. He, Journal of Fire Sciences 19 (2001) 369–377.

[19] J. Li, Z. X. Huang, Y. Zhao, Advanced Materials Research 66 (2009) 163–166.

[16] J. D. Kalen, R. S. Boyce, J. D. Cawley, Journal of the American Ceramic Society 74 (1991) 203–209.

[17] E. L. Williams, Journal of the American Ceramic Society 48 (1965) 190–194.

[18] K. Muehlenbachs, H. A. Schaeffer, Canadian Mineralogist 15 (1977) 179–184.

[19] J. L. Amoros, M. J. Orts, J. G. Ten, A. Gozalbo, Journal of the European Ceramic Society 27 (2007) 2295–2301.

[20] J. Garcia-Ten, A. Saburit, E. Bernardo, P. Colombo, Journal of the European Ceramic Society 32 (2012) 745–752.

[21] M. J. Orts, J. L. Amor´os, A. Escardino, A. Gozalbo, Applied Clay Science 8 (1993) 231–245.

[26] W. D. Kingery, Introduction to Ceramics, J Wiley & Sons, New York, 1976.

[27] E. M. Levin, C. R. Robbins, H. F. Mcmurdie, M. K. Reser, Journal of the American Ceramic Society (1964) 407–501.

[28] M. A. Lamkin, F. L. Riley, Journal of the European Ceramic Society 10 (1992) 347–367.

[29] H. P. Joo, J. M. Dong, Journal of Non-Crystalline Solids 337 (2004) 150–156.

[30] R. H. Doremus, J Non-Crystalline Solids 349 (2004) 242–247.

Chapter 3

Effect of SiC Particle Size and CaO content on Microstructure and Foaming Properties of Porcelain Ceramics

Abstract

Porcelain green bodies were prepared using porcelain stoneware tile powder as the major raw material, with silicon carbide (SiC) and CaO as additives. These were fired at 1000–1200 °C. The effects of SiC particle size and CaO content on the microstructure and foaming properties of porcelain ceramics were investigated in detail, with a view to further clarifying the dominant factors linking foaming behavior to SiC oxidation and phase composition during firing of a porcelain tile matrix. The results revealed that the size of the SiC particles has a significant influence on the number, size, and interconnectivity of the pores formed in the samples; this effect becomes more pronounced as the SiC particle size is reduced. The addition of a small amount of CaO is shown to significantly accelerate the foaming of a fired porcelain body containing SiC, but this effect is gradually inhibited by an increasing formation of anorthite. Based on these results, the foaming mechanism was discussed.

3.1 Introduction

Porcelain stoneware tile is a non-equilibrium material that is produced by the fast firing of kaolinitic clay, quartz, and feldspar mixtures [1]. In addition to providing a great resistance to wear, such tiles also exhibit a number of other interesting properties, such as an ability to withstand chemical attack, extremely low values of water absorption and excellent performance in frost and flexural tests. It is this combination of properties that has given porcelain stoneware tile the greatest increase in production and sales over recent years compared to all other ceramic building materials [2, 3]. In China alone, the production of porcelain stoneware tile has reached 4 Gm^2, representing more than half of all ceramic tile production [4].

In most instances, porcelain stoneware tile is surface-polished to improve its aesthetics and thereby increase its competitiveness with natural stone [5, 6]. In this process, long polishing lines are used to produce a flat and smooth final product with a high optical reflectivity; this typically consists of twenty or more polishing stages, with a steadily decreasing abrasive particle size from several hundred to just a few micrometers [7–9]. In all, this removes a layer of 0.4–0.8 mm in thickness from the surface of the porcelain stoneware tile, thus resulting in the generation of a large amount of polishing porcelain stoneware tile residue (PPR). Indeed, it has been reported that the output of PPR already exceeds 6 million tons per year in China [4]. Generally, these residues contain approximately 1–3 mass% of the abrasive used (most commonly silicon carbide), as well as 2–6 mass% of the magnesium oxychloride cement (MOC) used to adhere the abrasive to the polishing tool.

Disposal of PPR not only causes serious environment pollution, but also increases the consumption of mineral resources and their production cost; thus, the search for new recycling technologies is of great technological, economic, and environmental interest [10–13]. Bernardin et al [13] have previously demonstrated that porous ceramics can provide a highly valuable solution for thermal and acoustic insulation, since they generally possess a higher mechanical, chemical, and thermal stability than the polymeric foams currently employed. However, the costs associated with such porous ceramics have thus far presented a major impediment to their adoption by the building industry [14, 15]. There is, therefore, a definite economic and environmental benefit in finding the method of producing porous ceramics from PPR, as this should allow us much easier fabrication by foaming or bloating during firing [15–17].

Unfortunately, the commercial interest in porous ceramics from PPR has been accompanied by a scarcity of research. Although it is possible to find in the literature several papers on this issue, they are mainly focused on the feasibility of different raw materials to produce porous materials and more generalized information [13, 15-17]. As such, the foaming mechanism of PPR and its related influencing factors during firing have not yet been clearly understood. Furthermore, recent techniques have so far been unable to solve the landfill problem associated with PPR, because no fundamental research activity has been done to achieve the precise control of size and morphology of the material's porosity by making use of PPR. With this in mind, fundamental research was undertaken in our previous work that revealed the origin of PPR foaming during sintering is explained by the oxidation reaction of SiC particles [4]. Furthermore, this oxidation is accelerated by the presence of MOC, due to its decomposition into MgO at high temperature, thus resulting in a significant degree of foaming, even with porcelain green bodies that contain only a small amount of SiC [18]. However, the oxidation of SiC particles is a complex process that is still not fully understood. For instance, it is not known how the SiC particle size affects the foaming properties and microstructure of the porcelain tile matrix. On the other hand, it foams too drastically to get balanced porosity and mechanical strength during firing. To overcome this problem, crystalline phase with high mechanical properties was introduced. Particular attention was given to the anorthite ($CaO{\cdot}Al_2O_3{\cdot}2SiO_2$), the presence of which can produce superior mechanical properties of the final product [19,20]. But it is not known whether or how the phase composition affects the overall reaction of SiC particles in the porcelain tile matrix, and subsequent foaming properties and microstructure, thus affording significant opportunities for research in this field.

The objectives of this chapter are therefore to carry out a detailed study to make clear the effect of SiC particle size and crystallization of anorthite on the microstructure and foaming properties of porcelain ceramics. For this purpose, SiC of various particle sizes and different amount of CaO addition were used. In this way, it is expected to further clarify the relationship among foaming behavior, phase composition and SiC oxidation during firing of a porcelain tile matrix, with a view to the development of improved control technologies.

3.2 Experimental procedure

3.2.1 Sample preparation

The porcelain stoneware tile powder used as the main raw material for this study was obtained by shattering and planetary-milling porcelain stoneware tile (Newpearl Ceramics Co. Ltd., Guangdong, China) for 45 minutes. Its chemical composition is shown in Table 3.1.

Silicon carbide particles (Haixu abrasive Co., Ltd., Zhengzhou, China), with a purity of more than 99.8 mass%, were used as an additive to represent the typical abrasive particle used in porcelain stoneware tile polishing. The abrasive particle size was defined using the standard mesh-size designation, with the sequence used of 120, 200, 400, 600, 1000, and 2000 corresponding to an average particle size (as measured from SEM images) of 125, 85, 45, 25, 15, and 8 μm, respectively. CaO (AR, Tianjin Changlu Hangu Saltworks Co. Ltd., China) was also used an additive. Slurries of porcelain stoneware tile powder containing 1 mass% SiC of various particle sizes, or CaO and 1 mass% SiC (average particle size 45μm), were prepared with mixture of distilled water and 0.5 mass% of polyethylene glycol (PEG-400 binder, Guangzhou Taiqi Chemical Technology Co., Ltd., China) at the ratio of 0.8:1. These slurries were then planetary-milled for 30 minutes, with the raw material powders subsequently prepared by drying, granulating, and sieving with a 30 mesh sieve (550 μm). Porcelain green bodies of 35 mm in diameter and 5 mm in thickness were formed by dry-pressing the raw powder materials powders at 15 MPa, and then fired in an electric furnace under an air atmosphere at 1000–1200 °C for 20 minutes at a heating rate of 5 °C/min.

3.2.2 Sample characterizations

The water absorption, bulk density and apparent porosity of the fired samples were measured according to the ASTM C373-88. The total porosity of the sample, ε_T (%) was determined by the following equation:

$$\varepsilon_T = (1 - \frac{d_b}{d_r}) \times 100 \tag{3.1}$$

where d_b and d_r are the bulk and true densities of the fired sample, respectively. In which d_r was previously measured according to ASTM C329-88. The test method involves crushing, grinding and sieving of the sample to pass - 80 mesh (177 μm). The measurements were carried out on 8-10 g of powder sample by using a pycnometer (50 ml capacity) consisting of a suitable bottle with a capillary tube stopper. All determinations have been made in duplicate.

To assess the porosity evolution during firing, the microstructures of the fired specimens were examined by scanning electron microscopy (SEM, Philips L30FEG, The Netherlands). Image analysis software (Image-Pro Plus6.0, Media Cybernetics, USA) was used to determine the average particle size of SiC from these SEM images. The crystalline phases of the fired specimens were identified by X-ray diffraction (XRD, Philips PW-1710 model X-ray diffractometer, the Netherlands) using Cu K_α radiation.

Table 3.1 Chemical compositions of the porcelain stoneware tile powder.

	IL[a]	SiO_2	Al_2O_3	Fe_2O_3	TiO_2	CaO	MgO	K_2O	Na_2O
Porcelain tile powder (mass%)	0.6	69.01	22.29	0.44	0.17	0.54	0.48	1.35	4.93

[a] Ignition loss

3.3 Results and discussion

3.3.1 Effect of silicon carbide particle size on foaming

Fig. 3.1 shows the effect of firing temperature on the bulk density of a sample without SiC, and those with 1 mass% SiC of different particle sizes. As can be seen, the particle size of the SiC powder has a tremendous influence on the foaming of porcelain ceramics during firing. Moreover, the bulk density of samples without SiC gradually increased with an elevation in the firing temperature, reaching a maximum value of 2.42 g/cm^3 at 1180–1200 °C that is equivalent to the general density of densified porcelain stoneware tile. However, the bulk density of the samples containing 45 μm SiC particles initially increased with temperature, reaching a maximum value of 2.11 g/cm^3 at about 1120 °C, but then abruptly decreased with any further increase in the firing temperature. A similar tendency was also observed in the case of samples containing 8 μm SiC particles, but the transition temperature was reduced to about 1080 °C.

Fig. 3.2 shows SEM images of samples containing 1 mass% of 8 or 45 μm SiC particles fired at 1100 °C. From Fig. 3.2 (a) and (b), it is clear that a smaller SiC particle size produces a larger number of pores. Conversely, a greater SiC particle size (45 μm) produces a smooth surface with very little bubbling, as shown in Fig. 3.2 (c) and (d).

This phenomenon is likely related to the oxidation kinetics of SiC in a porcelain ceramic matrix. In porcelain stoneware tile, a minor crystalline phase formed by mullite and quartz crystals becomes immersed in a vitreous phase that is formed by a siliceous glass containing alkaline and earth alkaline oxides, mainly K_2O, Na_2O, and MgO [2, 5, 18]. These oxides have a significant corrosive effect on the SiO_2 protective layer normally formed on the surface of SiC particles, which in turn leads to a substantial increase in the chemical reaction between SiC and oxygen. The effect of this is that a large amount of CO_2 and CO gas can be generated at relatively low temperatures (900–1100 °C) [21–23]. Given that a large amount of liquid phase is generated in a fired porcelain body above 1100 °C, it becomes increasingly difficult for this gas to discharge outward. With more gas remaining in the liquid, closed pores are generated, which explains the observed reduction in density.

It was also revealed that the stability of the SiO_2 protective layer formed on the surface of SiC particles is strongly influenced by the SiC particle size [24]. That is, when a finer SiC powder is used, the thickness of the SiO_2 protective layer is insufficient to adequately protect the SiC particles from corrosion, with the increased oxidation subsequently resulting in greater gas evolution (CO and CO_2) and foaming. Conversely, when a coarser SiC powder is used, the thicker SiO_2 coating is more stable and therefore acts as a diffusion barrier to the reaction between the porcelain green body matrix and SiC particles that reduces the formation of bubbles. A similar phenomenon was observed by He et al. [25], in which the onset-temperature for significant oxidation of a finer SiC powder was found to be much lower than that of a SiC powder with a relatively larger particle size.

Any subsequent increase in temperature reduces the effective viscosity, which can deform the porcelain body and thereby increase the occluded pore gas pressure (P_g) above the capillary pressure (P_c). If this occurs, then the porcelain body expands, thus explaining the observed significant reduction in bulk density with increasing firing temperature. The firing process for this type of material is expressed by [26, 27]

$$-\frac{d\varepsilon}{\varepsilon dt} = \frac{3}{4\eta_s}(P_c - P_g) \tag{3.2}$$

where ε is the porosity, t is the temperature, η_s is the effective viscosity of the system, P_g

is the occluded pore gas pressure, and P_c is the capillary pressure; the latter is given as $P_c = -2\gamma/r$, where γ is the surface tension and r is the radius of the pores.

Fig. 3.3 shows the influence of SiC particle size on the bulk density and water-absorption of samples fired at 1200 °C, demonstrating that SiC particle sizes above 25 μm have no significant influence on either the bulk density or water-absorption. However, when using SiC particle sizes smaller than 25 μm, the samples exhibit a rapidly decreasing value of bulk density and much higher water-absorption with the decrease of SiC particle size. This behavior is attributable to the greater expansion provided by SiC, as the increase of specific surface area enables more effective oxidation and gas generation.

Fig. 3.4 shows SEM images of samples with various SiC particle sizes fired at 1200 °C. From this figure, it is evident that when the SiC particle size is varied, the number, size, and interconnectivity of the pores formed are similarly varied. A reduction in SiC particle size from 125 to 25 μm therefore leads to a greater number of pores and reduction in pore size, as shown in Fig. 3.4 (b), (c) and (d). This can be explained by the presence of a greater number of SiC particles, with a smaller geometric surface area for each particle, as the particle size reduced. An exception is evident in the case of the sample prepared with the finest SiC particle size, as shown in Fig. 3.4(a), which developed larger and more irregular pores with a higher level of interconnectivity than we expected. This may be due to the aforementioned fact that the chemical activity increased through the use of a finer SiC particle size, with the increased oxidation of SiC and the CO_2/CO gas generation producing a greater number of pores that are more readily connected to form larger pores.

Clearly, the use of fine SiC particles yields samples with a high total porosity (low bulk density), yet also leads to a more open porosity that could further affect the properties of the final product, e.g., its stain and frost resistance. However, when the SiC particle size is in the range of 25–125 μm, the bulk density and water absorption showed almost constant values.

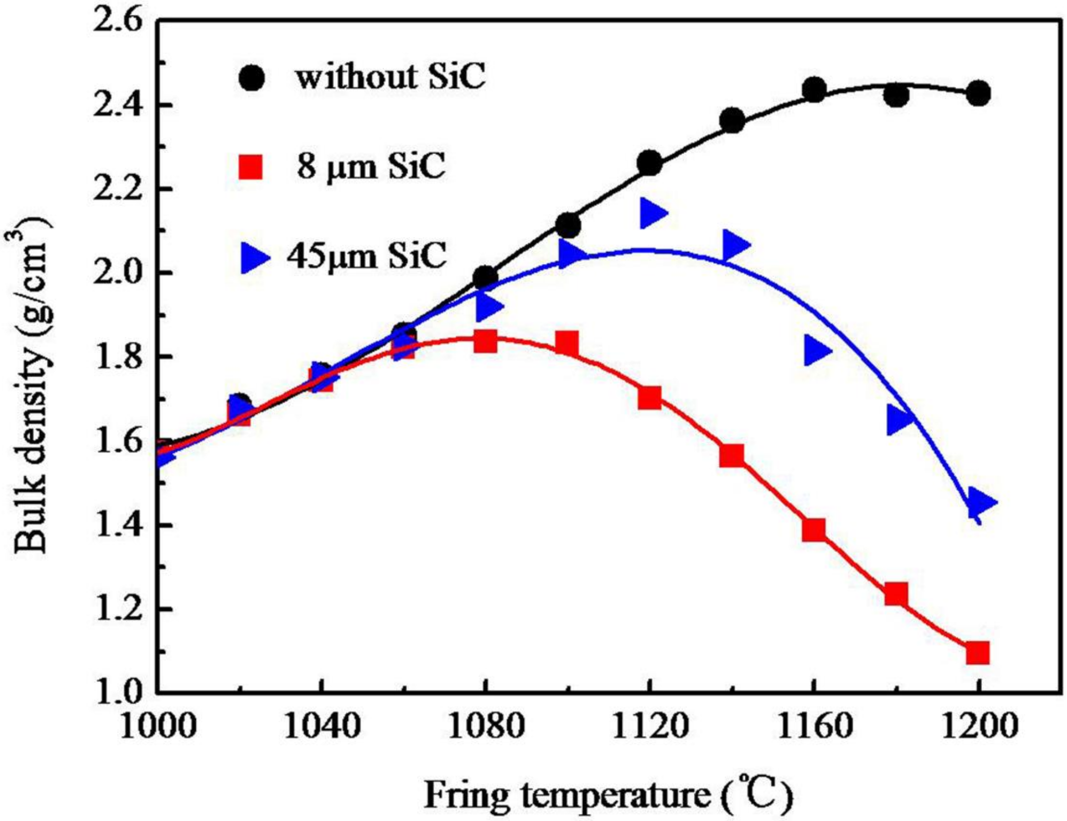

Fig. 3.1 Change in the relationship between bulk density and firing temperature for porcelain with the addition of SiC particles of different sizes.

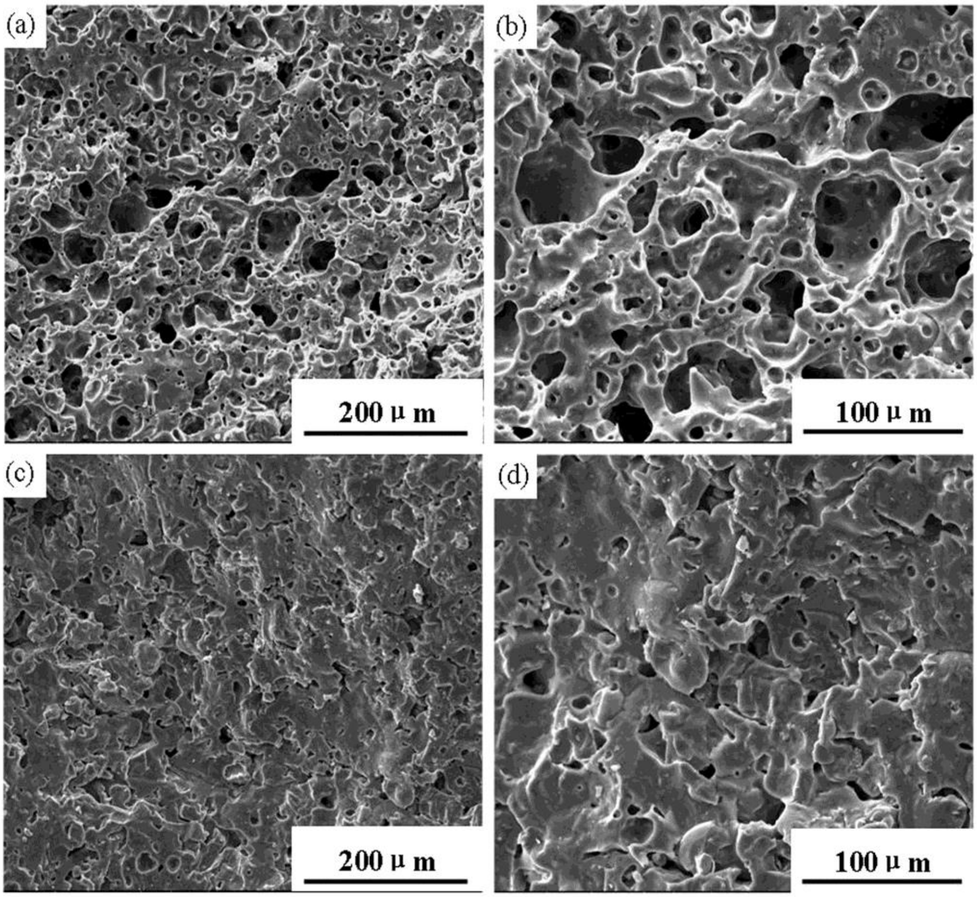

Fig. 3.2 SEM images of porcelain containing (a–b) 8 μm and (c–d) 45 μm SiC particles fired at 1100 °C.

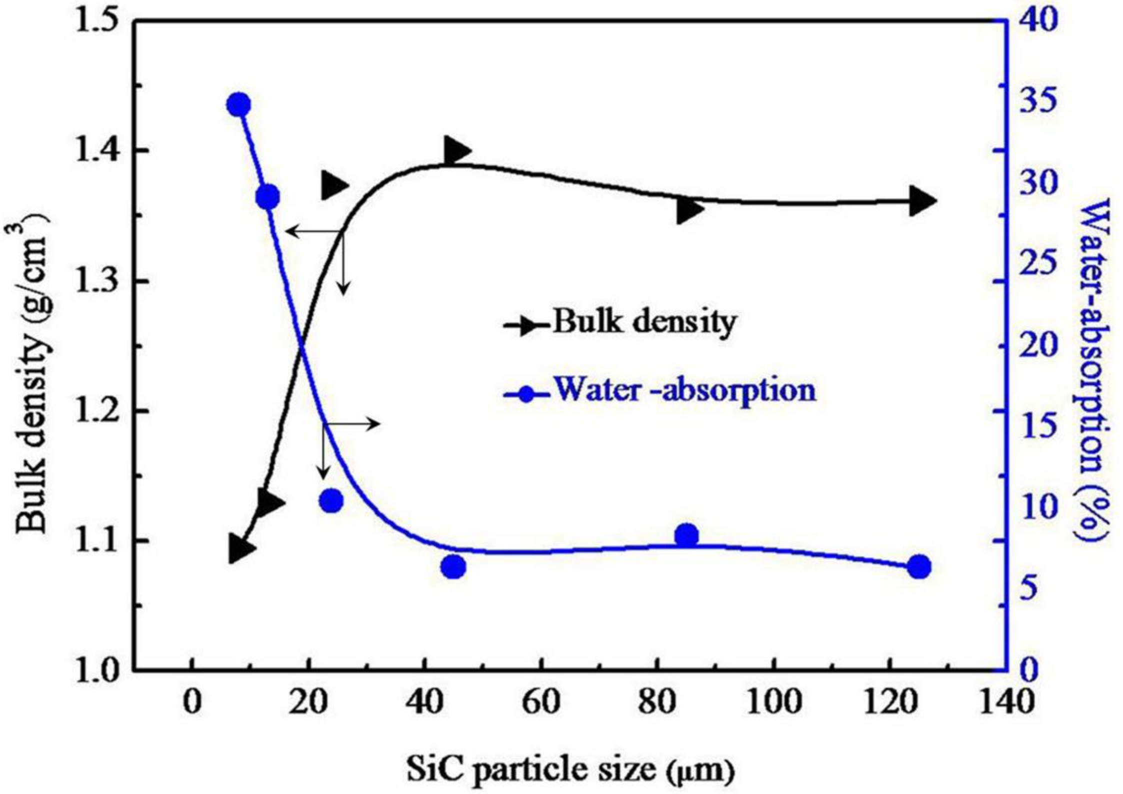

Fig. 3.3 Bulk density and water absorption of porcelain as a function of SiC particle size fired at 1200 °C.

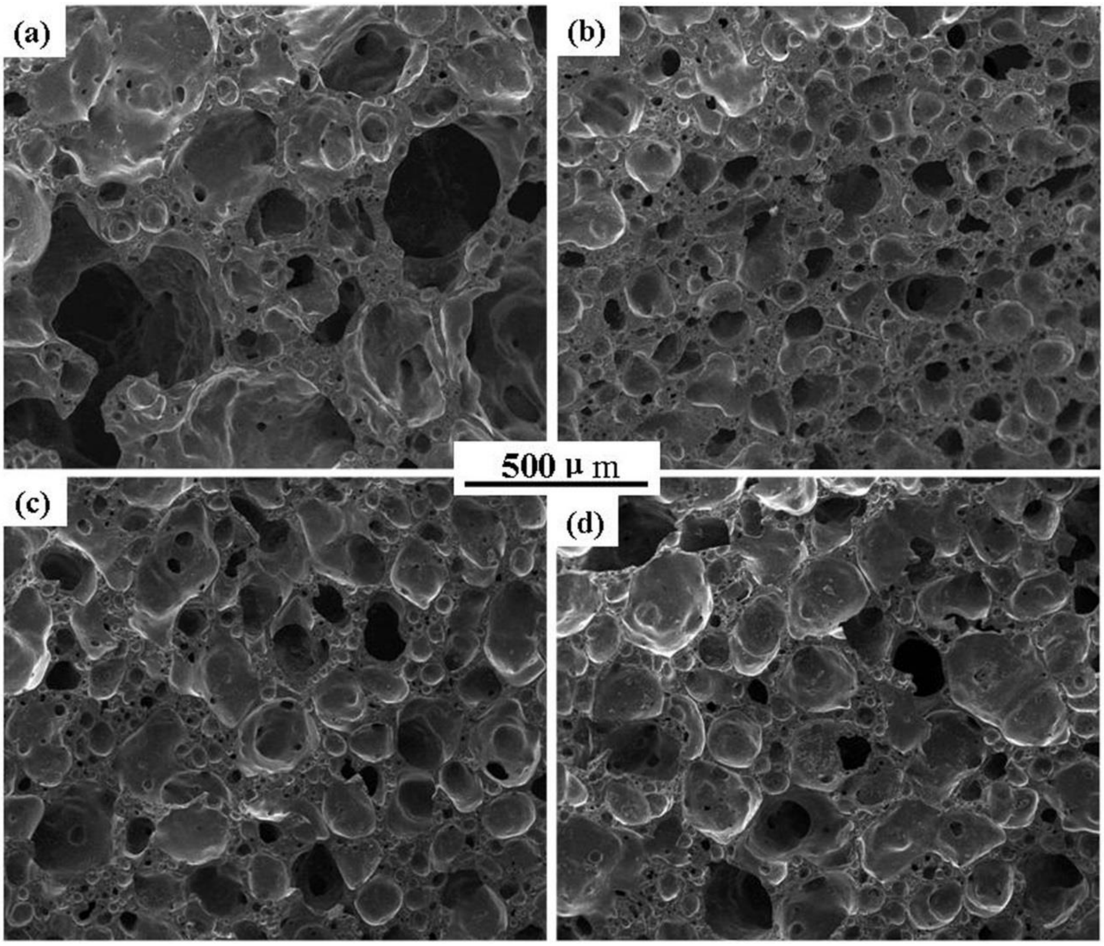

Fig. 3.4 SEM images of porcelain with SiC particle sizes of (a) 8 μm, (b) 25 μm, (c) 85 μm, and (d) 125 μm fired at 1200 °C.

3.3.2 Effect of CaO content on foaming

Fig. 3.5 shows the effect of CaO content on the bulk density and total porosity of samples containing 1 mass% SiC fired at 1200 °C. We can see from this that the bulk density initially reduced to the minimum value of 0.80 g/cm^3 (total porosity about 68%) as the CaO addition increased to around 2 mass%, then abruptly increases with further CaO addition. However, this increase of the bulk density becomes insignificant once the amount of CaO addition reaches 5–7 mass%.

Fig. 3.6 shows SEM images of samples with 1 mass% SiC and different amounts of CaO fired at 1200 °C. It is clearly evident from this that in the presence of a small amount of CaO (2 mass%), the pore size notably augmented compared with a sample to which no CaO is added. The pore size does, however, reduce with any further increase in the amount of CaO, as shown in Fig. 3.6 (c) and (d). This observation is quite consistent with the variation of bulk density and total porosity as shown in Fig. 3.5.

The foaming temperature and foaming rate of the fired samples, on the other hand, is significantly influenced by the amount of CaO addition. As shown in Fig. 3.7, the presence of just a small amount of CaO (2 mass%) causes the transition temperature of maximizing the bulk density around 1080 °C, while the bulk density rapidly reduced with the increase of firing temperature. However, this reduction in the bulk density becomes insignificant once the amount of CaO addition increased to 4 mass%.

These variations may be related to the phase evolution of the samples with the increase of CaO addition, as shown in Fig. 3.8. This demonstrates that when a small amount of CaO is added, the crystalline phase of the sample did not notably change; instead, the major crystalline phases remain as quartz (SiO_2) and mullite ($3Al_2O_3{\cdot}2SiO_2$), as shown in Fig. 3.8 (a) and (b). However, when the amount of CaO addition is greater than 2 mass%, the relative intensity of the peaks corresponding to mullite and quartz phases reduced, whereas that of anorthite ($CaO{\cdot}Al_2O_3{\cdot}2SiO_2$) appears and its intensity progressively increased with further CaO addition.

This phase evolution can be understood by considering the effect of CaO on the degree of polymerization (DOP) of the silicates. It is already well known that CaO behaves as a classic network modifier in silicate networks, disrupting the continuity of the silicate structure due to the breakage of Si-O bonds with the formation of non-bridging oxygen. This reduces the DOP of the silicates, thus lowering the temperature required for the formation of a liquid phase [28] and the oxidation of SiC thus leading to the generation of CO_2 and CO gas. This decrease in DOP is also associated with physical and chemical changes, such as a reduced viscosity [29, 30]. On the one hand, this can accelerate the oxygen migration in the liquid silicate [29–31] and thereby facilitate SiC oxidation to generate more gas, but on the other hand, the expansion resistance of the stoma formed in the silicate liquid becomes smaller, thereby resulting in a significant decrease in the bulk density with increased firing temperature, as shown (2 mass% CaO+ 1 mass% SiC) in Fig. 3.7. This effect is similar to that observed in the sample with a small amount of MOC or MgO [18].

When the amount of CaO addition increased, however, depolymerization of the silicates facilitates rapid heterogeneous nucleation and growth of crystalline anorthite from anorthite composition melts and glasses [32], as shown in Fig. 3.8 (c) and (d). The formation of this anorthite phase is accompanied by a substitution of Al^{3+} + $1/2Ca^{2+}$ for Si^{4+} in the silicate network, thus resulting in a strengthening of the structural network by Ca^{2+}; hence, the formation of larger clusters is favored. Consequently, the DOP of the silicate network increased, and the diffusion of structural units (e.g., tetrahedral groups and Ca^{2+} ions) in the melt becomes more difficult as the formation of anorthite increases [33, 34]. Ultimately, the expansion resistance of the stoma formed in the silicate liquid becomes greater, and the oxidation of SiC particles in the porcelain ceramic matrix may be inhibited, thus resulting in an insignificant decrease in bulk density with increasing firing temperature.

This indicates that the partial crystallization of anorthite has a remarkable effect in terms of limiting the expansion, despite the fact that they represent a superior strength phase in the composition. This is important information for the careful control of phase composition to achieve a desirable porosity and microstructure. It is therefore believed that this work will have important scientific value in the further understanding and control of the foaming process of PPR during its recycling. However, this is merely just an important first-step toward the effective recycling of porcelain stoneware tile residue, with more detailed studies warranted if this becomes standard practice in future.

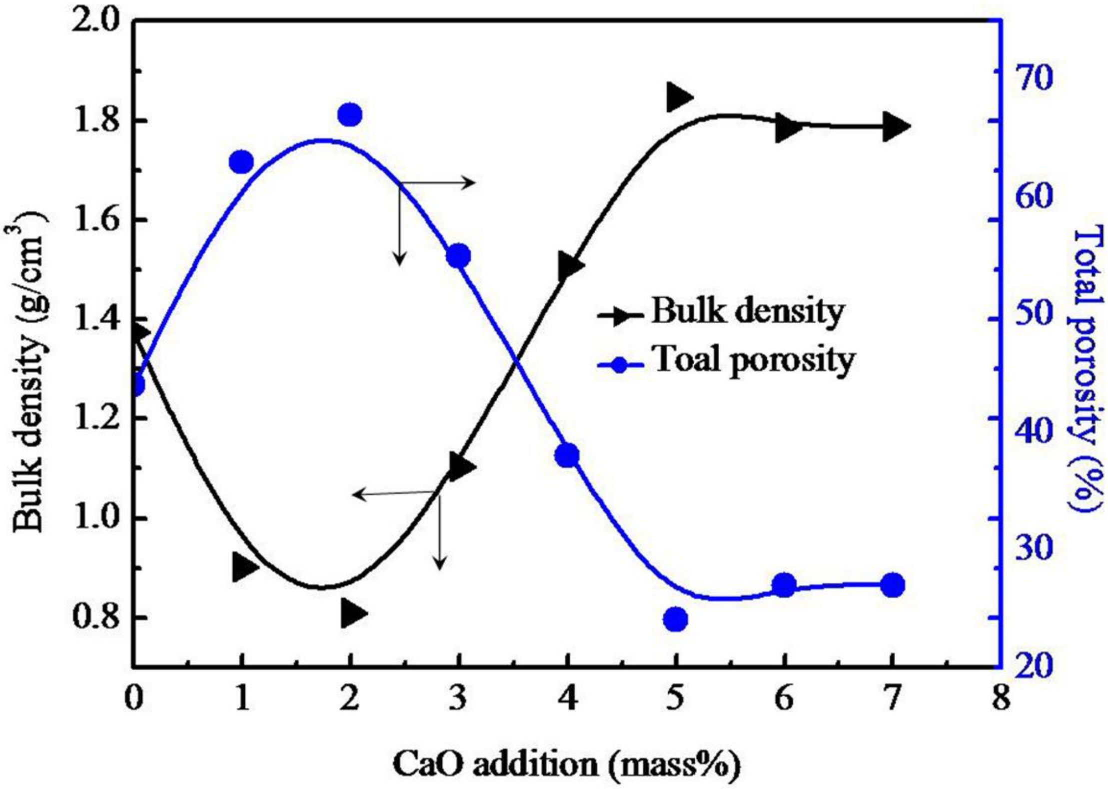

Fig. 3.5 Effect of the addition of CaO on the bulk density and total porosity of porcelain containing 1 mass% SiC fired at 1200 °C.

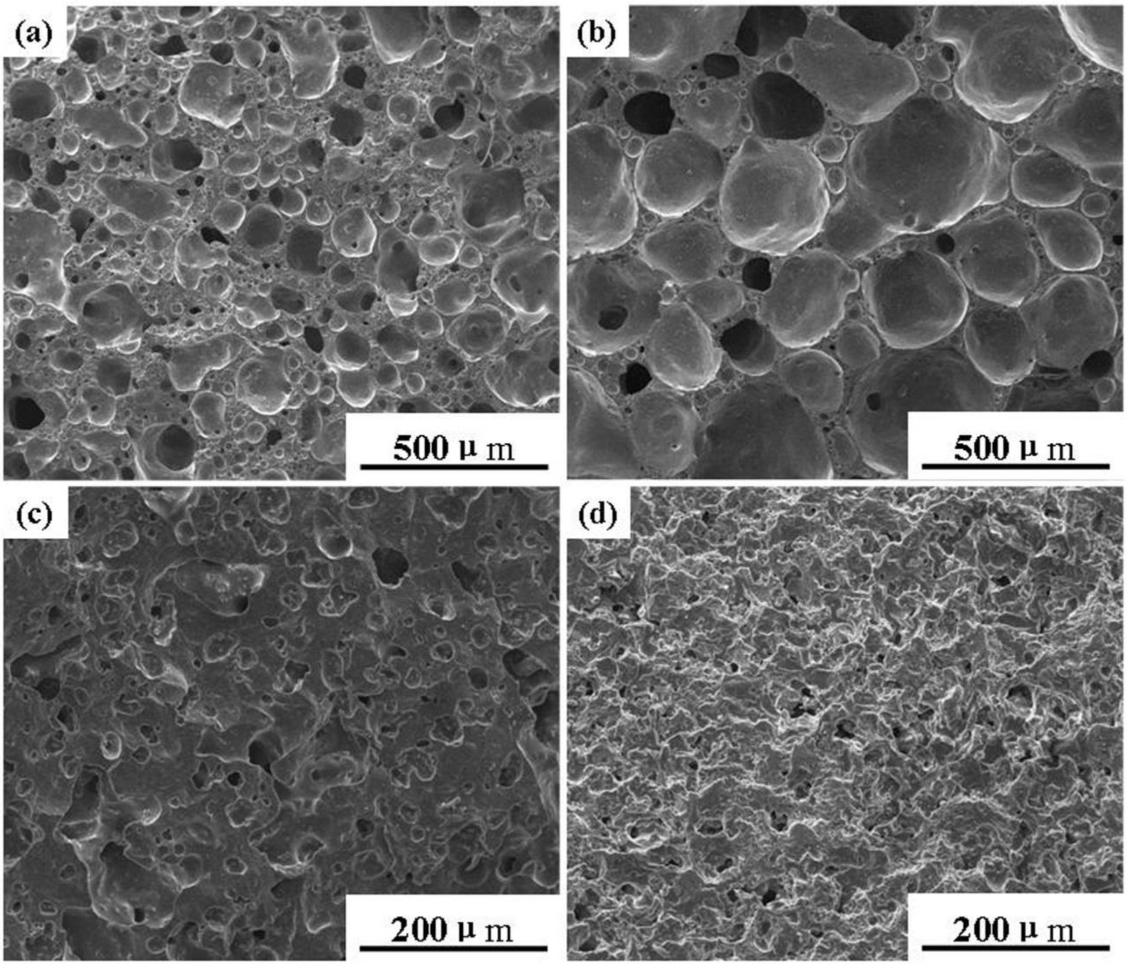

Fig. 3.6 SEM images of porcelain with (a) 0 mass%, (b) 2 mass%, (c) 4 mass%, and (d) 6 mass% CaO addition fired at 1200 °C.

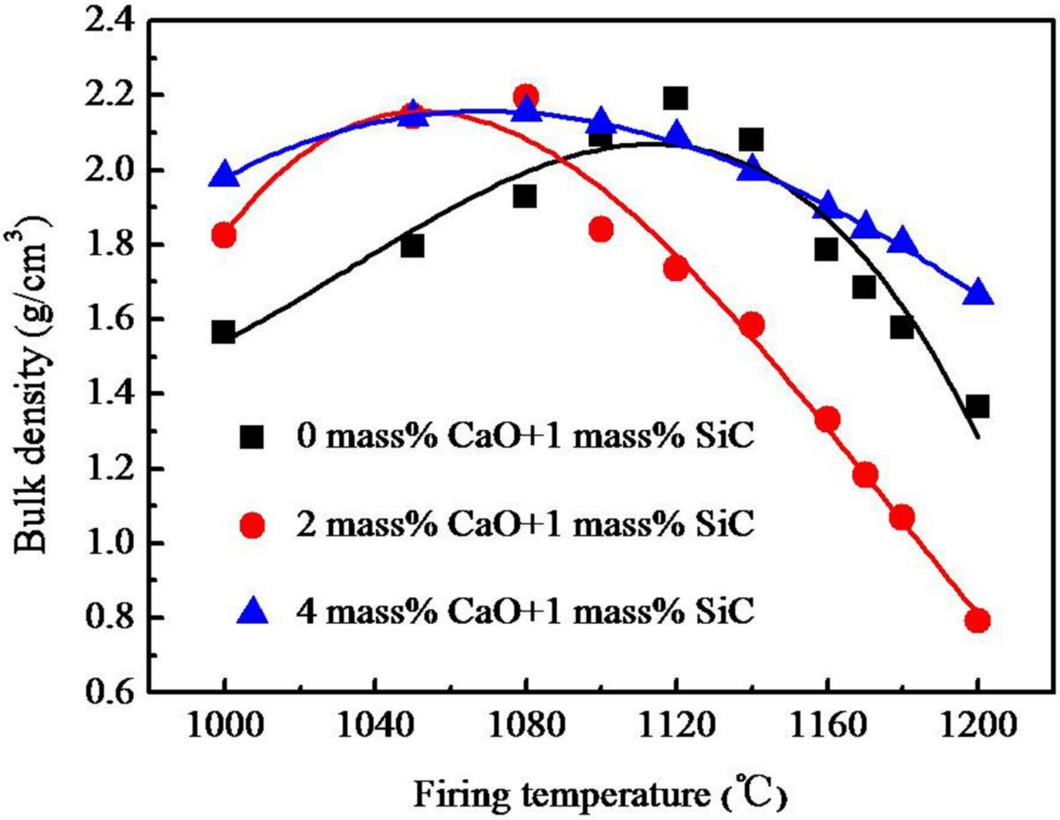

Fig. 3.7 Relationship between the bulk density and firing temperature of porcelain with 1 mass% SiC and different amounts of CaO.

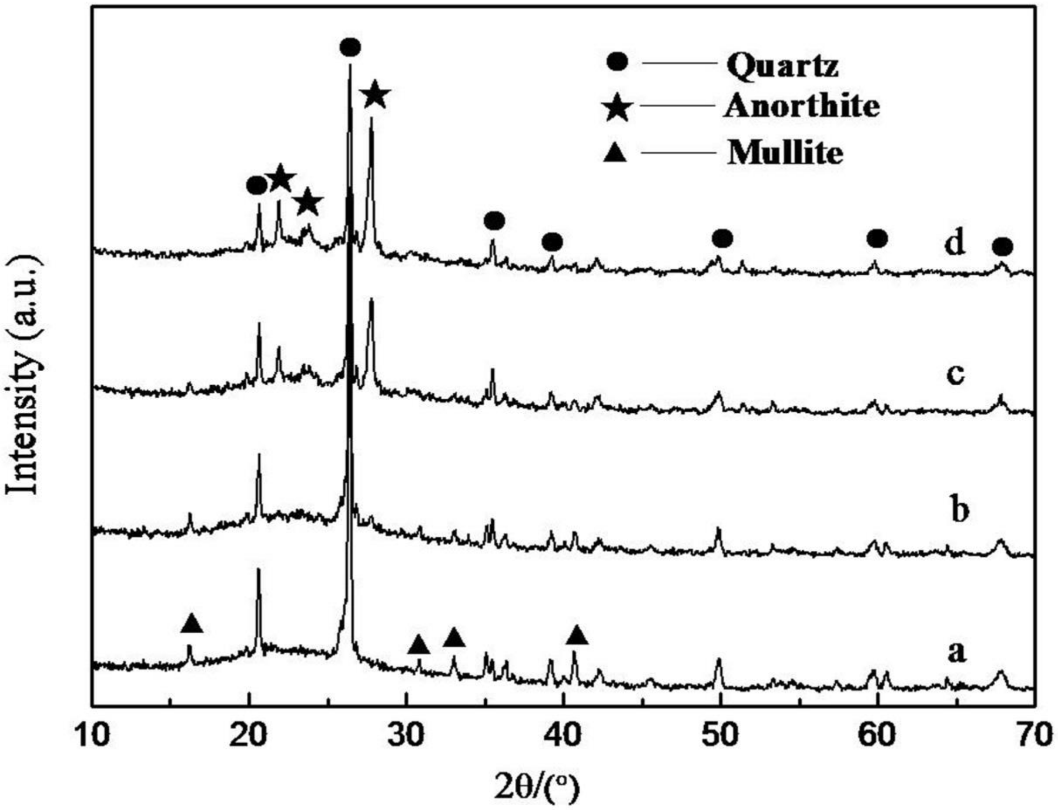

Fig. 3.8 XRD data for porcelain with (a) 0 mass%, (b) 2 mass%, (c) 4 mass%, and (d) 6 mass% CaO addition.

3.4 Conclusions

The size of SiC particles added to a porcelain matrix was found to have a significant influence on the number, size, and interconnectivity of the pores formed in the resulting product, with this effect becoming more pronounced as the SiC particle size reduced. When the SiC particle size is in the range of 25–125 μm, the use of an equal mass percent of SiC has no significant influence on the bulk density or water-absorption. However, using SiC particles less than 25 μm in size resulted in the rapidly decreased value of bulk density, and a much higher water-absorption. This was attributed to a greater expansion of the SiC, with the subsequent increase in specific surface area enabling a more effective oxidation and gas generation. On the other hand, the addition of a small amount of CaO also significantly accelerated the foaming properties of a porcelain green body with SiC, though the foaming rate was notably inhibited by the increase of anorthite.

References

[1] C. Leonelli, F. Bondioli, P. Veronesi, M. Romagnoli, T. Manfredini, G. C. Pellacani, V. Cannillo, Journal of the European Ceramic Society 21 (2001) 785–793.

[2] M. M. Jorge, M. R. Jesus, R. Maximina, Journal of the European Ceramic Society 30 (2010) 3063–3069.

[3] E. Sanchez, J. Garcia-Ten, V. Sanz, A. Moreno, Ceramics International 36 (2010) 831–845.

[4] A. Z. Shui, X. A. Xi, Y. M. Wang, X. S. Cheng, Ceramics International 37 (2011) 1557–1562.

[5] E. Sanchez, M. J. Ibanez, J. Garcia-Ten, M. F. Quereda, I. M. Hutchings, Y. M. Xu, Journal of the European Ceramic Society 26 (2006) 2533–2540.

[6] M. Dondi, G. Ercolani, G. Guarini, C. Melandri, M. Raimondo, E. Almendra, P. Cavalcante, Journal of the European Ceramic Society 25 (2005) 357–365.

[7] I. M. Hutchings, K. Adachi, Y. Xu, E. Sanchez, M. J. Ibanez, M. F. Quereda, Journal of the European Ceramic Society 25 (2005) 3151–3156.

[8] L. Esposito, A. Tucci, D. Naldi, Journal of the European Ceramic Society 25 (2005) 1487–1498.

[9] M. Hutchings, Y. Xu, E. Sanchez, M. J. Ibanez, M. F. Quereda, Journal of Materials Science 40 (2005) 37–42.

[10] R. D. Gennaro, A. Langella, M. D. Amore, Applied Clay Science 41 (2008) 61–72.

[11] E. Rambaldi, L. Esposito, A. Tucci, G. Timellini, Journal of the European Ceramic Society 27 (2007) 3509–3515.

[12] E. Sanchez, M. J. Ibanez, J. Garcia-Ten, M. F. Quereda, Journal of the European Ceramic Society 26 (2006) 2533–2540.

[13] A. M. Bernardin, M. J. DaSilva, H. G. Riella, Materials Science and Engineering: A 37 (2006) 222–225.

[14] S. Hasheminia, A. Nemati, B. E. Yekta, P. Alizadeh, Ceramics International 38 (2012) 2005–2010.

[15] E. Bernardo, R. Cedro, M. Florean, S. Hreglich, Ceramics International 33 (2007) 963–968.

[16] A. Mueller, S. N. Sokolova, V. I. Vereshagin, Construction and Building Materials 22 (2008) 703–712.

[17] A. M. Bernardin, M. J. Silva, H. G. C. Silva, H. G. Riella, Proc Qualicer (2006) 189–196.

[18] X. A. Xi, A. Z. Shui, Y. F. Li, Y. M. Wang, H. Abe, M. Naito, Journal of the European Ceramic Society 32 (2012) 3035–3041.

[19] M. U. Taskiran, N. Demirkol, A. Capoglu, Journal of the European Ceramic Society 25 (2005) 293–300.

[20] J. F. Wu, Z. Li, Y. Q. Huang, F. Li, Ceramics International 39 (2013) 7743–7750.

[21] N. S. Jacobson, Journal of the American Ceramic Society 69 (1986) 74–82.

[22] D. X. Fox, J. L. Smialek, Journal of the American Ceramic Society 73 (1990) 303–311.

[23] M. K. Feber, J. Ogle, V. J. Tennery, V. Henson, Journal of the American Ceramic Society 68 (1985) 191–197.

[24] M. Villegas, T. Sierra, F. Lucas, J. F. Fern´andez, A. C. Caballero, Journal of the European Ceramic Society 27 (2007) 861–865.

[25] J. Y. He, C. B. Ponton, Journal of Materials Science 43 (2008) 4031–4041.

[26] J. Garcia-Ten, A. Saburit, E. Bernardo, P. Colombo, Journal of the European

Ceramic Society 32 (2012) 745–752.

[27] M. J. Orts, J. L. Amor´os, A. Escardino, A. Gozalbo, Applied Clay Science 8 (1993) 231–245.

[28] W. D. Kingery, Introduction to Ceramics, J. Wiley & Sons, New York, 1976.

[29] M. A. Lamkin, F. L. Riley, Journal of the European Ceramic Society 10 (1992) 347–367.

[30] H. P. Joo, J. M. Dong, Journal of Non-Crystalline Solids 337 (2004) 150–156.

[31] R. H. Doremus, J Non-Crystalline Solids 349 (2004) 242–247.

[32] B. H. W. S. DeJong, C. M. Schramm, V. E. Parzizle, Geochimica et Cosmochimica Acta 48 (1984) 2619–2629.

[33] M. Solvang, Y. Z. Yue, S. L. Jensen, D. B. Dingwell, J Non-Crystalline Solids 336 (2004) 179–188.

[34] M. Moesgaard, Y. Z. Yue, J Non-Crystalline Solids 355 (2009) 867–873.

Chapter 4

Novel Co-precipitation Method to Synthesize NiO-YSZ Nanocomposite Powder for Solid Oxide Fuel Cell

Abstract

As the Ni composition, particle size and its homogeneous distribution in the SOFC anode of Ni-yttria stabilized zirconia (YSZ) composite are important factors in electrochemical performance, better control of the properties of NiO-YSZ nanocomposite particles as starting powder materials is essential for higher SOFC performance. In this study, their novel co-precipitation method was developed. It was applied the interaction of anionic Zr carbonate complex with cationic Ni and Y ions to achieve its uniform sedimentation. As a result, NiO-YSZ nanocomposite particles with their uniform size were successfully obtained at a facile condition with almost 100% yield. The Ni/YSZ anode was fabricated by screen-printing the paste made by the NiO-YSZ nanocomposite particles and its sintering at 1350℃ and subsequent reduction. The anode had a uniform porous structure consisting of fine grains in the range of 200~400nm, and exhibited low polarization resistance of 0.62, 0.34 and 0.23 $\Omega \cdot cm^2$ at 700℃, 750℃and 800℃, respectively.

4.1 Introduction

Nickel-Yttrium stabilized zirconium (Ni-YSZ) cermet is the most widely used anode material for solid oxide fuel cells (SOFCs) mainly due to its high mechanical strength, long-term reliability as well as cost factors. Recent research and development on SOFCs have been directed to lower operation temperature from about 1000℃ down to the intermediate range of 650~800℃, with the aim of cost reduction and durability enhancement of cells and systems [1]. For lower operation temperature, a major challenge of the Ni/YSZ anode is to achieve lower polarization loss to maintain sufficiently high electrochemical activity, because low temperature leads to low oxygen ion conductivity of YSZ and low reaction kinetics for hydrogen oxidation [2].

Previous fundamental studies revealed that the polarization resistance of the Ni-YSZ anode depends strongly not only on its nickel content but also on its microstructure [3]. The microstructure affects the length of Ni-YSZ-gas tripe phase boundary (TPB), where the electrochemical reaction occurs. The length of TPB correlates well with the reaction rate for the electrochemical oxidation of hydrogen [4]. Longer TPB length enhances the electrochemical reaction and reduces the polarization resistance of anode. For its achievement, the grain size and its distribution of Ni and YSZ in the anode must be controlled in nanosized ranges [5, 6].

It has been reported that the build-up process including gel combustion [7], spray pyrolysis [8], co-precipitation [9], sol-gel [10], polymeric complexing [11] and hydrothermal methods [12] had the advantage in the production of homogeneous multi-component and nanocomposite particles. In these processes, the co-precipitation method has been found particular interest because of its simplicity, cost-effective and easy scale-up capability. Moreover, owing to the low solubility of Ni in the YSZ lattice, the NiO/YSZ powders derived by such chemical method will consist of individual YSZ and NiO particles [13]. However, the grain size was still limited to 1 μm or more in the state-of-the-art Ni/YSZ anode derived from the NiO/YSZ composite particles synthesized by this method [9, 14]. This is owing to the fact that the precipitation pH values of $Zr(OH)_4$, $Y(OH)_3$ and $Ni(OH)_2$ are significantly different, thus led to the difficulty of the synthesis of nano-sized and homogeneous NiO-YSZ composite particles. To improve the inhomogeneity of the sediment, pH of the solution was kept at a highly basic level (above 13) by using extra NaOH solution, so that the number density of nuclei increased and the difference of precipitation rate among the hydroxides was smaller [14]. Unfortunately, highly basic level was not usually achieved and the sodium contained in the resultant powders may also reduce the long-term stability of the anode [15].

Introduction of zirconium basic carbonate complex is a useful alternative for the synthesis of homogeneous NiO-YSZ composite materials. In the previous literature [16], it has been demonstrated that the anionic zirconium carbonate complex was formed in various carbonate or hydrogen carbonate solutions such as NH_4HCO_3 under weakly basic conditions and it reacted with the cationic surfactant to obtain the sediment of corresponding salts. However, these anionic carbonate precursors have not yet been applied for the synthesis of NiO-YSZ composite particles.

In this study, we propose a facile synthetic route to NiO-YSZ nanocomposite particles by using the reaction of anionic zirconium carbonate complex with nickel and yttrium metal cations in the organic base solution. It is expected that the three constituent elements can be homogeneously precipitated well by this method, without any inorganic impurities such as Na^+. In this chapter, the properties of synthesized nanocomposite particles were evaluated, and their formation mechanism was discussed. Then, Ni-YSZ anode was fabricated by screen-printing NiO-YSZ nanocomposite particles and its sintering. The properties of the anode made clear that our method is promising for synthesizing Ni-YSZ nanocomposite particles for better SOFC performance.

4.2 Experimental procedure

4.2.1 Synthesis and characterization of NiO/8YSZ nanocomposite particles

In this experiment, NiO and YSZ (8mol% Y_2O_3-ZrO_2) mass ratio was chosen as 0.656: 0.344, corresponding to the volume ratio of Ni: YSZ =0.5:0.5 in the final Ni/YSZ anode. Firstly, 0.015 mol of $ZrO(NO_3)_2 \cdot 2H_2O$ was dissolved in 100 ml ultrapure water (resistivity>18MΩ cm, Sartorius AG, Germany), and then it was slowly added to 0.5 M tetramethylammonium hydrogen carbonate solution (TMAC, $(CH_3)_4NHCO_3$) upon vigorous stirring to prepare a clear solution A (Note: it is expected the solution has zirconium basic carbonate complex). The concentration of zirconium in the solution A was about 0.06M. Secondly, the $Ni(NO_3)_2 \cdot 6H_2O$ and $Y(NO_3)_3 \cdot 6H_2O$ were dissolved in 83 ml of ultrapure water under stirring, and they were added dropwise into the solution A. Then, the precipitates were immediately formed. During the precipitation, another organic base, tetramethylammonium hydroxide (TMAH, $(CH_3)_4NOH$) was added simultaneously to keep the solution pH 7.7. The mixture was kept stirring well for 30 min. The precipitates were filtered and washed by ultrapure water three times and then washed by ethanol once. They were dried in an oven at 80℃for 24 h. The dried precipitates were pulverized by alumina mortar and pestle, and then calcined at

400~1000℃ for 2h using a ramp speed of 5℃/min. The schematic flow diagram of synthesizing NiO/YSZ composite particles was shown in Fig. 4.1. NiO content of as-prepared NiO-YSZ composite powders was measured by the quantitative analysis of X-ray fluorescence instrument. Theoretical NiO content in NiO-YSZ composite particles was calculated by the reactant concentrations. The total yield of NiO-YSZ composite was determined by comparing the mass of obtained powders with the originally designed mass. For comparison, the precipitation agent system of $NH_3 \cdot H_2O$-NH_4HCO_3 was also used, and the same procedures were applied to make NiO-YSZ composite particles.

Phase identification of the prepared precursor and that of the composite particles obtained after calcinations were carried out using powder X-ray diffraction(XRD, D2 phaser, Bruker, Germany), with Cu-Kα radiation (λ= 0.1542 nm). The microstructure of the synthesized nanoparticles was examined by transmission electron microscopy (TEM; JEM-2010H, JEOL, Tokyo, Japan) and scanning electron microscopy (SEM; ERA-8800FE, Elionix, Tokyo, Japan). The specific surface area (SSA) of the NiO/YSZ composite particles was measured by the nitrogen gas adsorption based on the BET multipoint method (BET, ASAP-2010, Shimadzu, Tokyo, Japan).

To discuss the present precipitation phenomena using TMAC-TMAH system, co-precipitation experiment for only Ni and Zr were additionally conducted. Since the real amount of Y for NiO-YSZ synthesis is quite small compared to that of Ni or Zr, Y was not taken account for the experiment. The molar ratio of Ni/Zr was changed from 0 to 8.0 while the concentration of Zr was kept constant. Concentration of Ni and Zr in the supernatant after the sedimentation of precursor was measured by X-ray fluorescence instrument (EDX-800; Shimadzu, Tokyo, Japan) and it was correlated with the ratio of Ni/Zr. Thermal decomposition behavior of the precursor was examined by thermogravimetry - differential thermal analysis (TG-DTA, EXSTAR 6200, SII Nano Technology, Japan) in the temperature range 25~1000℃with heating rate of 5℃/min under air flow of 100 ml·min^{-1}. The carbonate amount contained in the as-prepared precipitates was estimated from the carbon content measured by a total organic carbon analyzer (TOC-V; Shimadzu, Japan).

4.2.2 Cell fabrication and electrochemical performance testing

An electrolyte-supported cell was employed for electrochemical performance testing. Firstly, fully dense YSZ electrolyte with the thickness of 300 μm and the diameter of 13 mm was fabricated by conventional tape casting, followed by sintering at 1350℃for 2h. Then the anode was fabricated on one side of the electrolyte by screen-printing a paste of NiO/YSZ nanocomposite particles and polyethylene glycol, followed by sintering at 1350℃ for 2h. Finally, the cathode was fabricated on another side by screen-printing the $La_{0.8}Sr_{0.2}MnO_3$-YSZ paste and subsequent sintering at 1100℃ for 2h. The processing flow chart of cell fabrication was shown in Fig. 4.2.

Three electrode-four lead configuration was used as the testing geometry. The cell was fixed between alumina tubes with a glass sealant. A Pt mesh connected with Pt wires was placed on both the anode and the cathode as a current collector. A Pt wire was attached along the circumference of the electrolyte as a reference electrode. The cell was heated up to 900℃ to soften the glass sealant for gas tightening. During this process, nitrogen was supplied to the anode, and dry air was supplied to the cathode and the reference electrode with a flow rate of 0.05 l/min. After the temperature was down to 800℃, anode gas atmosphere was altered from nitrogen to wet hydrogen containing 3vol% H_2O with the flow rate of 0.05 l/min. At this stage, NiO was reduced into Ni, forming pores in the microstructure. Polarization resistance (R_p) was measured with electrochemical impedance spectroscopy (EIS) at 700℃, 750℃ and 800℃. EIS spectra were recorded using a frequency response analyzer with a potentiostat (Parstat 2263, Princeton Applied Research, TN) in the frequency range $0.1 \sim 10^5$ Hz, under open circuit voltage (OCV) with an applied amplitude of 50 mV.

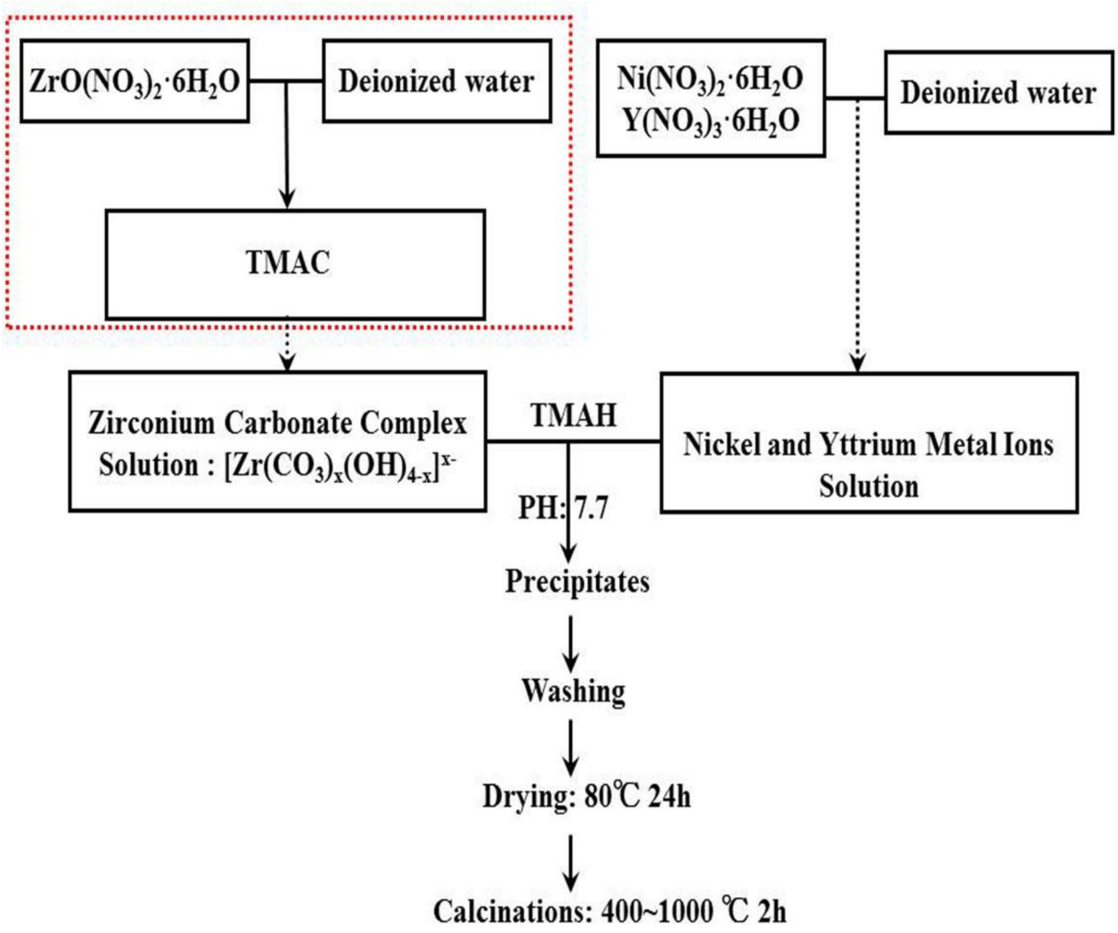

Fig. 4.1 Schematic flow diagram of synthesizing NiO/YSZ nanocomposite particles using the novel co-precipitation method.

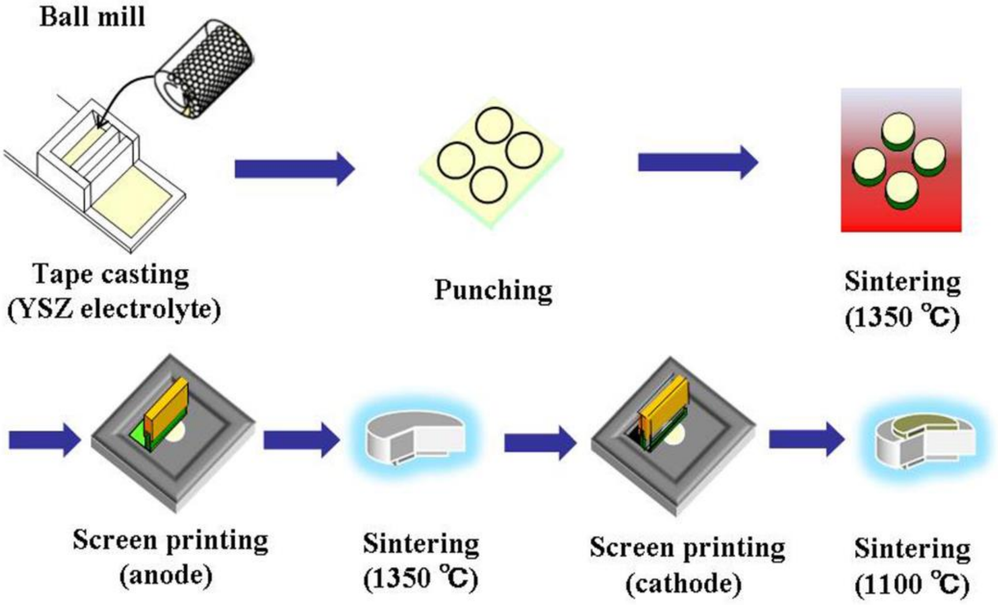

Fig. 4.2 Flow chart of the cell fabrication.

4.3 Results and discussion

4.3.1 Characterization of NiO/YSZ composite particles

Table 4.1 shows the compositions of as-prepared NiO-YSZ composite particles. When the NH_4HCO_3-$NH_3 \cdot H_2O$ system was used as co-precipitation agent at pH 7.7, the real composition of NiO in the NiO-YSZ composite powder (sample-1) was lower than the theoretical value of 65.6 mass%, and the supernatant solution showed a light blue color, indicating that a certain amount of Ni dissolved with formation of nickel-ammonia complexes [9]. On the other hand, when the TMAC-TMAH system was used, that in the sample-2 was 65.9 mass%, and the total yield of NiO-YSZ composite powder was higher than 94.0 mass%. In the TMAC-TMAH system, i.e., organic base system, Ni ions did not form any soluble complexes.

Fig. 4.3 shows the crystalline phase evolution of the sediments prepared by TMAC-TMAH system. The as-prepared precursor shows no detectable X-ray diffraction peak, indicating the amorphous nature. The weak peaks appeared after the powder was calcined at 400℃, indicating that NiO began to crystallize at this temperature. Crystalline cubic-YSZ began to appear at approximately 700℃, and the YSZ peaks continued to become more defined as the temperature increased. The average crystallite sizes for NiO and YSZ of the sample calcined at 1000℃ were calculated as 71 nm and 36 nm by Scherrer equation, respectively.

Fig. 4.4 shows SEM and TEM images of the sample prepared by TMAC-TMAH system calcined at 1000℃. The nano-sized nature of the synthesized powder was clearly observed, and it shows very narrow size distribution of NiO-YSZ particles. Specific surface area (SSA) was measured as 11.0 m^2/g for the composite particles.

Equivalent diameter of the particles was estimated using the following equation:

$$D_{BET}=6/(\rho \times S_{BET}), \tag{4.1}$$

Where D_{BET} is the BET equivalent diameter, S_{BET} is the specific surface area of the composite particles, and ρ is the theoretical density of NiO/YSZ composite. In this experiment, the mass fraction of NiO in the NiO/YSZ was 0.659, thus ρ calculated from the following equation was 6.41 g/cm^3.

$$\rho = 0.659\times \rho_{NiO} + 0.341\times \rho_{YSZ}, \tag{4.2}$$

Where ρ_{NiO} and ρ_{YSZ} are the density of NiO (6.67g/cm^3) and YSZ (5.90g/cm^3), respectively. The equivalent diameter was calculated as 85.0 nm for the composite particles. Good agreement was obtained between the BET equivalent diameter and the particle size evaluated by TEM image. It indicates that the composite particles calcined at 1000℃ are well dispersed without significant agglomerates.

To further investigate the distribution of Ni and YSZ phases in the as-synthesized composite powders, TEM-EDS element mapping was performed. From the results shown in Fig. 4.5, it is evident that NiO/YSZ composite powders exhibited a homogenous distribution of Ni, Zr, and Y phases.

Obviously, highly dispersive NiO-YSZ nanocomposite particles were successfully synthesized at a facile condition by our proposed method.

To investigate formation mechanism of the sediments, detailed co-precipitation experiments for Ni and Zr were additionally conducted. Fig. 4.6 shows the relation of Zr and Ni concentration in the supernatant as a function of Ni/Zr molar ratio. Clearly, as the concentration of Ni increased, the concentration of Zr gradually decreased and reached the minimum value at the Ni/Zr molar ratio equal to about 4.0, and then the concentration of Ni rapidly increased in the supernatant. It suggests that the Zr basic carbonate complexes were almost consumed via co-precipitation reaction with Ni ions at the Ni/Zr molar ratio ≧4.0.

Fig. 4.7 shows TG-DTG curves of the as-prepared precipitates obtained at the Ni/Zr molar ratio of 4.0. There were two temperature intervals where significant mass loss could be detected. The first one was around 100℃, that corresponded to the evaporation of the physically adsorbed water, and the second was the range between 250 and 450℃ which was related to the loss of chemically-bonded hydroxide water together with carbon dioxide (Identified from mass spectrometer for analysis of evolved gases: EGA-MS). The total weight loss between 100℃ and 1000℃ was about 35.3 mass%. If Zr and Ni were precipitated as hydroxides ($Zr(OH)_4$ and $Ni(OH)_2$), the weight loss would be 20.4mass%.

For further investigation, the as-prepared precipitates at the Ni/Zr=4 were also examined by total carbon analyzer, and subsequently its composition after firing was measured by XRF. The results of analysis were summarized in Table 4.2. Based on this table, stoichiometric molar ratio of the composition was calculated as Ni : Zr : CO_3^{2-}: $H_2O \approx 3.93 : 1.00 : 2.03 : 10.20$ in the precipitates, and then its chemical formula is roughly estimated as $Ni_4Zr(CO_3)_2(OH)_8(H_2O)_6$ or $Ni_4[Zr(CO_3)_2(OH)_2](OH)_6(H_2O)_6$ (Note: OH^- was derived from the valence balance). This is almost consistent with the chemical formula of $Ni(CO_3)_x(OH)_y \cdot zH_2O$ except the CO_3^{2-} was replaced by $[Zr(CO_3)_2(OH)_2]^{2-}$ [17-19].

This may be related to the fact that, in the presence of CO_3^{2-}/ HCO_3^-, the chemistry of zirconium in aqueous solution is dominated by soluble carbonate complex, e.g. $[Zr(CO_3)_x(OH)_{4-x}]^{x-}$. The number of carbonate ions which can coordinate to Zr^{4+} varied from 0 to 4 and is dependent on pH values as well as on the ratio of carbonate ions per Zr^{4+} [16,20-23]. It was also stressed in references [16] and [23] that these anionic zirconium carbonate complexes could be useful for the preparation of mixed oxides by interacting with cationic surfactant or metal cations to precipitate the corresponding salts. From these model experiments, it suggests that the precipitates should be obtained by the interaction of anionic zirconium carbonate complex with cationic nickel complex as we expected. Since the co-precipitation process with zirconium carbonate complex is a bit complicated. Further study should be done to elucidate the formation mechanism of the sediments including yttrium in more detail.

Table 4.1 Composition of as-prepared NiO-YSZ composite powders.

Sample	Precipitation agent	Final pH	Theoretical NiO content in NiO-YSZ (mass%)	Real NiO content in NiO-YSZ (mass%)	Total NiO-YSZ Yield (mass%)
Sample-1	NH_4HCO_3-$NH_3 \cdot H_2O$	7.7	65.6	58.1	77.8
Sample-2	TMAC-TMAH	7.7	65.6	65.9	94.2

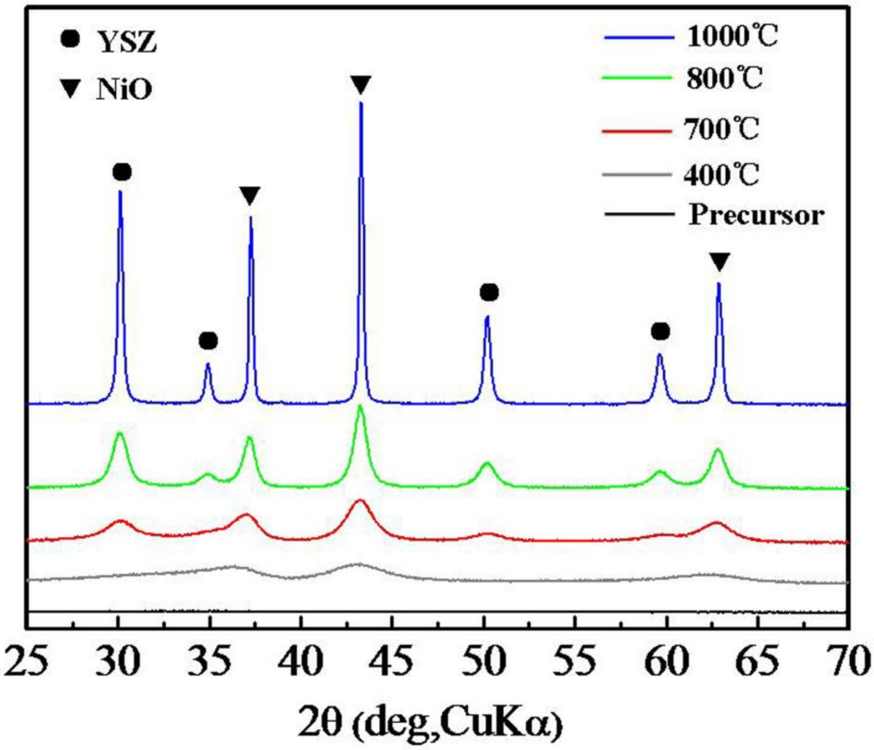

Fig. 4.3 Crystalline phase evolution of the sample-2 under different calcining temperatures.

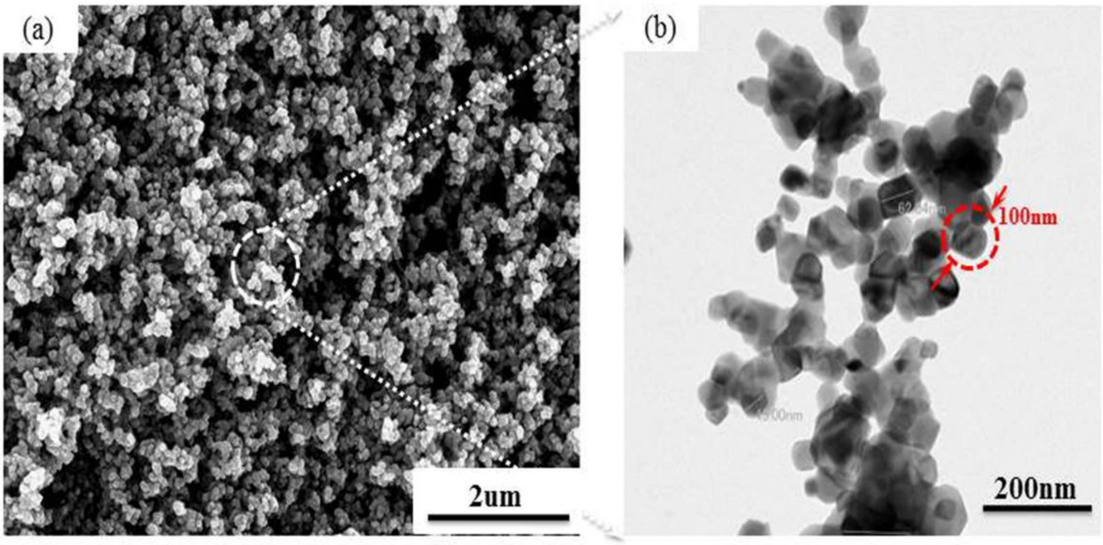

Fig. 4.4 SEM and TEM images of the synthesized NiO-YSZ composite powder (sample-2) calcined at 1000℃. (a) SEM image; (b) TEM image.

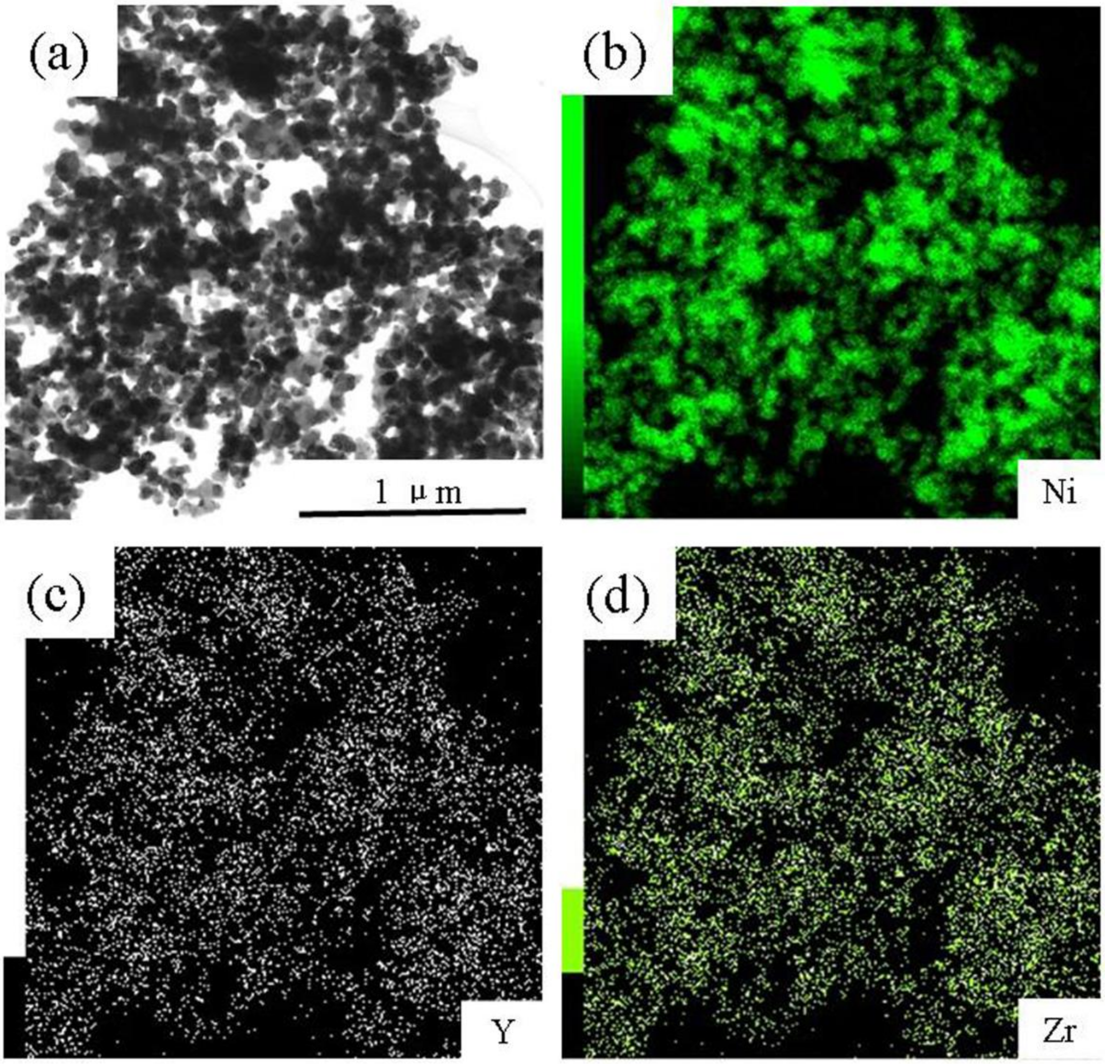

Fig. 4.5 (a) TEM image of NiO/YSZ composite powders calcined at 1000℃ and the EDS element mapping images of (b) nickel, (c) yttrium, and (d) zirconium.

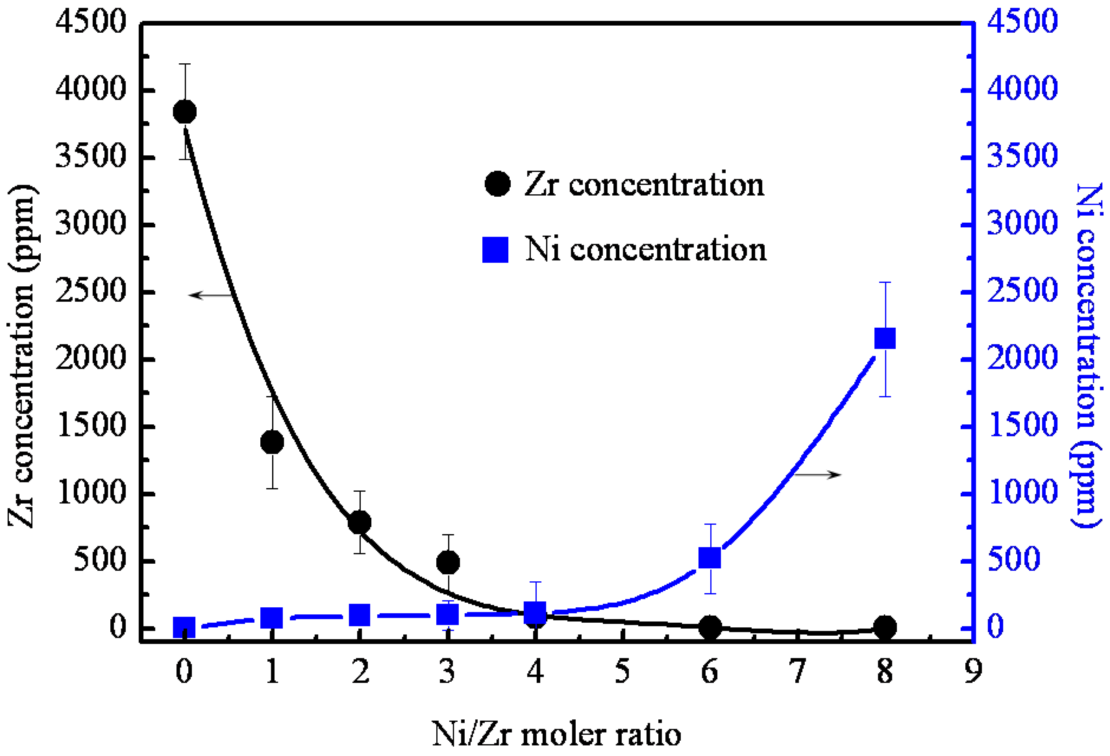

Fig. 4.6 Concentration of Ni and Zr in the supernatant as a function of Ni/Zr molar ratio of starting solution at pH 7.7.

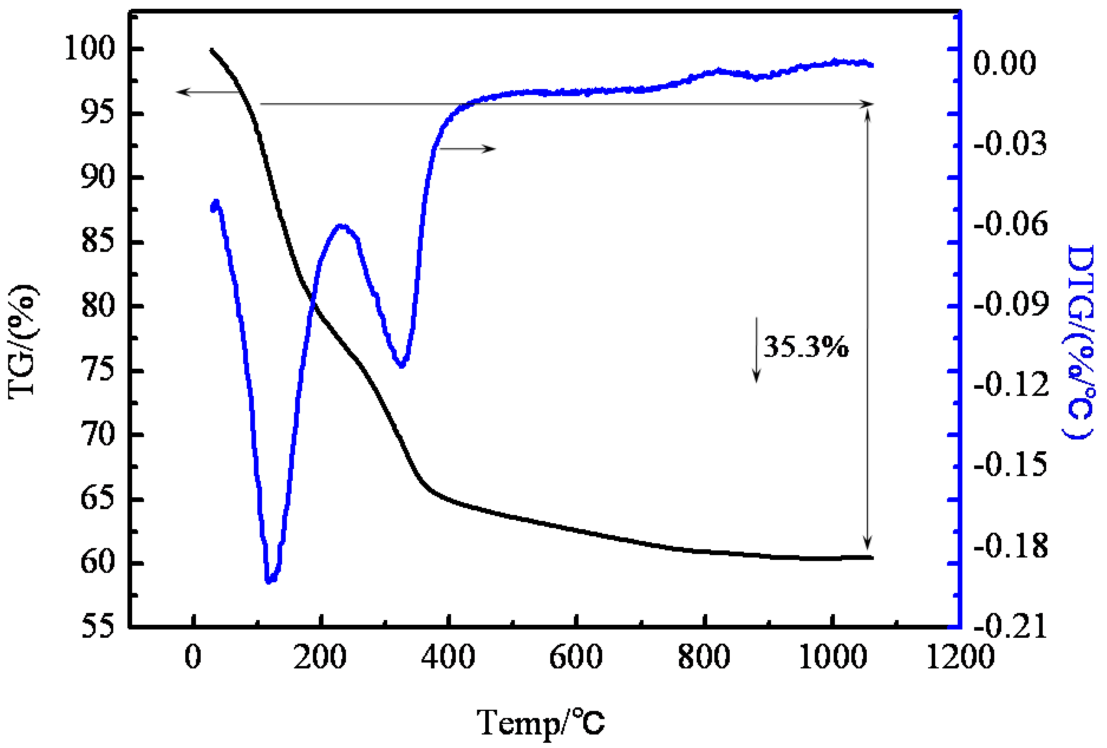

Fig. 4.7 TG-DTG curves of the as-prepared precipitate at 4.0 of Ni/Zr molar ratio.

Table 4.2 Properties of as-prepared precipitate at the Ni/Zr molar ratio of 4.0.

Name	ZrO_2	NiO	CO_2(C)*	H_2O*	Total
Composition (mass %)	17.90	42.52	12.98(3.53)	26.60	100
Composition (mass %)	5.83	22.88	11.86	59.43	100
Molar ratio (/Zr)	1.00	3.93	2.03	10.20	-

*The amount of CO_2 or CO_3^{2-} was calculated from the carbon content (3.53mass%), and the H_2O content was calculated from total weight loss and CO_2 content: H_2O=Total weight loss (H_2O+ CO_2) - CO_2.

4.3.2 Electrochemical properties and microstructure of anodes

Fig. 4.8 (a) shows SEM images of the Ni/YSZ anode after electrochemical performance testing. The low magnification image shows that the anode has good adhesion to the electrolyte as well as uniform microstructure consisting of three dimensionally connecting solid stems and pore channels. The high magnification image reveals that the anode consisted of fine grains in the range of 200~400nm as shown in Fig. 4.8 (b).

Fig. 4.9 shows EIS spectra of the Ni/YSZ anode made by NiO-YSZ nanocomposite particles shown in Fig. 4.4. As shown in Fig. 4.9, polarization resistance (R_p) of the anode was 0.62, 0.34 and 0.23 $\Omega\cdot cm^2$ at 700, 750 and 800℃, respectively. These values were comparable to those of the samples prepared from the conventional co-precipitation method at pH 13 as shown in Fig. 4.10 [14]. It shows that NiO-YSZ nanocomposite particles synthesized by the new method have high quality to be used for the anode of SOFC. The proposed method has a feature which enables us to precisely control the composition of NiO-YSZ nanocomposite particles in wide range with their nanosize, high homogeneity and high yield. It will contribute to developing higher performance of Ni-YSZ anode.

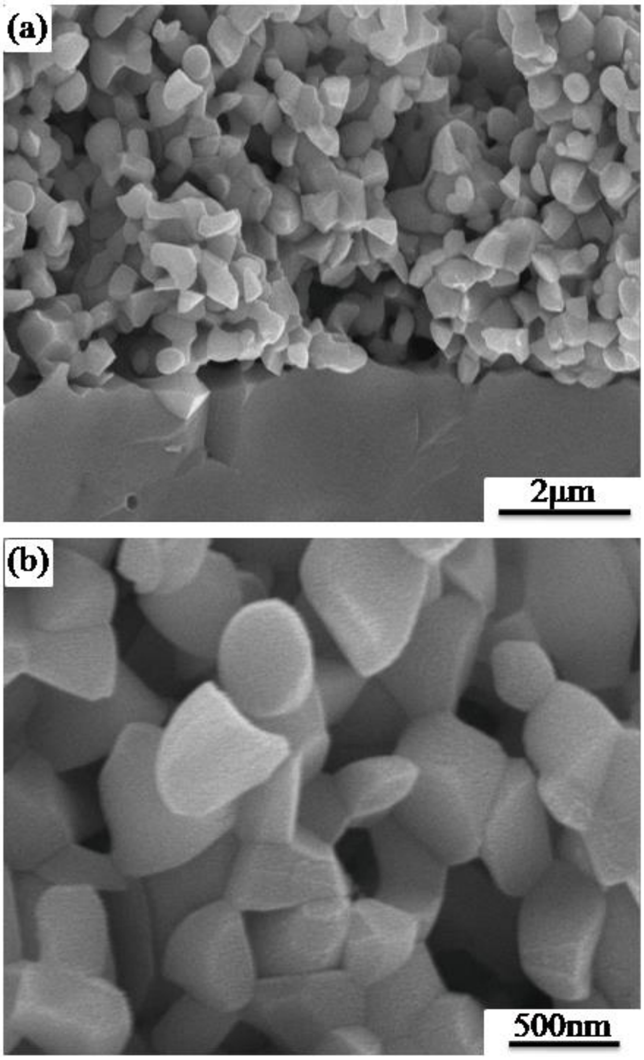

Fig. 4.8 SEM images of the Ni/YSZ anode after electrochemical performance testing (a) low magnification image, (b) high magnification image.

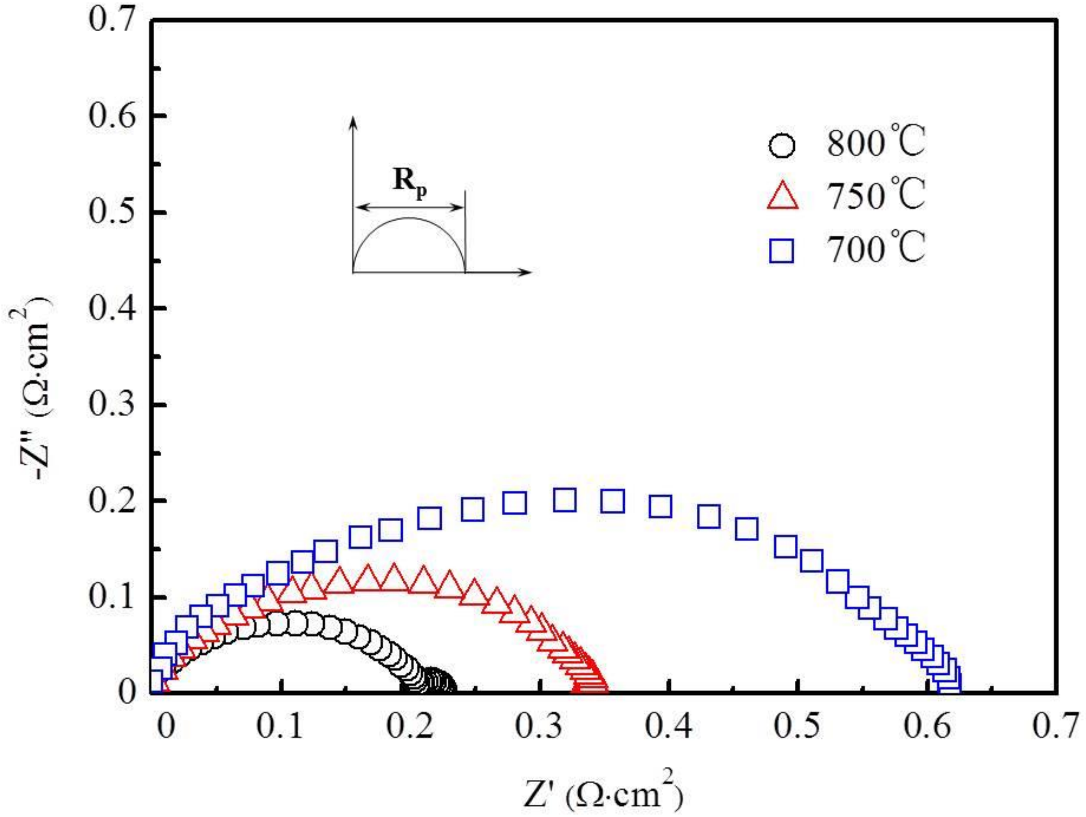

Fig. 4.9 EIS spectra of the Ni/YSZ anode measured at different temperatures.

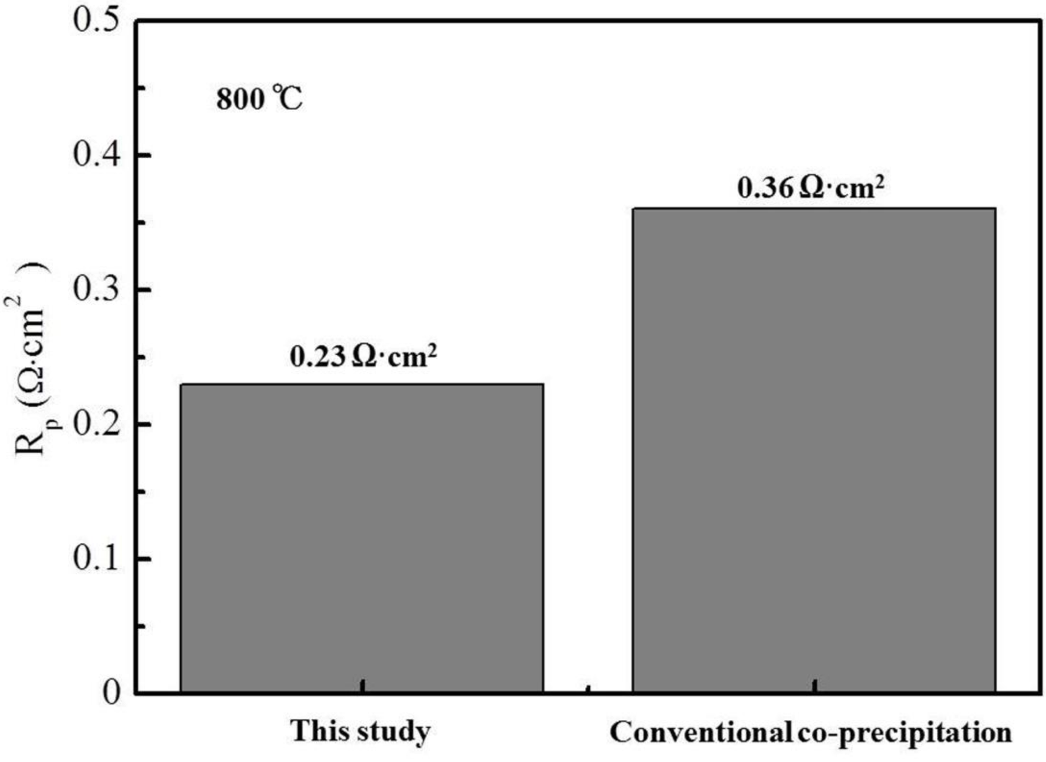

Fig. 4.10 Comparison of polarization resistance obtained by this study and the conventional co-precipitation method.

4.4 Conclusions

Highly dispersive NiO-YSZ nanocomposite particles were successfully synthesized by our proposed facile co-precipitation method. The total yield of the precipitates reached almost 100%, and the particle size of composites was around 85 nm. It was discussed that the present homogeneous precipitation was attributed to the interaction of anionic zirconium carbonate complexes with cationic nickel and yttrium ions. Grain size of the resultant Ni/YSZ anode was in the range of 200~400 nm even after being sintered at 1350℃,and the anode exhibited quite low area specific resistance due to its finer composite microstructure.

References

[1] Z. P. Shao, W. Zhou, Z. H. Zhu, Progress in Materials Science 57 (2012) 804–874.

[2] S. Primdahl, M. Mogensen, Journal of The Electrochemical Society 144 (1997) 3409–3419.

[3] M. Brown, S. Primdahl, M. Mogensen, Journal of The Electrochemical Society 147 (2000) 475–485.

[4] S. P. Jiang, Y. Y. Duan, J. G. Love, Journal of The Electrochemical Society 149 (2002) 1175–1183.

[5] S. P. Jiang, S. Zhang, Y. D. Zhen, W. Wang, Journal of the American ceramic society 88 (2005) 1779–1785.

[6] K. Sato, H. Abe, T. Misono, K. Murata, T. Fukui, M. Naito, Journal of the European Ceramic Society 29 (2009) 1119–1124.

[7] S. D. Kim, H. Moon, S. H. Hyun, J. Moon, J. Kim, H. W. Lee, Journal of Power Sources 163 (2006) 392–397.

[8] T. Fukui, S. Ohara, M. Naito, K. Nogi, Journal of Power Sources 110 (2002) 91–95.

[9] C. M. Grgicak, R. G. Green, W. F. Du, Journal of the American ceramic society 88 (2005) 308–3087.

[10] P. G. Keech, D. E. Trifan, V. I. Birss, Journal of the Electrochemical Society 152 (2005) 645–651.

[11] P. Duran, J. Tarta, F. Capel, Journal of the European Ceramic Society 23 (2003) 2125–2133.

[12] X. L. Weng, D. Brett, V. Yufit, Solid State Ionics 181 (2010) 827– 834.

[13] J. D. Lin, T. H. Hsieh, Materials Chemistry and Physics 119 (2010) 553–561.

[14] K. Sato, G. Okamoto, M. Naito, H. Abe, Journal of Power Sources 193 (2009) 185–188.

[15] Y. L. Liu, S. Primdahl, M. Mogensen, Solid State Ionics 161 (2003) 1–10.

[16] P. Afanasiev, Materials Research Bulletin 37 (2002) 1933–1940.

[17] Y. Wang, J. J. Ke, Materials Research Bulletin 31(1996) 55–61.

[18] J. M. Davidson, D. H. Glass, Industrial & Engineering Chemistry Research 46 (2007) 4772–4777.

[19] H. Henmi, M. Mori, T. Hirayama, Thermochimica Acta 104 (1986) 101–109.

[20] A. Veyland, L. Dupont, J. Rimbault, J. C. Pierrard, M. Aplincourt, Helvetica Chimica Acta 83 (2000) 414–427.

[21] A. Veyland, L. Dupont, J. C. Pierrard, J. Rimbault, M. Aplincourt, L. Devoldere, Inorganic Chemistry Communications 3 (2000) 600– 607.

[22] A. Veyland, J. Rimbault, L. Dupont, J. C. Pierrard, M. Aplincourt, S. Bourg, J. M. Nuzillard, J. F. Angiboust, Helvetica Chimica Acta 82 (1999) 2003–2014.

[23] P. Afanasiev, Catalysis Communications 9 (2008) 734–739.

Chapter 5

Effect of Composition on Microstructure and Polarization Resistance of Solid Oxide Fuel Cell Anode Ni-YSZ Composites Made by Novel Co-Precipitation

Abstract

Highly dispersed composite powders of NiO and yttria-stabilized zirconia (YSZ) were synthesized through a newly developed co-precipitation method, using an organic base solution that contains an anionic zirconium carbonate complex. It was found that a wide variation in composition can be achieved in this way. Subsequent investigation of the effect of composition on the microstructure and polarization resistance of sintered Ni–YSZ anodes revealed a significant variation in microstructure and polarization resistance. A Ni content of 40% by volume produced the finest and most uniformly porous anode structure with the lowest polarization resistance of approximately 0.18 $\Omega\cdot \text{cm}^2$ at 800 °C in a 97 % H_2 + 3 % H_2O atmosphere.

5.1 Introduction

The high catalytic activity and mechanical/chemical stability of Ni–YSZ (yttria-stabilized zirconia) cermets, as well as their compatibility with most electrolytes and interconnect materials, has made them the most extensively studied anode material in the field of solid oxide fuel cells (SOFCs) [1]. In such applications, the electrochemical reaction inside the anode is considered to occur around the triple-phase boundary (TPB), which is the contacting point that is formed among the fuel gas, the Ni and YSZ phases [2]. The Ni therefore provides not only an excellent catalyst for the electrochemical oxidation of hydrogen, but also the predominant electron pathway through the anode. At the same time, the YSZ creates the necessary framework for the dispersion of Ni particles, and inhibits growth of the Ni powder during both consolidation and operation. It also offers a significant ionic contribution to the overall conductivity, thereby effectively broadening the TPB [3, 4].

Previous studies of the polarization resistance of Ni–YSZ anodes have shown a strong dependence on the length of the TPB [5]. Specifically, a longer TPB enhances the electrochemical reaction, and therefore reduces the polarization resistance of the anode [6]. Various electrode models have revealed that the TPB length is predominantly determined by microstructural characteristics such as the particle size, and the relative distribution of its individual components. A finer microstructure with uniformly distributed phases and pores in the electrode will be beneficial to maximizing the TPB length [7, 8]. At the same time, for the sufficient transport of chemical species to and from the TPB, contiguous pathways of the three phases need to be secured; the lack of any one of these pathways results in making the TPB inactive. Many recent studies have therefore focused on electrode optimization using nano-sized starting particles, and an optimizing the fabrication processes to ensure a uniform fine-grained microstructure [9, 10].

Of the various fabrication methods that have been explored, success in achieving a homogenous distribution of multi-phase composite particles has been reported with: gel combustion [11], spray pyrolysis [12], co-precipitation [13], sol-gel [14], polymeric complexing [15] and hydrothermal methods [16]. However, these build-up processes unfortunately have several inherent disadvantages associated with their production cost, complexity, and speed of operation. A promising alternative lies in the much simpler and more easily scaled-up co-precipitation method. However, the homogeneity of NiO/YSZ composites produced by this co-precipitation is quite poor unless synthesized in a highly basic solution of NaOH ($pH > 13$) [13, 17, 18]. This is attributed to the fact that the pH at which $Zr(OH)_4$, $Y(OH)_3$, and $Ni(OH)_2$ precipitate differs significantly, leading to difficulties in achieving homogeneous NiO–YSZ composite particles. Indeed, the required level of basicity is often not achieved in practice, with the residual sodium that results from this having the potential to greatly reduce the long-term anode stability [19].

The problems associated with precipitation can be largely addressed through the use of a newly developed co-precipitation route, wherein NiO–YSZ nanocomposite particles are synthesized by adding a nickel/yttrium nitrate solution to an organic base solution containing an anionic zirconium carbonate complex at a pH of ~7.7 [20]. This has been shown to improve the polarization resistance of anodes prepared with the same Ni content using traditional co-precipitation methods. However, research is still needed to fully understand the effect of composition on the microstructure and polarization resistance of Ni–YSZ anodes produced by co-precipitation.

In this chapter, the study was focused on varying the Ni content of NiO–YSZ nanocomposite particles synthesized by the newly developed co-precipitation method and they were deposited on YSZ substrates by screen printing. Additionally, the effect of Ni content of nanocomposite particles on the polarization resistance and microstructure of the resultant Ni–YSZ anodes was discussed.

5.2 Experimental procedure

5.2.1 Synthesis and characterization of NiO/YSZ nanocomposite particles

NiO–YSZ (8mol% Y_2O_3-ZrO_2) composite powders corresponding to the suitable proportion of the Ni vol.% in the Ni–YSZ anode were synthesized using a newly developed co-precipitation method. Hereafter, the Ni–YSZ anodes with specific compositions are designated as x vol.% Ni–YSZ (x=30–70), and thus, the corresponding NiO–YSZ compositions are also referred to as x vol.% NiO–YSZ (x=30–70). The procedures are shown as follows:

First, 0.015 mol of $ZrO(NO_3)_2{\cdot}2H_2O$ was dissolved in 100 ml ultrapure water (resistivity>18 MΩ cm, Sartorius AG, Germany). Then, this solution was slowly added to a 0.5 M tetramethylammonium hydrogen carbonate solution (TMAC, $(CH_3)_4NHCO_3$) while stirring vigorously to prepare the zirconium carbonate complex solution. The concentration of zirconium in the solution was about 0.06 M. Second, the corresponding amount of $Ni(NO_3)_2{\cdot}6H_2O$ and $Y(NO_3)_3{\cdot}6H_2O$ were dissolved in 83 ml of ultrapure water while stirring. This was subsequently added dropwise into the zirconium carbonate complex solution. Upon which, the precipitates were immediately formed. During the precipitation, another organic base, tetramethylammonium hydroxide

(TMAH, $(CH_3)_4NOH$) was added simultaneously to maintain the solution pH at the corresponding value (pH: 6.5–8.5). The mixture was stirred well for 30 min. The precipitates were filtered and washed with ultrapure water three times, and then washed with ethanol once. They were then dried in an oven at 80 ℃ for 24 h. The dried precipitates were pulverized using an alumina mortar and pestle, and Ni-YSZ composite powder was obtained by heating at 5 ℃/min to 1000 ℃ and holding for 2 h.

The NiO, Y_2O_3 and ZrO_2 content of the as-synthesized NiO–YSZ composite powders was measured using the quantitative X-ray fluorescence analysis (EDX-800; Shimadzu, Tokyo, Japan). The theoretical contents of NiO, Y_2O_3 and ZrO_2 in the NiO–YSZ composite particles were calculated from the reactant concentrations. The total yield of the as-synthesized NiO–YSZ composite powders was evaluated by measuring the concentration of Ni, Y and Zr in the supernatant after sedimentation. Phase identification of the as-synthesized composite powders was carried out using powder X-ray diffraction (XRD, D2 phaser, Bruker, Germany), with Cu Kα radiation (λ =0.1542 nm). Microstructure and chemistry were characterized using scanning electron microscopy (SEM) and SEM-EDX mapping (SEM; ERA-8800FE, Elionix, Tokyo, Japan). The specific surface area (SSA) of the NiO–YSZ composite particles was determined by the nitrogen gas adsorption based on the BET multipoint method (BET, ASAP-2010, Shimadzu, Tokyo, Japan). The equivalent spherical diameter of the particles was estimated using the following equation [21]:

$$D_{BET}=6/(\rho \times S_{BET}), \tag{5.1}$$

where D_{BET} is the BET equivalent diameter, S_{BET} is the specific surface area of the composite particles, and ρ is the theoretical density of NiO/YSZ composite. In this experiment, ρ was calculated from the following equation:

$$\rho = \text{NiO mass\%} \times \rho_{NiO} + \text{YSZ mass\%} \times \rho_{YSZ}, \qquad (5.2)$$

where ρ_{NiO} and ρ_{YSZ} are the density of NiO (6.67g/cm^3) and that of YSZ (5.90g/cm^3), respectively.

5.2.2 Cell fabrication and electrochemical performance testing

An electrolyte-supported cell was employed for electrochemical performance testing. First, a fully dense YSZ electrolyte about 300 μm thick and 13 mm in diameter was fabricated by conventional tape casting, followed by sintering at 1350℃ for 2 h. Then an anode was fabricated on one side of the electrolyte by screen-printing on a paste of as-synthesized NiO–YSZ composite particles and polyethylene glycol, followed by sintering at 1350℃ for 2 h. Finally, a cathode was fabricated on the other side by screen-printing on $La_{0.8}Sr_{0.2}MnO_3$–YSZ paste and subsequently sintering at 1100℃ for 2 h. The effective electrode area was 0.28 cm^2. The thickness of the cathode and anode after the sintering was approximately 20 and 15μm, respectively.

A three electrode-four lead configuration was used as the testing geometry. The cell was fixed between alumina tubes with a glass sealant. A Pt mesh connected by Pt wires was placed on both the anode and the cathode as a current collector. A Pt wire was attached along the circumference of the electrolyte as a reference electrode. Pt paste was applied to the reference electrode to improve electrical contact. The cell was heated up to 900℃ to soften the glass sealant for gas tightening. During this process, nitrogen was supplied to the anode, and dry air was supplied to the cathode and the reference electrode with a flow rate of 0.05 l/min. After the temperature was decreased to 800℃, the anode gas atmosphere was altered from nitrogen to wet hydrogen containing 3 vol% H_2O with the flow rate of 0.05 l/min. At this stage, NiO was reduced to Ni, forming pores in the microstructure. The polarization resistance (R_p) was measured with electrochemical impedance spectroscopy (EIS) at 600–800℃. EIS spectra were recorded using a frequency response analyzer with a potentiostat (Parstat 2263, Princeton Applied Research, TN) in the frequency range of 0.1–10^5 Hz, under open circuit voltage (OCV) with an applied amplitude of 50 mV.

5.3 Results and discussion

5.3.1Characterization of NiO/YSZ composite particles

Table 5.1 shows the composition of the various NiO–YSZ powders produced. It is clear that composition can be accurately controlled through the pH of the suspension. Indeed, the compositions of the individual NiO, Y_2O_3, and ZrO_2 phases are close to the theoretical values predicted from the reactant concentrations. The absence of a blue aqueous solution during precipitation was indicative of the fact that Ni ions do not form a soluble complex in the organic base system used. This allowed all of the composite powders to be synthesized under fairly benign conditions (i.e. a pH of 6.5–8.5). The total yield achieved (>93.0 mass%) is still comparable to those obtained from the previous studies using highly basic conditions (pH > 13) [13, 18].

From the XRD patterns of the as-synthesized NiO–YSZ powders as shown in Fig 5.1, we can see that cubic-YSZ and NiO phases are present in all instances, with no other phases within the detection limits of XRD. The crystallite size of the NiO and YSZ phases were determined from their respective main peaks using the well-known

Scherrer equation [22]:

$$\mathrm{A}=\frac{K\lambda}{\beta\cos\theta} \tag{5.3}$$

where K (here, K=0.89) is a shape factor, λ is the wavelength of the X-ray beam used (λ =0.1542 nm), θ is the angle between the incident beam and reflecting plane, and β is the full width at half maximum (FWHM) of the X-ray diffraction peak. As evidenced by the results presented in Table 5.2, there is clearly a slight increase in the NiO crystallite size with increasing Ni content, while the size of the YSZ is reduced slightly. Despite this, the crystallite size of both phases is still well within the nanoscale range and close to the particle size calculated from their BET specific surface area (SSA), indicating that the composite particles were all well dispersed without substantial coarsening during the calcination.

The SEM images in Fig. 5.2 show that as the Ni content of the synthesized powders is in the range of 30 to 50 vol%, a uniformly nano-sized particles is obtained. The notable exception is the powder containing 70 % Ni, which exhibits a significant degree of coarsening. These results differ from those previously obtained with conventional co-precipitation in NaOH [13, 23, 24]. The composite particles produced in those studies exhibit two distinct morphologies: small nano-particles of YSZ and larger NiO crystallites. Furthermore, the composite particles varied in size from the sub-micron to several microns.

To further investigate the distribution of Ni and YSZ phases in the as-synthesized composite powders, SEM-EDS element mapping was performed. From the results shown in Fig. 5.3, it is evident that a Ni content of between 30 and 70 vol% results in a homogenous distribution of Ni, Zr, and Y phases. There is therefore a clear advantage to using our co-precipitation method for the synthesis of NiO–YSZ composite particles.

Table 5.1 Composition of as-synthesized NiO-YSZ composite powders.

Ni (vol.%)	pH	$NiO_{(th)}$ (mass%)	$NiO_{(r)}$ (mass%)	$Y_2O_{3(th)}$ (mass%)	$Y_2O_{3(r)}$ (mass%)	$ZrO_{2(th)}$ (mass%)	$ZrO_{2(r)}$ (mass%)
30	6.5 ~ 6.7	45.1	45.5	7.8	7.6	47.1	46.9
40	7.0 ~ 7.3	56.2	57.7	6.2	6.5	37.6	35.8
50	7.5 ~ 7.7	65.6	65.9	4.9	4.8	29.5	29.2
70	8.2 ~ 8.5	81.8	82.4	2.6	2.4	15.6	15.2

※ $NiO_{(th)}$ is the theoretical content in NiO-YSZ; NiO(r) is the real content; $Y_2O_{3(th)}$ is the theoretical content; $Y_2O_{3(r)}$ is the real content; $ZrO_{2(th)}$ is the theoretical content; and $ZrO_{2(r)}$ is the real content.

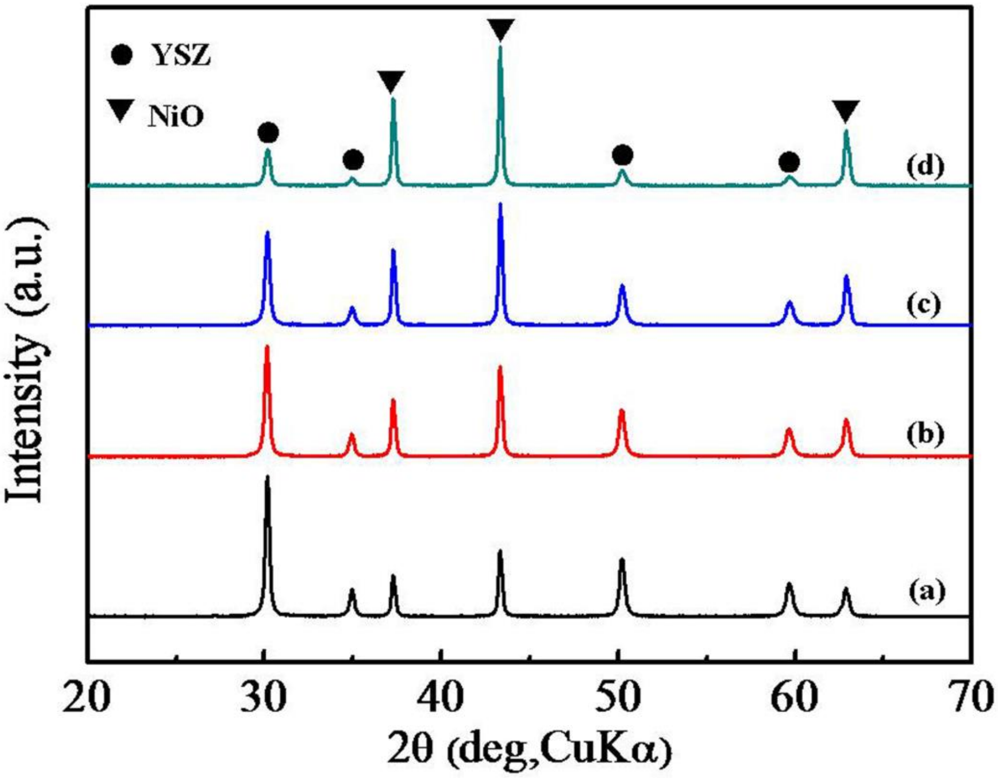

Fig. 5.1 XRD patterns of as-synthesized NiO–YSZ powders containing (a) 30, (b) 40, (c) 50, and (d) 70 vol% Ni.

Table 5.2 Crystallite size and BET SSA of as-synthesized NiO-YSZ composite powders.

Name	Crystallite size (nm)		BET SSA(m^2/g)	Calculated particle size(nm)
	NiO	YSZ		
Ni: YSZ=3:7	66.0	45.2	11.5	83.5
Ni: YSZ=4:6	62.5	40.4	12.7	74.5
Ni: YSZ=5:5	71.0	36.3	11.0	85.1
Ni: YSZ=7:3	78.6	33.8	7.8	117.8

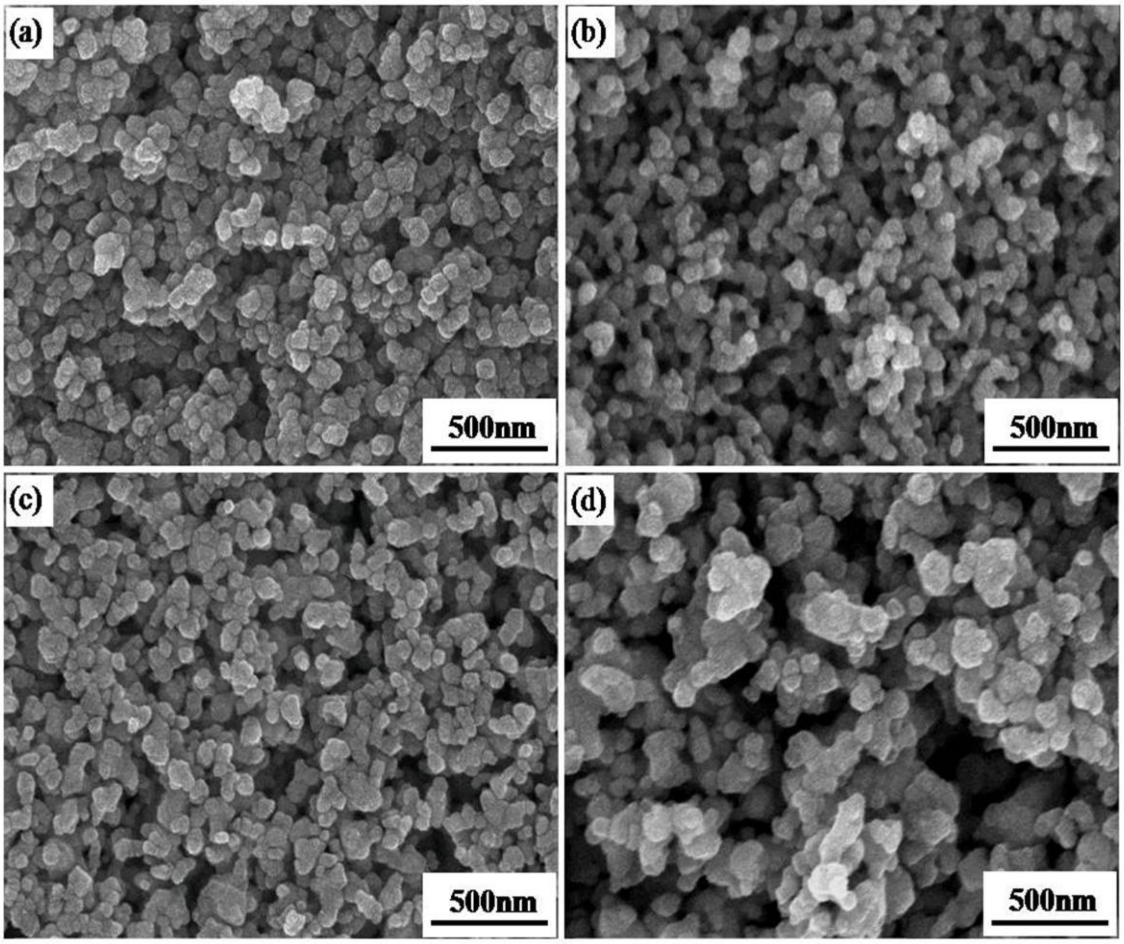

Fig. 5.2 SEM images of as-synthesized NiO–YSZ powders containing (a) 30, (b) 40, (c) 50 and (d) 70 vol% Ni.

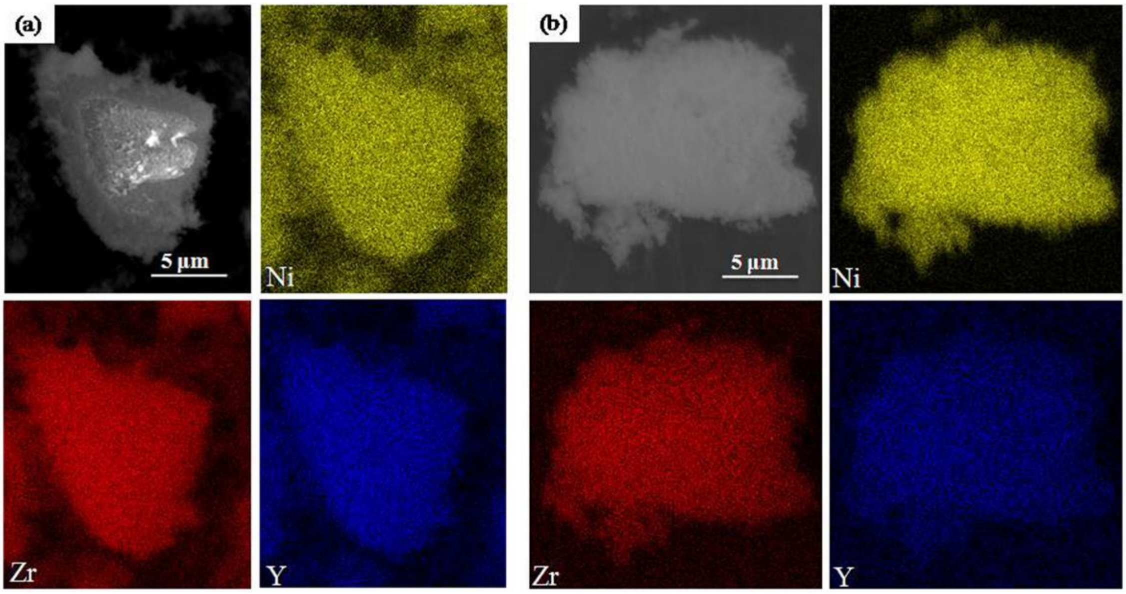

Fig. 5.3 SEM-EDS element maps of NiO–YSZ composite powders containing (a) 30, and (b) 70 vol% Ni.

5.3.2 Electrochemical properties and microstructure of anodes

Fig. 5.4 shows the EIS spectra of the Ni/YSZ anodes, as measured at 800 °C. The polarization resistance (R_p) is represented as the difference in the intercepts of the high and low frequency arcs with the real axis. To more clearly demonstrate the variation of R_p as a function of the Ni content, the ohmic resistance (R_o) was subtracted from each impedance arc. Since the total R_o includes both the R_o of the bulk electrolyte and the electrode, a slight variation in the thickness of the electrolyte is sufficient to cause a significant variation in the total R_o. Thus, it is difficult to compare the variation in R_o between anodes directly. Nevertheless, the polarization resistance of the 70 vol% Ni–YSZ anode is clearly different from the other samples, with the Ni contents of 30, 40, and 50 vol% resulting in smaller impedance arcs, and the R_p values of 0.34, 0.18, and 0.23 $\Omega\cdot$ cm^2, respectively. It is also apparent that the 40 vol% Ni–YSZ specimen exhibits the lowest R_p value at 0.18 $\Omega\cdot$ cm^2, which is comparable to reported values in the literature for high-performance Ni/YSZ anodes [17, 25].

Fig. 5.5 shows Arrhenius plots for the reciprocal of R_p within the temperature range of 600 to 800 °C. The slope of the lines plotted can be used to estimate the apparent activation energy (E_a) of H_2 oxidation. It is approximately 1.2 eV, and therefore consistent with the published values for other Ni–YSZ anodes [26, 27]. This similarity in H_2 oxidation activation energy suggests that the rate limiting step for electrochemical reaction is the same for all anodes, and thus the low polarization resistance observed in this study may be related to the formation of longer TPBs. This relationship can be expressed by [28]:

$$R_p = \frac{\beta}{\ell_{TPB}^{\alpha}} \tag{5.4}$$

where R_p is the polarization resistance, α and β are constants, and ℓ_{TPB} is the length of the TPB.

The SEM images of the Ni/YSZ cermets after electrochemical testing (Fig. 5.6) reveal that a fine, uniform and porous structure is obtained with a Ni content of between 30 and 50 vol%. This was somewhat expected from the properties of the initial powders, and may be attributed to the uniform dispersion of the NiO and YSZ phases, as the pores of the resultant Ni–YSZ anode are predominantly formed by the reduction of NiO into Ni. These microstructural characteristics contribute to maximizing the length of the Ni-YSZ-gas TPB, thereby leading to improved electrochemical performance; the poor anodic performance of the 70 vol% Ni–YSZ cermet is most likely caused by its unique structure consisting of agglomerations of weakly connected small grains.

It is generally recognized that YSZ plays an important role in suppressing the sintering of Ni during the preparation of Ni–YSZ anodes [29]. It is therefore possible that an appropriate YSZ content could cause the uniformly distributed NiO and YSZ phases to effectively suppress each other's grain growth during high temperature sintering. Following reduction of the NiO, this should result in a finer and more uniformly porous structure, and a significantly enhanced TPB length [7, 8]. An optimal composition should also be beneficial to the transport rate of each species; the vapor, electron, and ion transport rates all were approximately equal [28]. This may be the origin of the minimum polarization resistance of the 40 vol% Ni–YSZ cermet.

When the YSZ content is reduced to 30 vol% (70 vol% Ni), its function as a secondary phase is weakened to the extent that aggregated Ni grains start to form (Fig. 5.6 (d)). At the same time, the porosity of the resultant Ni–YSZ cermet is increased, as these are predominantly formed through the reduction of NiO. The end result is a reduction in the contact area of the electrode/electrolyte (Ni/YSZ) interface, which hinders charge transfer. Furthermore, the connection between YSZ grains is weakened, hindering the movement of oxygen ions through this phase and slowing the overall charge transfer process at the TPB [30]. This combination effects easily explains the significant increase in polarization resistance observed at lower YSZ contents.

On the other hand, when the YSZ content increased up to 70 % (30 vol% Ni), the value of R_p increased, as shown in Fig. 5.4. This may be because of the fact that Ni is a catalyst for the electrochemical oxidation of hydrogen, and thus reducing its content also reduces the number of available electrochemical reaction sites. This should also lead to an increase in the volume fraction of isolated Ni particles, thereby increasing the fraction of electrochemically inactive TPBs and negatively affecting the rate of electron transport and charge transfer [30]. The reduction in porosity seen with increased YSZ content in the cermet will also invariably have some effect on the gas permeation through the anode; however, the thinness of the active layer in this study (approximately 15μm) means that this should have only a marginal effect at most on the polarization resistance. It is important to note that polarization resistance also depends on the microstructure of the electrode, and thus all processing variables need to be optimized and meticulously controlled to ensure greater electrochemical performance and stability.

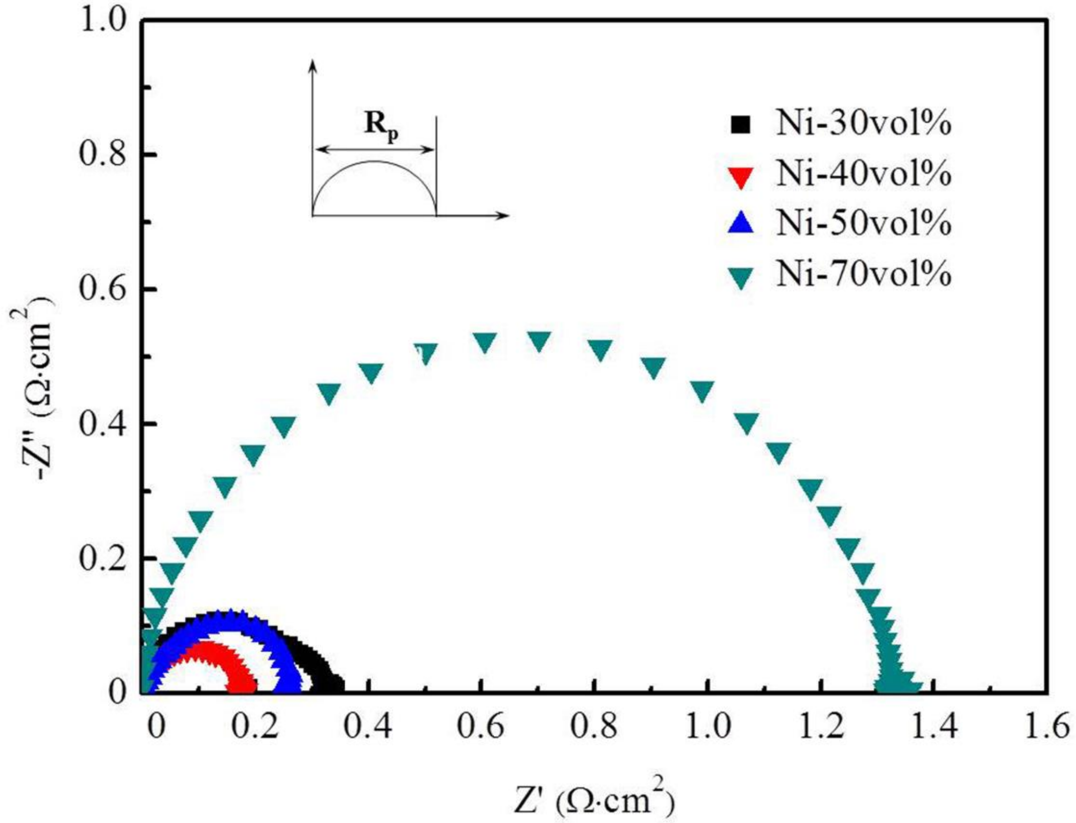

Fig. 5.4 EIS spectra of Ni/YSZ anodes with various Ni contents measured at 800 °C.

Table 5.3 Comparison of polarization resistance between this study and the previous studies.

Ref.	Operation temperature (℃)	R_p ($\Omega\cdot cm^2$)
[17]	800	0.36
[25]	800	0.15
This study	800	0.18

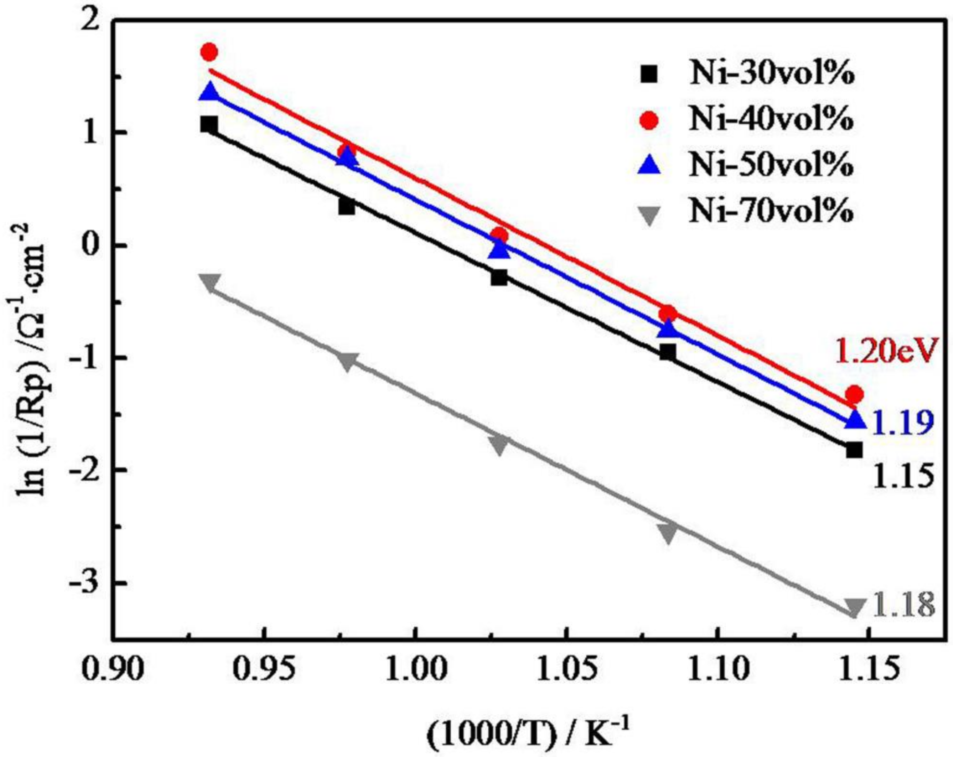

Fig. 5.5 Arrhenius plot for the reciprocal of R_p within the temperature range of 600 to 800 °C.

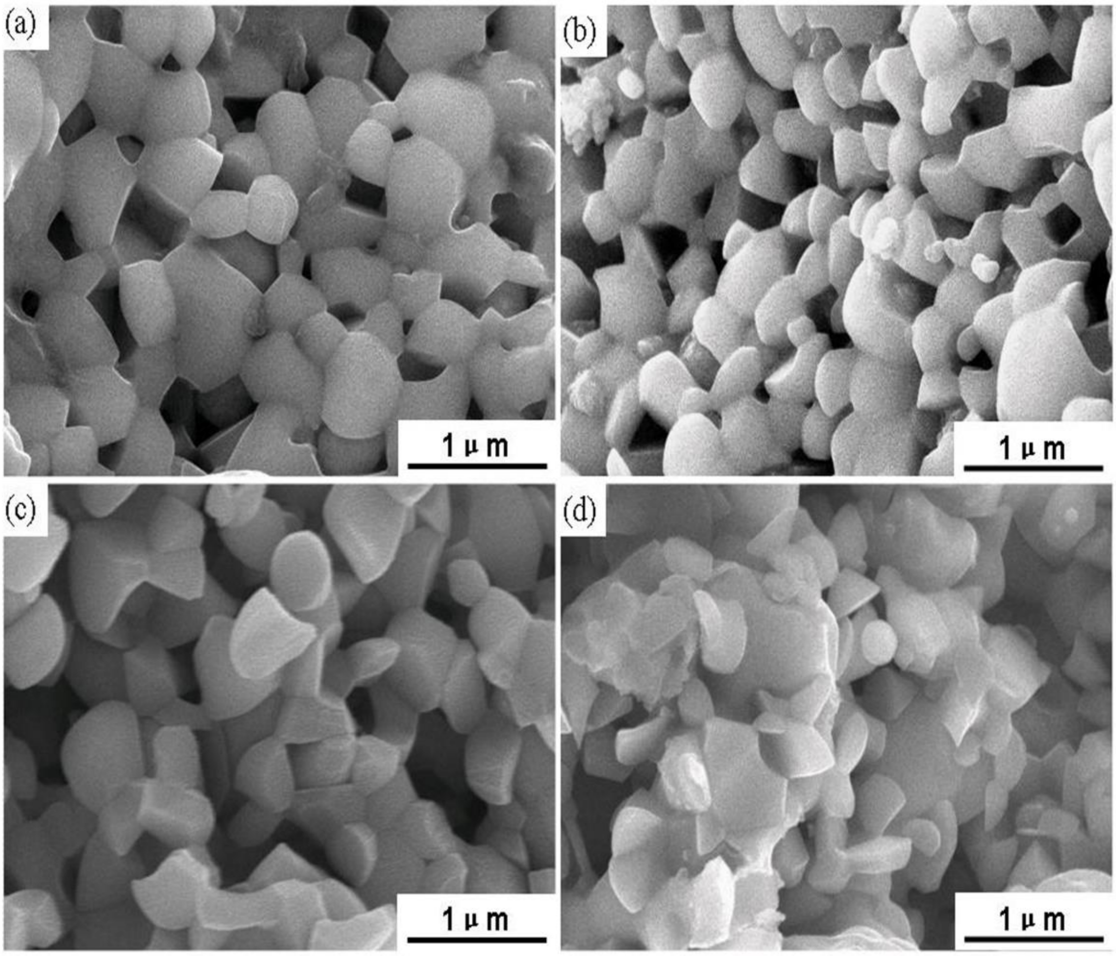

Fig. 5.6 SEM images of Ni/YSZ cermets containing (a) 30, (b) 40, (c) 50, and (d) 70 vol% Ni.

5.4 Conclusion

Homogeneous NiO-YSZ composites were successfully synthesized with a wide range of nickel contents by means of an improved co-precipitation method under facile conditions. The Ni content was found to have a significant effect on the microstructure and electrochemical performance of the resultant Ni–YSZ anodes, with a suitably controlled cermet composition producing a finer microstructure and a lower polarization resistance. A Ni content of 40% by volume produced the finest and most uniformly porous anode structure with the lowest polarization resistance of approximately 0.18 $\Omega\cdot cm^2$ at 800 ℃. This study therefore confirms the viability of using the newly developed co–precipitation of Ni–YSZ composite particles to achieve higher performance in SOFC anodes. The new approach also has great potential for application in a variety of composites for further performance enhancement of the SOFC through an economic and environmentally safe production route.

References

[1] J. Kim, K. H. Cho, I. Kagomiyac, K. Park, Ceramics International 39 (2013) 7467–7474.

[2] M. Mogensen, S. Scare, Solid State Ionics 86 (1996) 1151–I 160.

[3] Z. P. Shao, W. Zhou, Z. H. Zhu, Progress in Materials Science 57 (2012) 804–874.

[4] F. Stephen, X. Qiao, Journal of the American Ceramic Society 86 (2003) 401–406.

[5] J. S. Cronin, J. R. Wilson, S. A. Barnett, Journal of Power Sources 196 (2011) 2640–2643.

[6] M. Brown, S. Primdahl, M. Mogensen, Journal of the Electrochemical Society 147 (2000) 475–485.

[7] Y. Deseure, L. Bultel, E. Siebert, Electrochimica Acta 10 (2005) 2037–2046.

[8] S. H. Chan, Z. T. Xia, Journal of the Electrochemical Society 4 (2001) 388–394.

[9] M. Mamak, G. S. Metraux, S. Petrov, N. Coombs, G. A. Ozin, M. A. Green, Journal of the American Chemical Society 125 (2003) 5161–5175.

[10] V. Esposito, D. Z. Florio, E. N. S. Muccillo, R. Muccillo, E. Traversa, Journal of the European Ceramic Society 25 (2005) 2637–2641.

[11] S. D. Kim, H. Moon, S. H. Hyun, J. Moon, J. Kim, H. W. Lee, Journal of Power Sources 163 (2006) 392–397.

[12] T. Fukui, S. Ohara, M. Naito, K. Nogi, Journal of Power Sources 110 (2002) 91–95.

[13] C. M. Grgicak, R. G. Green, W. F. Du, Journal of the American Ceramic Society 88 (2005) 308–3087.

[14] P. G. Keech, D. E. Trifan, V. I. Birss, Journal of the Electrochemical Society 152 (2005) 645–651.

[15] P. Duran, J. Tarta, F. Capel, Journal of the European Ceramic Society 23 (2003) 2125–2133.

[16] X. L. Weng, D. Brett, V. Yufit, Solid State Ionics 181(2010) 827– 834.

[17] K. Sato, G. Okamoto, M. Naito, H. Abe, Journal of Power Sources 193 (2009) 185–188.

[18] C. M. Grgicak, R. G. Green, J. B. Giorgi, Journal of Materials Chemistry 16 (2006) 885–897.

[19] Y. L. Liu, S. Primdahl, M. Mogensen, Solid State Ionics 161 (2003) 1–10.

[20] X. Xi, H. Abe, K. Kuruma, R. Harada, A. Z. Shui, M. Naito, Advanced Powder Technology 25 (2014) 490–494.

[21] K. Sato, T. Kinoshita, H. Abe, M. Naito, Journal of the Ceramic Society of Japan 117 (2009) 1186–1190.

[22] B. D. Cullity, S. R. Stock, Elements of X-Ray Diffraction, 3rd ed., Prentice-Hall, New Jersey, 2001.

[23] S. Mosch, N. Trofimenko, M. Kusnezoff, T. Betz, M. Kellner, Solid State Ionics 179 (2008) 1606–1610.

[24] N. F. P. Ribeiro, M. M. V. M. Souza, O. R. M. Neto, S. M. R. Vasconcelos, M. Schmal, Applied Catalysis A: General 353 (2009) 305–309.

[25] K. Sato, T. Kinoshita, H. Abe, Fuel Cells 10 (2010) 320–324.

[26] K. Sato, M. Naito, H. Abe, Journal of the Ceramic Society of Japan 119 (2011) 876–883.

[27] K. Sato, T. Kinoshita, H. Abe, Fuel Cells 10 (2010) 320–324.

[28] J. R. Wilson, S. A. Barnett, Electrochemical and Solid-State Letters 11 (2008) 181–185.

[29] J. H. Lee, H. Moon, H. W. Lee, J. Kim, J. D. Kim, K. H. Yoon, Solid State Ionics 148 (2002) 15–26.

[30] M. Chen, B. H. Kim, Q. Xu, B. G. Ahn, D. P. Huang, Solid State Ionics 181 (2010) 1119–1124.

Chapter 6

Conclusions

In this study, porous ceramics for thermal insulation material and solid oxide fuel cell (SOFC) were selected, and their promising production methods were developed. Firstly, porous ceramics for building thermal insulation material was studied. In this part, a fabrication route of porous ceramics from polishing porcelain tile residue (PPR) was proposed, as this allows us much easier fabrication by foaming during firing. And the properties of such porous ceramics have confirmed that this method is promising for achieving high-quality building thermal insulation materials. Therefore, a fundamental research on the foaming mechanism of PPR and its influential factors during firing was carried out to better control the microstructure and properties of porous ceramics from PPR. In the second part of the thesis, a novel co-precipitation method to synthesize homogeneous NiO-YSZ nanocomposite particles was proposed. It is hoped to make uniformly porous structure which makes larger TPBs for high-performance IT-SOFC. Therefore, the present thesis primarily concerns the microstructure control and characterization of the porous ceramics prepared by powder processing methods. The main conclusions in this study are summarized as follows:

In chapter 1, the background of this study and its objectives were explained.

In chapter 2, effects of magnesium oxychloride cement (MOC), SiC and their mixture on the microstructure and properties of a porcelain tile matrix were quantitatively investigated in detail. It was found that a small amount of the mixture of both MOC and SiC added into the porcelain tile matrix causes the body foaming during firing more significantly, compared to the addition of either SiC or MOC. The foaming mechanism of the PPR could be explained as follow: (a) SiC acts as a foaming agent due to its oxidation reaction to CO and CO_2 gas generation at high temperature and under alkaline molten salt conditions, and (b) MOC serves as an alkaline molten salt due to its decomposition into MgO at high temperature and accelerates the SiC oxidation, resulting in a significant foaming of the porcelain green body during firing.

In chapter 3, effects of SiC particle size and CaO content on the microstructure and foaming properties of a porcelain tile matrix were investigated, with a view to further clarifying the relationship among foaming behavior, phase composition and SiC particle size during firing of a porcelain tile matrix. It was found that the size of SiC particles added to a porcelain matrix had a significant influence on the number, size, and interconnectivity of the pores formed in the resulting product, and that this effect became more pronounced as the SiC particle size was reduced. When the SiC particle size is in the range of 25–125 μm, the use of an equal mass percent of SiC has no significant influence on the bulk density, porosity and microstructure. However, using SiC particles less than 25 μm in size results in a rapidly decreasing value of bulk density, and a much higher water-absorption, owing to that the larger and more irregular pores with a higher level of interconnectivity were formed in their microstructure. On the other hand, the addition of a small amount of CaO was also shown to significantly accelerate the foaming of a porcelain green body containing SiC, but this effect was gradually inhibited by an increasing formation of anorthite.

In this part, the foaming mechanism of PPR and its influential factors during firing were preliminary clarified. It was also found that the microstructure properties of porous ceramics can be controlled by its phase composition. This work will be used to better control the microstructure properties of porous ceramics from PPR for building materials with high thermal insulation performance.

In chapter 4, a novel synthetic route to NiO-YSZ nanocomposite particles for SOFC anode was proposed. It aimed to use the interaction of anionic Zr carbonate complex with cationic Ni and Y ions in the organic base solution to achieve its uniform sedimentation. As a result, homogeneous NiO-YSZ nanocomposite particles were successfully synthesized at a facile condition, and the total yield of the precipitates reached almost 100%. Furthermore, the resultant anode had a uniform porous structure consisting of fine grains in the range of 200~400nm even after being sintered at 1350℃, and the anode exhibited quite high electrochemical performance due to its finer and uniformly porous microstructure.

Chapter 5 described the influence of composition on the microstructure and electrochemical performance of Ni–YSZ anodes produced by the novel co-precipitation method. It was found that the homogeneous NiO-YSZ composite particles were successfully synthesized with a wide range of nickel contents under relatively neutral conditions, and that the Ni content was found to have a significant effect on the microstructure and electrochemical performance of the resultant Ni–YSZ anodes. When the Ni volume content was about 40%, the anode exhibited the finest and most uniformly porous structure and higher electrochemical performance.

In this part, a novel co-precipitation method to synthesize homogeneous NiO-YSZ nanocomposite powder for SOFC anode was developed. Its electrochemical properties made clear that this method is very promising for synthesizing homogeneous NiO-YSZ composite particles for better IT-SOFC performance. The new approach also has great potential for application in a variety of other composites, e.g., NiO-ScSZ (scandia-stabilized zirconia), for further performance enhancement of the SOFC through an economic and environmentally safe production route.

Finally, the author believes that the finding and strategies obtained in this study will contribute to the progress in materials science and engineering.

Acknowledgement

This doctoral thesis has been completed under the guidance of Professor Makio Naito of Joining and Welding Research Institute (JWRI), Osaka University. I would like to express my heartiest gratitude to him for his valuable advices and discussions throughout this work.

I am grateful to Professor Toshihiro Tanaka and Professor Yasufumi Fujiwara, of Division of Materials and Manufacturing Science, Graduate School of Engineering, Osaka University for their peer reviewing of the thesis.

I would like also to thank Professor Anze Shui, of College of Materials Science and Engineering, South China University of Technology, Associate Professor Hiroya Abe, Assistant Professor Takahiro Kozawa, Dr. Akira Kondo and Mr. Kazuo Kuruma, Joining and Welding Research Institute (JWRI), Osaka University, for their valuable assistance.

I wish to express my appreciation to Oversea Study Program of Guangzhou Elite Project for funding and providing the opportunity to enter the doctor course of engineering, Osaka University.

I wish to express my appreciation to all the members of Professor Naito's laboratory for their excellent contributions to this work.

I am grateful to Prof. Zhiqiang Li and Dr. Lin Jiang, of Shanghai Jiao Tong University, for their remarkable scientific supports.

I would like to express a special thanks to my parents and all my family for their continuous encouragement and supports.

List of publication

[1] Anze Shui, Xiuan Xi, Yanmin Wang, Xiaosu Cheng. Effect of silicon carbide additive on microstructure and properties of porcelain ceramics, Ceramics International 37(2011) 1557–1562.

[2] Xiuan Xi, Anze Shui, Yunfeng Li, Yanmin Wang, Hiroya Abe, Makio Naito. Effects of magnesium oxychloride and silicon carbide additives on the foaming property during firing for porcelain ceramics and their microstructure, Journal of the European Ceramic Society 32(2012) 3035–3041.

[3] Xiuan Xi, Linfeng Xu, Anze Shui, Yanmin Wang, Makio Naito. Effect of silicon carbide particle size and CaO content on foaming properties during firing and microstructure of porcelain ceramics, Ceramics International 40(2014) 12931–12938.

[4] Xiuan Xi, Hiroya Abe, Kazuo Kuruma, Ryo Harada, Anze Shui, Makio Naito. Novel co-precipitation method to synthesize NiO-YSZ nanocomposite powder for solid oxide fuel cell, Advanced Powder Technology 25(2014) 490–494.

[5] Xiuan Xi, Hiroya Abe, Makio Naito. Effect of composition on microstructure and polarization resistance of solid oxide fuel cell anode Ni-YSZ composites made by co-precipitation, Ceramics International 40(2014) 16549–16555.